Western Graduate&PostdoctoralStudies

Electronic Thesis and Dissertation Repository

November 2018

Experimental Investigation of the Heat Source Orientation on the Transient Flow and Thermal Behaviour of Phase Change Material During Phase Transition

Steven Jevnikar, *The University of Western Ontario*

© Steven Jevnikar 2018

Follow this and additional works at: https://ir.lib.uwo.ca/etd

Part of the Energy Systems Commons, and the Heat Transfer, Combustion Commons

Abstract

The present study reports the characterization of transient flow and transient thermal behavior of phase change material (PCM) during solid-liquid phase change (melting) through experimental investigation. Two specific aspects of the current work, both important in the field of latent heat thermal energy storage, are to investigate the influence of the flow behavior within liquid PCM on the melting and heat transfer processes, and the impact of heat source orientation on the underlying melting and heat transfer processes. A relationship between heat source orientation and the Nusselt number was discussed. The results show that the fluid velocity is critical for both the heat transport within the liquid domain and the overall melting pattern and rate. These results further extend the understanding of phase change and the associated heat transfer processes in the PCM and provide comprehensive benchmark data for the improvement of numerical models simulating the solid-liquid phase change process.

Keywords

Acknowledgments

I would first like to express my thanks and gratitude to my supervisor Dr. Kamran Siddiqui, for his above and beyond support throughout both my undergraduate and graduate degrees. He was a major reason why I decided to further my education into the Graduate program and I am thankful for the opportunities he has provided me.

I would also like to thank my colleagues and faculty members who provided me support and helped me during my study. Their assistance for all problems, big or small is sincerely appreciated.

Finally, I would like to thank my friends and family for their tireless support during my studies. Their support and encouragement throughout this time was invaluable.

Table of Contents

List of Tables

List of Figures

Nomenclature

Notation/ List of Symbols (in order of appearance)

m	Mass, [kg]
Q_s	Stored sensible thermal energy, [kJ]
c_p	Specific heat capacity, [kJ/kg K]
ΔT	Change in temperature. [K]
C_{AB}	Thermochemical component
A	Reactant A
B	Reactant B
Q_L	Stored latent thermal energy, [kJ]
h_L	Latent heat of fusion, [kJ/kg]
Q_T	Total heat storage capacity (sensible + latent), [kJ]
c_{p_s}	Specific heat capacity, solid phase, [kJ/kg K]
c_{p_l}	Specific heat capacity, liquid phase, [kJ/kg K]

T_1	Initial/final solid temperature, [K]
T_l	Melting temperature, [K]
T_2	Final/initial liquid temperature, [K]
γ_m	Melt fraction
NT_l	Number of interpolated grid coordinates above melting temperature
NT_l	Number of interpolated grid coordinates below melting temperature
N_{total}	Total number of grid points within PCM domain
$T_{l_{mean}}$	mean temperature of the liquid PCM, [°C]
$Q_{sensible}$	Instantaneous sensible heat transfer, [kJ]
t	Time, [sec]
ρ_s	Solid density, [kg/m^3]
ρ_l	Liquid density, [kg/m^3]
T_{m-liq}	Mean liquid temperature, [K]
T_{m-s}	Mean solid temperature, [K]
T_i	Initial PCM temperature, [K]
V_l	Volume of liquid fraction, [m^3]
V_s	Volume of liquid fraction, [m^3]
Q_{latent}	Instantaneous latent heat transfer, [kJ]
Q_{total}	Instantaneous sensible and latent heat transfer, [kJ]

$\overline{Nu}(t)$	Instantaneous surface-averaged Nusselt number
L	Characteristic length, [m]
k_l	Liquid PCM thermal conductivity, [W·m^{-1}·K^{-1}]
$\overline{h}(t)$	Surface-average heat transfer coefficient, [W·m^{-2}·K^{-1}]
T_s	Average hot wall surface temperature, [K]
T_{int}	Average temperature of solid-liquid interface, [K]
Ra	Rayleigh number
g	Gravitational acceleration, [m·s^{-2}]
β	Coefficient of thermal expansion of the fluid, [K^{-1}]
T_b	Bulk temperature of the fluid, [K]
ν	Kinematic viscosity, [m^2·s^{-1}]
α	Thermal diffusivity, [m^2·s^{-1}]
L_{int}	Horizontal distance: hot wall to mid-point of the solid/liquid interface, [m]
L_{wall}	Characteristic length, horizontal width of enclosure, [m]

Abbreviations

GHG	Greenhouse Gases
CAES	Compressed air energy storage
TES	Thermal energy storage
PCM	Phase change material

LHTES   Latent heat thermal energy storage

PIV   Particle image velocimetry

CCD   Charge-coupled device

PID   Proportional–integral–derivative

TC   Thermocouple

Chapter 1

1   Introduction

Energy is an indispensable part of everyday human life. Powering appliances in homes and offices, heating and cooling living spaces, traveling to and from work, and manufacturing goods all require some form of energy. By now, for most, it is expected that this energy supply will be reliable and available on demand. However, with growing concerns surrounding the scarcity of conventional energy resources and the environmental impact from the utilization of these fossil-based energy resources, there is a desperate and urgent need to explore alternative options to fulfill energy demand while mitigating the environmental damage. Furthermore, careful planning and consideration is also necessary to ensure a reliable supply of energy and livable environment for future generations [1].

Global demand for energy consumption continues to rise. Over the past two decades, from 1984 to 2004, primary energy consumption has grown by 49% [2]. This growth is forecasted to continue, with estimates predicting that by 2040, there will be a further increase of 28% in the global energy use [3]. The ongoing rise of global energy consumption can be attributed to, in part, a combination of increased growth in residential, commercial and transportation sectors partly due to increasing global population [4] and a growing middle class with a desire for an improved lifestyle [5]. This expanding middle class is most prevalent in emerging economies, where it is predicted that by 2020, the energy demand will exceed that of developed countries [2].

A significant consequence of this increased energy consumption (primarily from fossil fuels) is the rise in global greenhouse gases (GHG), where over half of the current emissions (in 2017) can be attributed to energy use (see Figure 1) [6]. There is a growing concern over these rising GHG and their negative impacts on the planet. These emissions are primarily in the form of CO_2 which has steadily increased, doubling in the past 40 years (see Figure 2) [6].
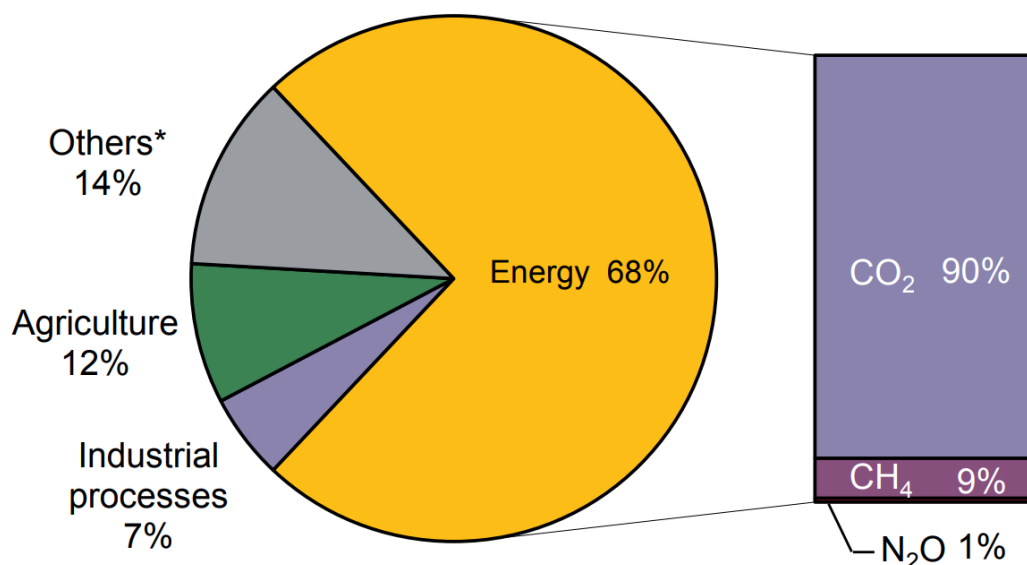
Figure 1: Estimated shares of global anthropogenic GHG, 2014 [6]

Rising GHG, including CO_2 emissions have a determinantal impact on the environment, trapping heat and raising global surface temperatures. Desertification, sea level rise, ocean acidification, decreased production of plant nutrition, and rising pollution levels are only a few of the many, well documented consequences of the rising GHG [7], [8]. Hence, with the overwhelming evidence that humans have contributed to the acceleration of global warming through energy consumption from conventional resources, there is an increasing pressure to rethink current practices. Many of the conventional energy sources such as natural gas and coal produce high levels of pollution. As well, due to their unrenewable nature and finite availability, their ongoing use is unsustainable [9]. Hence, there is an urgency to explore clean, renewable energy resources, i.e. ones that do not contribute to GHG.
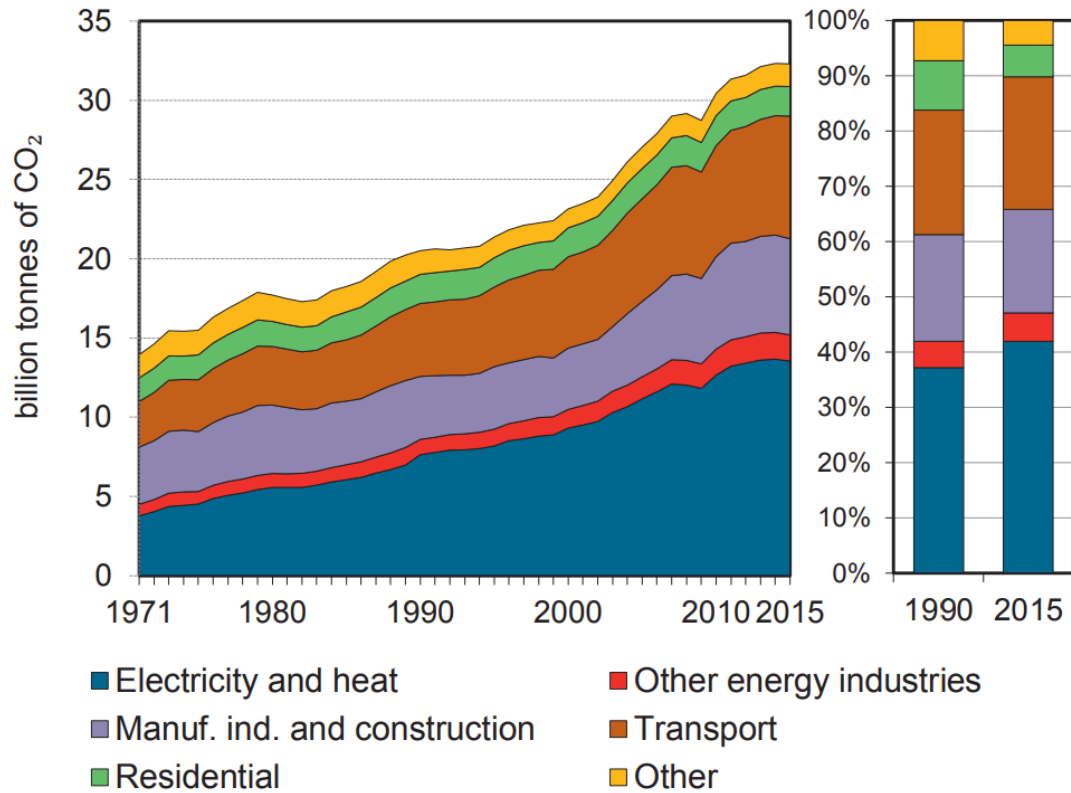
Figure 2: World CO2 emissions by sector [6]

With the transition of energy generation towards more renewable sources, such as wind and solar, a significant restructuring of power generation, consumption, and use will be necessary. While the potential for clean energy is great, many renewable energy sources still suffer from new challenges not necessarily considered before. These include mismatch between supply and demand, fluctuation of the energy intensity with seasonal variation, dependency on current weather conditions and unpredictable availability of energy sources [10]. Ultimately, due to the intermittency of their supply (i.e. lack of wind, sun, etc.), renewable energy sources in their current form are not considered as reliable resources to provide consistent energy supply.

This poses a problem for many of the current energy grids which rely on a steady energy source. More conventional forms of energy resources, such as coal, nuclear, natural gas and hydro, all operate at predictable production levels, able to match supply and demand. However, when the energy source is inconsistent and unpredictable, as it is with many

renewable energy sources, growing pressure is placed on developing methods to increase consistency. One such method to improve the consistency of energy supply from renewable resources is through energy storage [11]. Furthermore, with fossil fuels remaining a dominant energy source to meet rising energy demand, increasing pressure is placed on energy conservation as fossil fuel resources are finite. Energy storage is again a potential solution to conserve energy.

1.1   Energy Storage

Energy storage is an important component in both the conservation and utilization of generated energy. Through the storage of energy during off-peak times, or storage of excess and waste energy, the reliance on conventional energy resources can be reduced.

Within Canada, solar and wind energy are two of the fastest growing sources of electricity production [12]. Unlike conventional sources, such as fossil fuel or hydro, these types of sources are highly dependent on uncontrollable factors such as the availability of sunlight or wind. However, by utilizing stored energy, acquired during times when excess energy is available, supply can be provided at all times, even when the current generation sources may be reduced. This combination of generation and storage can mimic a more traditional type of energy production system [11].

Energy storage could also be utilized to improve the overall efficiency through the recapture of waste heat. In industrial processes involving metallurgy or chemical reactions, as well as mechanical-based thermodynamic systems, over 50% of the total input energy is discarded as waste heat [13]. In the U.S manufacturing sector, approximately one-third of the total energy is rejected as waste heat. Specifically, most of this wasted heat is considered low-grade energy, often discharged into the atmosphere through exhaust gasses [14]. This low-grade thermal energy is difficult to reuse and is often wasted. However, by developing a process through energy storage to recover and reutilize even a fraction of this heat, the percentage of wasted thermal energy could be drastically reduced, providing positive economic benefits while reducing environmental impacts [1].

Energy storage can be classified and divided into three primary categories: mechanical, electrical and thermal.

1.1.1   Mechanical Energy Storage

Mechanical energy storage is the most common large-scale type of storage. Mechanical storage is primarily in the form of pumped hydropower storage, where excess energy is used to store potential energy in the form of water that is pumped to higher elevation. Another form of mechanical energy storage which works on a similar principal, is compressed air energy storage (CAES) which uses excess energy to drive compressors, storing compression energy. Both storage methods are primarily utilized for large-scale and/or long-term energy storage [15]. Flywheels, another type of mechanical storage, converts excess energy into the form of rotational (kinetic) energy. However, unlike pumped hydropower storage and CAES, they are predominantly used for intermediate energy storage [16]. All types of mechanical storage require a relatively large footprint. Hydropower storage, which accounts for 99% of the total global storage capacity [17], use expansive reservoirs which are difficult to zone, and can negatively influence the surrounding environment [15].

1.1.2   Electrochemical Energy Storage

Electrical energy storage consists primarily of rechargeable batteries. These batteries are charged through a chemical reaction, induced by applying direct electric current. When discharged, the stored chemical energy is converted back to electrical energy. Today, electrochemical energy storage can provide very energy dense storage and it has the distinct advantage of allowing direct storage of electrical energy. However, it is often very costly to provide this storage on large scales. Therefore, while advancements have been made, it is still predominantly used with end-user storage, often utilized by consumers for temporary storage in personal devices [17].

Other electrochemical energy storage may include supercapacitors. These storage devices generally have lower energy density, often around 10% of that of a comparable battery [18]. However, these supercapacitors have a high power density, allowing them to rapidly

charge and discharge. This makes them ideal for applications that often experience either a rapid surge of excess energy or are required to provide a burst of energy [15].

1.1.3   Thermal Energy Storage

Thermal energy storage (TES) is the storage or removal of internal energy in the form of heat. It can be subdivided into sensible heat, latent heat and thermochemical heat. Sensible and latent heat storage involve the transfer of thermal energy through a temperature gradient. Thus, to store either form there needs to exist a temperature difference between the transfer and storage medium. Thermochemical heat storage involves endothermic chemical reactions and are less dependent on existing temperature gradients. When choosing an appropriate storage medium, crucial criteria include high stability from thermal cycling and resistance to long term degradation of thermal properties [16].

1.1.3.1   Sensible Heat Storage

The most common form of thermal energy storage is sensible heat storage. Sensible heat storage involves increasing or decreasing the temperature, and therefore internal energy, of the storage medium. This storage medium could either be in a fluid state (liquid or gaseous) or a solid state. However, due to lower specific heat and pressurization problems, gaseous phases are not a feasible nor practical option for the thermal energy storage. Thus, a sensible heat storage medium is either in the liquid phase (e.g. oil, water, molten salts) or the solid phase (e.g. stone, concrete, metal). Since sensible heat storage only involves temperature change in a single phase, a high specific heat capacity is desirable [19].

Water is the most common and economical type of sensible storage medium because it is readily available, has high specific heat and low cost. It is typically used in residential applications where the amount of stored thermal energy required is minimal. Water heaters and space heating are two common applications. For applications requiring high thermal energy storage, inorganic salts or metals are generally used. While water thermal storage is used in applications between 0-100 Celsius, salts and metals can be used in the range of 120-1400 Celsius [19].

The amount of thermal energy stored in a medium is dependent on the mass and temperature change. It can be expressed as a function of the mass, m [kg], the specific heat capacity, c_p [kJ/kg K] and the change in temperature, ΔT [K]:

$$Q_s = mc_p\Delta T \qquad (1.1)$$

1.1.3.2   Thermochemical Storage

In thermochemical energy storage, reversible chemical reactions are used to charge and discharge the thermal storage. Primarily, these reactions occur in either the solid or liquid state. Furthermore, this type of storage often uses a mixture of both sensible and/or latent heat storage in combination with the chemical reactions. The primary advantage of this type of storage is the ability to store thermal energy over long periods of time. While sensible and latent heat storage are often used for relatively short-term storage, thermochemical energy storage can be used for long term applications, such as seasonal storage. This is because, due to the chemical reactions in this type of storage, little energy is lost over time and the storage medium can be left at ambient temperatures [20]. Thermochemical TES involves an endothermic reversible reaction, where the thermochemical component C_{AB}, with the addition of heat, is separated into reactants, A and B, which can then be independently stored. When combining the reactants, heat is released.

$$C_{AB} + \text{heat} \rightleftarrows A + B \qquad (1.2)$$

Thermochemical storage is still in its infancy of development, with minimal commercial presence. Currently, high costs and degradation of chemical reactants during thermal cycling are primary barriers preventing this type of storage from commercial use. Additionally, these types of endothermic reactions occur above 0 Celsius, limiting their use in cold temperature and cooling applications [21].

1.1.3.3   Latent Heat Storage

Latent heat storage utilizes the enthalpy of phase change of a material to store energy. This involves the energy that is stored or released during the phase change of a material,

primarily between solid and liquid states due to practical reasons. Since heat is transferred during phase transition, unlike sensible thermal energy storage, this type of storage is theoretically near isothermal. This is beneficial for applications which require a constant temperature or when the charging and discharging of heat is within a narrow temperature band. Furthermore, the latent heat storage is attractive due to the high energy storage density, gained from the exploitation of the enthalpy of phase change. Using equal masses of water as an example, to match the total latent heat energy released during ice freezing, it would require sensibly cooling liquid by 80 Celsius [19]. The differences between sensible and latent heat storage is shown in Figure 3. Latent heat can store thermal energy at a nearly constant temperature, whereas sensible heat storage requires a large temperature difference, i.e. the greater the temperature of the medium, the more heat stored.
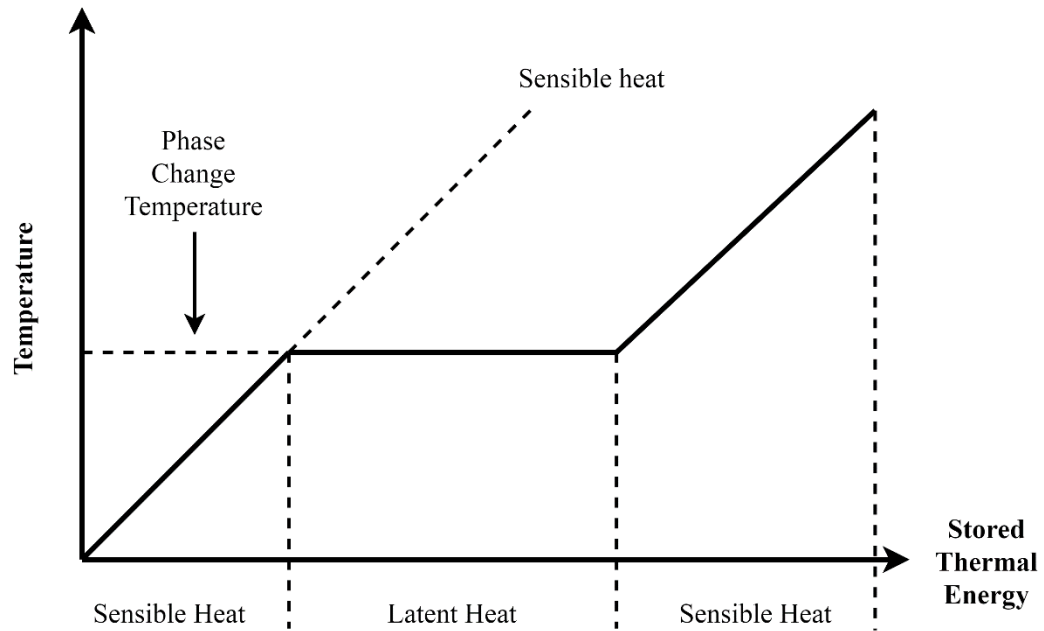
Figure 3: Sensible and latent heat storage principles

The total energy stored in latent heat storage can be expressed as a function of the materials mass, m [kg], and latent heat of the phase change of the material, h_L [kJ/kg].

$$Q_L = m \cdot h_L \tag{1.3}$$

Materials used in latent heat storage are referred to as phase change materials (PCMs). Water is one of the most common type of PCM, however, it is primarily limited for cooling applications. By using PCMs with different melting temperatures, latent heat storage can be implemented over a wide temperature range. Currently, there are commercially available PCMs with melting temperature ranging from below -33 Celsius, to above 850 Celsius [22].

Often latent heat storage systems use a combination of both sensible and latent heat storage. That is, as the storage medium is warmed or cooled in a single phase, sensible heat storage occurs, while the latent heat storage occurs during phase transition. Therefore, for a system utilizing solid-liquid phase transition, the total heat storage capacity is often expressed as [23]:

$$Q_T = \int_{T_1}^{T_l} mc_{p_s} dT + mh_L + \int_{Tl}^{T_2} mc_{p_l} dT \tag{1.4}$$

Where m [kg] is the total mass of heat storage medium, c_{p_s} and c_{p_l} [kJ/kg.K] are the specific heat capacities for the solid and liquid phases, respectively, and h_L [kJ/kg] is the latent heat of fusion. The variables, T_1, T_l and T_2 [K] refer to the initial/final (depending on melting/freezing) solid temperature, the melting temperature and the final/initial (depending on melting/freezing) liquid temperature, respectively. The first term corresponds to the sensible energy of the solid PCM, the second term is the absorbed/released latent energy and the third term is the sensible energy of the liquid PCM [23].

1.2   Comparison Between Types of Energy Storage

Each energy storage system offers distinct advantages and disadvantages, and the dominance of one type over another is highly dependent on the potential application of the storage. Thus, determining the superiority of one type of energy storage over another is a trivial process. It is likely that with the increase in renewable energy sources, and with energy efficiency becoming a crucial criterion, a combination of several types of energy storage systems will become necessary, as it is disadvantageous to rely solely on one

technology. Previous reviews of each energy storage technology have been considered [16], [24], [25]. These reviews base their comparisons on criteria such as cost, energy density, durability, efficiency and environmental impact.

Focusing on the most impactful benefits and drawbacks, a brief comparison can be conducted. Mechanical energy storage is frequently utilized in large scale applications, allowing for direct storage of excess potential energy such as pumped hydropower. However, mechanical energy storage often requires a large footprint. This limits its application in dense urban areas where energy demand is greatest [26]. Additionally, since this storage type often requires the conversion between multiple forms of energy, namely between electrical and mechanical (kinetic/potential) energy, significant losses can occur during this conversion. Electrochemical energy storage has a high energy storage density and allows for direct electrical energy storage. There exists great potential for both small and large-scale applications, with the most likely scenario involving end user storage in residential applications. However, the cost, short lifespan and environmental impact from insufficient established recycling programs remain as challenging concerns which cannot be overlooked [27]. Thermal energy storage can be used in small, medium and large-scale applications. It has the advantage of allowing direct energy transfer from heat sources, such as solar energy or waste heat. Additionally, the potential exists to incorporate TES with existing systems, to improve the efficiency of energy consumption. Latent heat thermal energy storage (LHTES) is attractive because it [16], [24]:

- Provides high energy storage density
- Is available over an extensive range of temperatures and,
- Provides nearly isothermal thermal energy storage; ideal for temperature sensitive applications.

LHTES does have drawbacks however, and there exists a significant research opportunity to advance the technology and improve the potential applications. Due to the complicated nature of phase change, with simultaneously varying solid and liquid fractions, the heat transfer processes are complex and transient. Further studies into the processes involved can help to reduce adherent weaknesses in PCMs.

1.3   Phase Change Materials

Phase change materials are materials with relatively high latent heat storage capacity. A wide range of PCMs have been developed with various melting and vaporization temperatures, increasing their suitability for a wide range of applications.

Depending on the type of material used for LHTES, PCMs can undergo solid-solid, solid-liquid and liquid-gas phase transitions. Solid-liquid transition is the most commonly used phase transition, because as mentioned earlier, during liquid-gas transformation, there are high volume and pressure changes creating practical problems. Similarly, there are very few PCMs exist which have suitable transition temperatures for solid-solid transformation, limiting their use [19].

PCMs can be classified into three primary groups: organic, inorganic and inorganic/organic eutectics. A breakdown of each primary and secondary classifications is shown in Figure 4 [23].
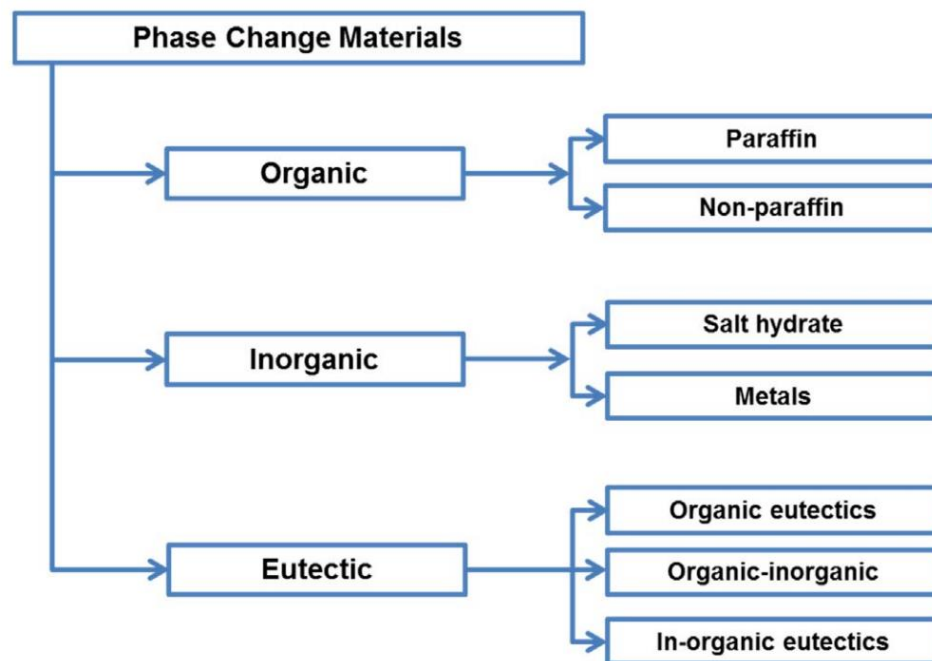
Figure 4: Breakdown of primary and secondary PCM classifications [23]

Numerous reviews have been conducted of PCM classifications, comparing properties, characteristics, and highlighting benefits/drawbacks of each group [28],[29],[30],[31],[32]. In summary, the primary focus is on desirable thermal, physical and chemical properties when selecting a suitable PCM for LHTES. The advantageous thermal properties include:

- Appropriate phase transition temperature
- High latent heat capacity
- High thermal conductivity.

Thermal conductivity is a concern for many PCMs, as most suffer from low conductivity in all phases; an undesirable trait for thermal energy storage.

Desirable physical properties of PCMs include: small volume change between phases, high density and congruent melting. In terms of chemical properties, high chemical stability with thermal cycling, low reactivity with storage enclosure, low toxicity and low flammability are all desirable traits. Additionally, PCMs that do not suffer from supercooling are advantageous.

Selection of the appropriate PCM depends on the type of application. Often, the critical selection criteria is dependent on the operating temperature range of the proposed application, and as such, the ideal PCM can be selected with a phase transition temperature in that range. The PCM selection can then be further narrowed through selection methods considering required thermal, physical and chemical properties [23].

1.4   Literature Review

Promoted by the greater usage of PCMs and LHTES, an increasing number of studies have been conducted to investigate the solid-liquid phase change through characterization of the thermal behaviors. Overwhelmingly, these studies are motivated by the rise in alternative energy sources to combat the growing concerns surrounding fossil fuel consumption and related consequences. Conducted studies include analytical, numerical and experimental work. However, often, due to the challenging nature of the two-phase investigations, numerical and experimental work are most prevalent in this field.

Some of the earliest studies on two-phase heat transfer considered only one-dimensional conduction and ignored effects of natural convection in the liquid phases. These early works, most notably by Stefan in 1891 [33] on sea ice formation, continue to impact the scientific community. Although it requires significant assumptions, the mathematical model, commonly referred to as the Stefan problem, provides a reasonable approximation of the temperature distribution within a homogeneous medium undergoing phase change [34].

Presently, it is well established that natural convection plays an important role in liquid phase during melting. Studies conducted by Sparrow et al. [35] and Bathelt *et al.* [36] are two of the earliest published studies that experimentally investigated two phase melting while considering convective heat transfer. Sparrow et al. [34] concluded through experimental work that natural convection has a dominant role in the melting of a solid, and Bathelt *et al.* [35] found that a combination of the transient melt shape (i.e. solid-liquid interface), surface temperature and heat transfer coefficients contribute to the significance of natural convection. In both studies it was concluded that natural convection should be considered in both the analysis and design of phase change systems and should not be neglected.

Recent progress varies across many different aspects in the field pertaining to heat transfer for thermal energy storage. Due to the presence of natural convective heat transfer, the geometry of the PCM container and heat source/sink orientations are important factors in the overall behavior of the heat transfer process and as such, investigations have been conducted to study the heat transfer characteristics in different enclosure geometries. Similarly, due to the low thermal conductivity of PCMs, research work has also been focused on the ways to improve heat transfer. Finally, prompted by the push towards the integration of thermal storage systems in renewable energy and sustainability applications, there are a growing number of studies pertaining to applications of PCMs and TES. As such, within this review, topics are divided into studies which primarily focus on investigating PCM phase change heat transfer characteristics, PCM based heat transfer enhancement methods and applications of PCM based TES. Comprehensive review summaries have also been reported in the literature [37], [38], [39].

1.4.1   Investigation of Heat Transfer Characteristics

Studies investigating the fundamental heat transfer characteristics present in phase change often utilize simplistic enclosure geometries. These enclosures are often either rectangular [39], [40], [41], cylindrical [42], [43], [44], [45], or spherical [46], [47]. Studies either include insulated walls, with one vertical/horizontal wall as the heat source (heated) and another as the heat sink (cooled) or only insulated walls and a single heated wall.

Commonly, it is determined that the melting process is dominated by conduction in the initial stages of heating when the heat transfer medium remains solid and after this initial stage, when melting is initiated, natural convection becomes the dominant heat transfer mode within the liquid region [48], [49], [50], [51], [52].

C.-J. Ho and R. Viskanta [53] experimentally, and numerically studied the melting of n-octadecane, isothermally heated from a vertical wall within a rectangular cavity. Comparison between experimental and mathematically predicted melt front profiles and volume fractions were conducted, finding increasing discrepancy between the two. This error was attributed to the neglection of volumetric expansion in the mathematical models and the coarseness of the utilized grid. It was concluded that melt rate, melt interface profiles and heat transfer are all significantly influenced by the buoyancy induced fluid motion in the liquid region.

The work by Wang *et al.* [51] looked at the melting behaviour of the PCM, polyethylene glycol 900 during constant heat flux melting in an insulated rectangular enclosure. In their model, one vertical wall was heated, and the adjacent wall was cooled through a heat exchanger. Thermocouples along the top wall, bottom wall and mid-plane were utilized to calculate convective heat transfer rates and direct visual measurements were used to continuously determine the temporal position of liquid-solid interface. Temporal Nusselt number results identified three heat transfer regimes, corresponding to conduction dominant, a combination of conduction and convection and convection dominant heat transfer. A critical Rayleigh number was determined, signifying the transition from conduction to the convection regime.

Shokouhmand and Kamkari [49] investigated the heat transfer characteristics of lauric acid (an organic PCM) in an insulated vertical rectangular enclosure subjected to heating from a single vertical wall. Photographs, combined with temperature data, were used to infer flow structures and characterize the heat transfer processes. Four melt stages were observed: dominant conduction, transition, dominant strong convection and weak convection. Additionally, it was found that the intensity of the convection current decreases as the melt front moves away from the hot wall source, contributing to the reduction in the melting rate.

Kamkari *et al*. [50] further expanded upon their previous work [49], by investigating the effect of inclination angle on the heat transfer characteristics of lauric acid in a rectangular enclosure. Experiments were conducted with a heat source at 0 degrees (vertical), 45 degrees and 90 degrees (horizontal). It was found that the inclination angle of the heat source had a significant effect on both the heat transfer rate and the melting time of the PCM. It was suggested that these heat transfer enhancements were due to an increase in the natural convection currents present in the liquid PCM.

Benard *et al.* [54] also studied, both numerically and experimentally, the melting process in a rectangular enclosure with one vertically heated wall using pure n-octadecane as the PCM. All other walls were insulated and the wall adjacent to the hot wall was cooled and held at a constant temperature, 0.4 Celsius below the melting temperature. The solid-liquid interface, observed through imaging, combined with thermocouple temperature measurements were used to study the melting process. It was concluded that the behaviour of melting could be approximated as a two-stage process, before and after the melt front contacted the cold wall.

Bashar and Siddiqui [55] investigated the melting behavior of a PCM and the associated heat transfer, induced by a U-shaped heat source in a rectangular enclosure. Paraffin wax was used as the PCM and the experiments were conducted at four input heat flux conditions. They measured the transient local heat transfer coefficient and found that the heat transfer coefficient of the PCM in the inner region, enclosed by the U-tube, was 35%

higher than that in the outer region. They also proposed a new Nusselt-Rayleigh numbers correlation to characterize the heat transfer during melting by a U-shaped heat source.

1.4.2   Heat Transfer Enhancement

As previously mentioned, a major drawback of many potential PCMs is the low thermal conductivity. This is especially the issue in organic PCMs which often have a liquid thermal conductivity of approximately 0.15 to 1 $W \cdot m^{-1} \cdot K^{-1}$ [56]. The poor thermal conductivity limits the ability to rapidly transfer heat in and out of the thermal storage. As such, a significant number of studies have been conducted to improve heat transfer in PCM based thermal energy storage. A detailed review of experimental and computational studies pertaining to the thermal conductivity enhancement of PCM was conducted by Fan and Khodadadi [57].

A common technique to enhance heat transfer is by using fins. Several studies have been conducted to introduce fins into the PCM medium [58], [59], [60], [61].

Bugaje [62] looked to overcome the slow thermal response of organic PCMs contained within plastic enclosures. Within a vertical glass column, paraffin wax with embedded aluminum fins was studied during heating and cooling. The fins were utilized to increase the overall heat transfer to/from the PCM. Overall melting and solidification times were recorded, and it was found that the phase transition time could be reduced by over two times during heating, and four times during cooling.

Choi and Kim [63] also investigated heat transfer enhancement with the addition of horizontal stainless-steel fins, attached to the outer surface of a vertical heat transfer tube. This tube was immersed within the high heat PCM, magnesium chloride hexahydrate. Three cases were considered with an un-finned, 5-fin-tube and 10-fin-tube. It was found that while the addition of 5-fins did increase melting by 25% when compared to the un-finned case, the addition of 10-fins had an almost negligible effect on melted volume. The heat-transfer coefficient was calculated for all cases and found to increase with increasing number of fins.

Other techniques to improve thermal conductivity involve adding highly conductive particles into the PCM medium to increase thermal conductivity. Often these particles are classified as nanoparticles which are embedded into the phase change material [64], [65].

Motahar *et al.* [66] experimentally investigated n-octadecane bounded in a rectangular enclosure heated from one vertical wall. All other walls were insulated. Nanoparticles were added to enhance the effective thermal conductivity of PCM. They observed a reduction in the melting rate as time progressed due to the reduction in the natural convection current, which was attributed to the increase in viscosity due to the nanoparticles addition.

Bashar and Siddiqui [67] investigated the transient melting and heat transfer characteristics of a nanoparticle-PCM mixture. Four different types of nanoparticles were tested: silver, copper oxide, aluminum and multi-walled carbon nanotubes and were added to the PCM, paraffin wax. A surfactant was added to the PCM to improve nanoparticle dispersion. Results show improvements to thermal performance for all studies with nanoparticles. It was shown that the addition of nanoparticles increases the PCM viscosity. However, the added surfactant was found to counteract the viscosity rise from the nanoparticles, limiting any negative reduction in the natural convection. Silver and the copper oxide nanoparticles were found to be the most effective, increasing heat transfer coefficients by approximately 18% and 14%, respectively. It was concluded that nanoparticle-enriched PCM is beneficial for latent heat TES.

Other methods of heat transfer enhancement include methods such as the addition of carbon fibers [65], [68] and with technological advances, carbon nanotubes [69].

A study by Oh and Yang [70] looked at improving heat transfer in the PCM, n-octadecane, through ultrasonic vibrations. The vibrations were used to accelerate the melting process. A thermal camera coupled with particle image velocimetry was used to examine the heat transfer. They concluded that ultrasonic vibration led to an increase in upward flow, enhancing heat transfer. Analysis of particle image velocimetry data was limited to a qualitative analysis between the cases with and without ultrasonic vibration.

1.4.3   PCM-based TES Applications

There are many studies investigating practical applications of the PCM-based TES systems. Dincer and Rosen [71] provided an extensive overview of various TES systems. Other studies also provided reviews on current and potential implementations of PCM-based TES systems [22], [72], [73].

Common PCM-based TES applications include, but are not limited to: storage of solar thermal energy [74], [75], [76], [77], passive cooling in buildings [78], [79], [80], integration with electricity generation, utilizing off-peak demand TES [81], [82] [83] and cooling from engines (combustion or electric) [84], [85].

Sun *et al.* [86] developed a novel TES system to recover heat from industrial residual water (IRW), a byproduct of a production process which was used during operation to heat the production plant. However, to meet heating requirements, production was required to run at less than 100% capacity to distribute the workload and allow continuous operation 24 hours of the day. By storing excess waste heat during production, the plant could run more efficiently at full capacity, and utilize stored thermal energy during plant shutdown. A mathematical model, validated with experimental data, was generated to test the potential application and benefits of a shell and tube TES system. It was concluded that such a system could meet heating requirements and provide over 10% energy savings for the overall production unit.

An experimental study was conducted by Murray and Groulx [87] to investigate the charging and discharging behaviour of the PCM, lauric acid, in a cylindrical latent heat energy storage system. Two copper tubes (one for charging the PCM with heated water and one for discharging with cold water) with horizontal circular fins were placed within the PCM which was encapsulated with a surrounding vertically oriented acrylic tube. It was found that natural convection was significant during charging (melting), and had negligible effect during discharging (freezing). This was concluded from the observed independence of PCM temperature on height within the enclosure for the discharging case.

1.5   Motivation and Knowledge Gaps

As previously discussed, in efforts to reduce GHG, thermal energy storage can play a crucial role in two major aspects, 1) to conserve energy from conventional fossil fuel sources and 2) to store energy from intermittent renewable energy sources to improve the reliability and consistency of clean energy supply. Specifically, solid/liquid latent heat thermal energy storage has shown to have distinct advantages over other storage methods. This type of storage does have challenges however, particularly due to the complexity of the underlying physical processes involved during phase change. The heat transfer during phase change is complex and transient, with varying magnitudes of conduction and convection from the simultaneous changes in liquid and solid fractions. The complexity is further increased with the non-linear behaviour of the solid-liquid interface. As well, during natural convection, the orientation of the heat source/sink plays an important role in the overall processes involved.

It has been found that while previous experimental studies have advanced the scientific understanding of the heat transfer processes during PCM phase change, a significant gap remains in our understanding of the underlying liquid flow behaviour. Previous studies are limiting as they primarily focused on temperature distributions within the PCM. From these studies the flow behaviour was only inferred from the temperature measurements and imaging. Detailed characterization of the fluid velocity behavior throughout the liquid PCM is vital from two fundamental aspects:

1) The knowledge of the fluid flow dynamics is vital in the understanding of underlying natural convection processes. Convection heat transfer is dominant over the conduction heat transfer and hence its characteristics significantly influence the overall heat transfer.

2) The flow patterns within the liquid domain governs the spatio-temporal dynamics of the solid-liquid interface, which in turn influence the melting/solidification process. Hence, the knowledge of the flow behavior provides a deeper insight into the melting/solidification behavior of the PCM.

Furthermore, numerical studies of PCM have acknowledged the limitations of the current numerical models to accurately capture the phase change processes [46], [88], [89], [90]. The numerical studies often accurately simulate melting behaviors at initial times. However, there is often an observed divergence between numerical and experimental results which typically increase both during times of strong natural convection and at later stages of melting. Detailed experimental characterization of the flow dynamics along with the temperature behavior can provide benchmark data that is invaluable for numerical studies through numerical model improvement. The knowledge advancement of the fundamental thermo-fluids processes during phase transition in a PCM-based thermal storage is essential to improve these energy storage systems for practical applications.

The present research is an effort towards this knowledge advancement by addressing some of the current knowledge gaps in the scientific literature related to the phase change process. While these knowledge gaps include both the charging and discharging aspects of a TES i.e. both melting and freezing processes of a PCM, due to experimental challenges, specifically during PCM freezing, the present research is focused on characterizing the melting behaviour of the PCM.

1.6   Thesis Objectives

The objectives of this experimental study are to:

1) Conduct a detailed investigation of the transient flow behavior in the liquid domain of phase change material during solid-liquid phase change (melting)
2) Conduct a detailed investigation of the transient thermal behavior of phase change material during solid-liquid phase change (melting)
3) Investigate the effects of heat source orientation on the transient heat transfer processes of natural convection-driven melting of the phase change material.

The liquid flow behaviour will be investigated through particle image velocimetry, a non-intrusive measurement technique used to quantify flow velocity. The thermal behavior will be studied through high-resolution thermocouple temperature measurements.

1.7 Thesis Layout

Chapter 1 provides background information on current energy supply, the need for energy conservation and renewable energy sources. The concept of energy storage is introduced and the role that this storage will play in the transition from convectional to renewable energy is highlighted. A summary of each type of energy storage is provided, and a comparison between each, with benefits and drawbacks, are discussed. A brief background of PCMs is provided and a literature review of solid-liquid phase change studies is included. Motivations, knowledge gaps and thesis objectives are also discussed.

Chapter 2 contains the methodology and experimental setup. Previous designs are discussed, highlighting the drawbacks which led to further iterations. The full details of the final experimental setup are presented, including the PCM enclosure, PCM properties, heating circuit, particle image velocimetry measurements, temperature measurements, experimental uncertainty, and data analysis processes.

Chapter 3 includes the results and discussion of recorded experimental data. Combined analysis of both velocity and temperature measurements enable a detailed discussion into the underlying heat transfer characteristics present during the melting of the PCM paraffin wax.

Chapter 4 summarizes and provides conclusions of the conducted study. Future recommendations are presented.

Chapter 2

2 Methodology and Experimental Setup

Experiments were conducted in a laboratory setting at the University of Western Ontario. Two primary experimental setups were constructed to measure and characterize 1) the fluid velocity fields within the liquid PCM region and 2) the temperature field within the entire (solid and liquid) PCM domain. The construction of the PCM enclosure, including materials, insulation, and the heat source, remained unchanged between both setups. Two enclosures were constructed to mitigate interferences between the Particle Image Velocimetry (PIV) imaging technique for velocity measurements and the temperature measurements.

2.1 Preliminary Experimental Setup Designs

Due to the novel approach of velocity fields measurement within liquid PCM, several iterations of the experimental setup, mainly the PCM enclosure, were considered before selecting the final version.

2.1.1 First Iteration

The initial design (see Figure 5) was a rectangular enclosure constructed primarily from acrylic and glass sheets and was used to contain the PCM, paraffin wax. A copper pipe (right side of enclosure, surrounded by black foam insulation in Figure 5) was utilized as both a vertical wall of the enclosure and a heat source with heated water pumped through it. This design was primarily utilized to investigate the behaviour of liquid PCM during melting and determine if PIV measurements were possible. The design did have drawbacks however, most notably the uneven shape of the heat source. The cylindrical copper tube, due to its convex shape, altered the overall fluid flow and did not provide a consistent, approximately 2D vertical heat source.
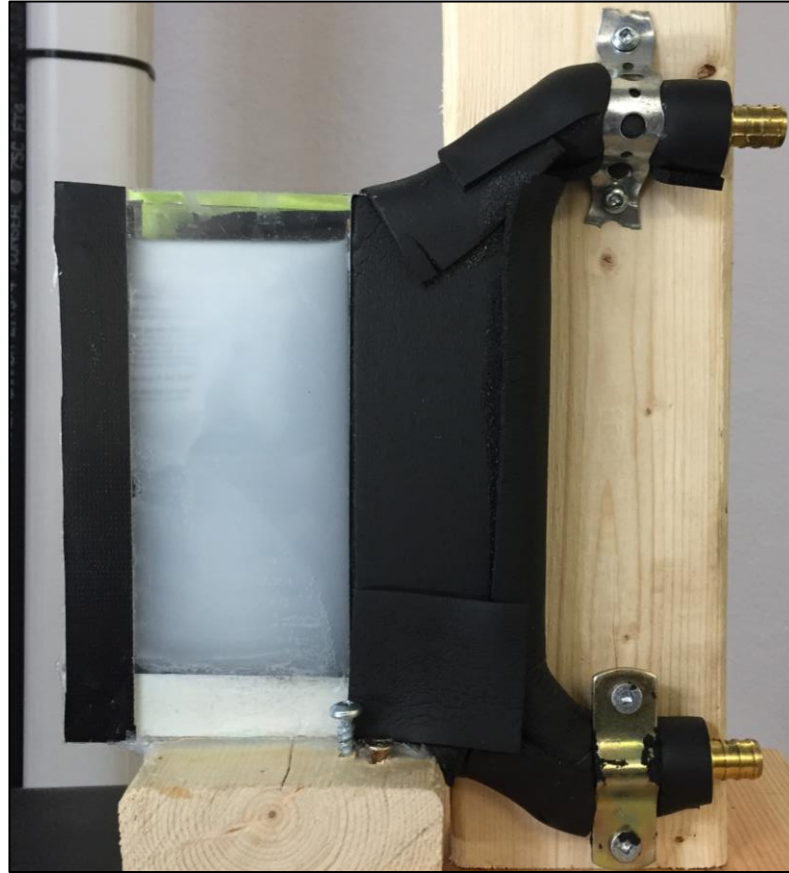
Figure 5: Initial PCM enclosure

2.1.2   Second Iteration

The second iteration of the PCM enclosure was constructed from a glass (front face) and acrylic (back face) sheet, both measuring 120mm high (H), 60mm wide (W) and 10mm deep (D). The left and bottom face of the enclosure was constructed from PVC plastic. The glass was chosen for its optical properties, with low distortion of the camera image. Again, paraffin wax was chosen as the PCM. In this iteration, the heat source was modified to address the previous issues of an uneven heating surface. A brass bar functioned as the heat source and a vertical wall, replacing the copper pipe. Instead, a copper pipe was brazed to the external face of the brass bar, and heated water was pumped through the pipe to provide the heat source.

Figure 6 highlights the copper pipe and brass plate. The camera positioning and field of view are also shown in Figure 6. As shown, the field of view did not extend the full height

of the PCM enclosure. A four-megapixel CCD camera was used, with a resolution of 2052 x 2048 pixels. To maximize the potential vector resolution within the liquid PCM, the studied field of view was reduced, capturing only the upper two thirds of the enclosure. As well, it was assumed that since the majority of the melted fraction would occur within the top of the enclosure, the chosen field of view would still allow sufficient velocity data collection. However, after data analysis, utilizing this experimental setup, it was discovered that the velocity behavior would require a full field of view for proper analysis and hence further testing was required.
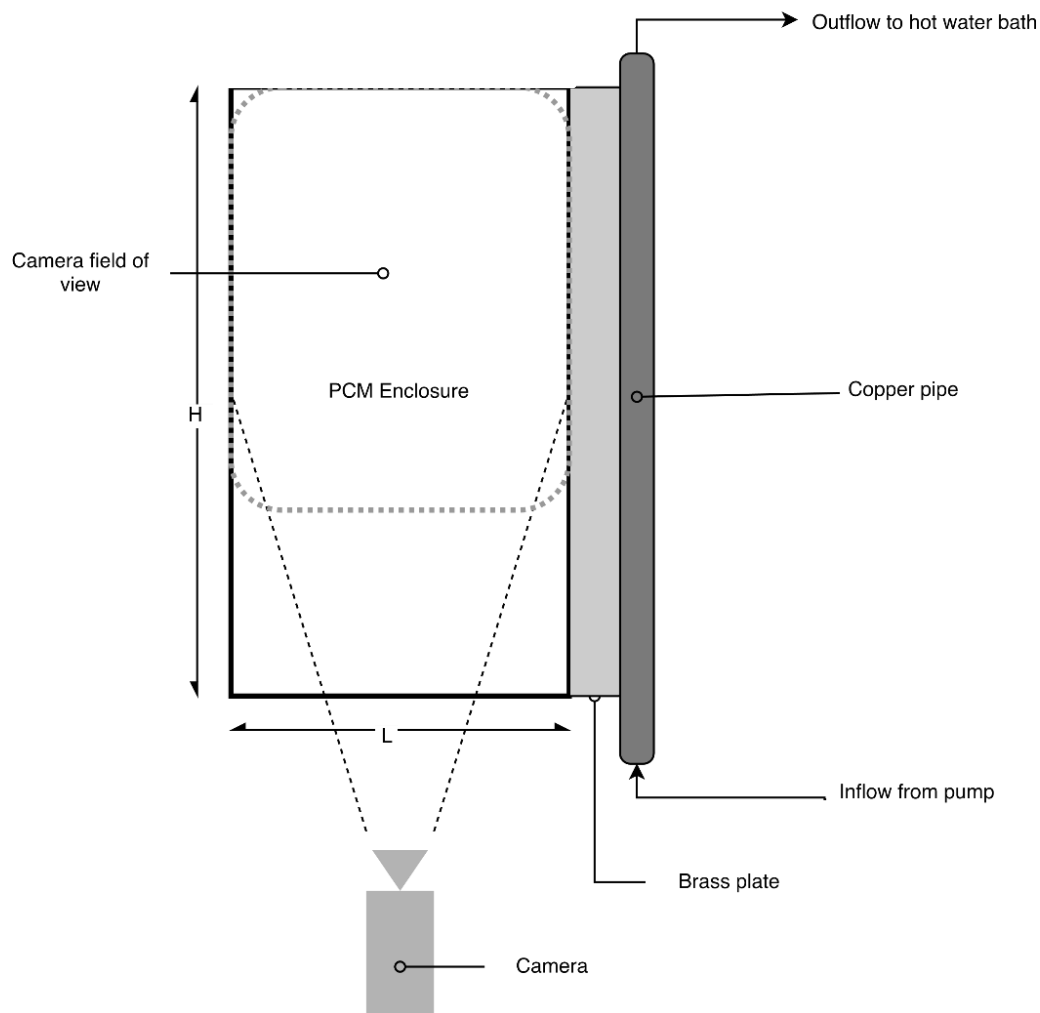
Figure 6: Schematic of the second iteration of the PCM enclosure

2.1.3   Third & Fourth Iteration

The third iteration the PCM enclosure expanded the captured field of view by changing the camera from a four to 12-megapixel sensor. As well, this iteration attempted to address the slow melting times experienced with the previous PCM, paraffin wax. Due to the relatively small temperature difference between the heated water (heated to a maximum of 80 Celsius) and the melting point of the paraffin wax (approximately 55 Celsius), the total melting times were in excess of 12 hours. This made prolonged capture of the velocity fields a challenge and resetting the setup between trials required several days to fully melt and solidify the wax. Hence, lauric acid was selected as a new PCM which has a lower melting point of approximately 43-44 Celsius [91]. Initially, the enclosure from the second iteration was utilized, however it was discovered that due to the acidity of lauric acid, the brass bar heat source rapidly corroded and dyed the PCM, rendering it useless for further experimental study (see Figure 7). As such, a new heating wall was designed and machined out of aluminum which is relatively resistant to the acidic PCM. This aluminum heater is discussed in further detail in the following sections. As well, the new enclosure was designed with only clear cast acrylic sheets, replacing the glass, allowing for a removable acrylic face which enabled full access to the PCM during reset between trials. The removable face was sealed through a malleable plastic gasket and bolts (see Figure 7). The gasket during prolonged heating, however, expanded, rendering the seal ineffective, and allowed lauric acid to leak from the enclosure. Hence, a fourth iteration was designed, maintaining the previous materials and heat source, while eliminating the gasket. Instead, the entire enclosure was permanently sealed with a high temperature resistant epoxy.
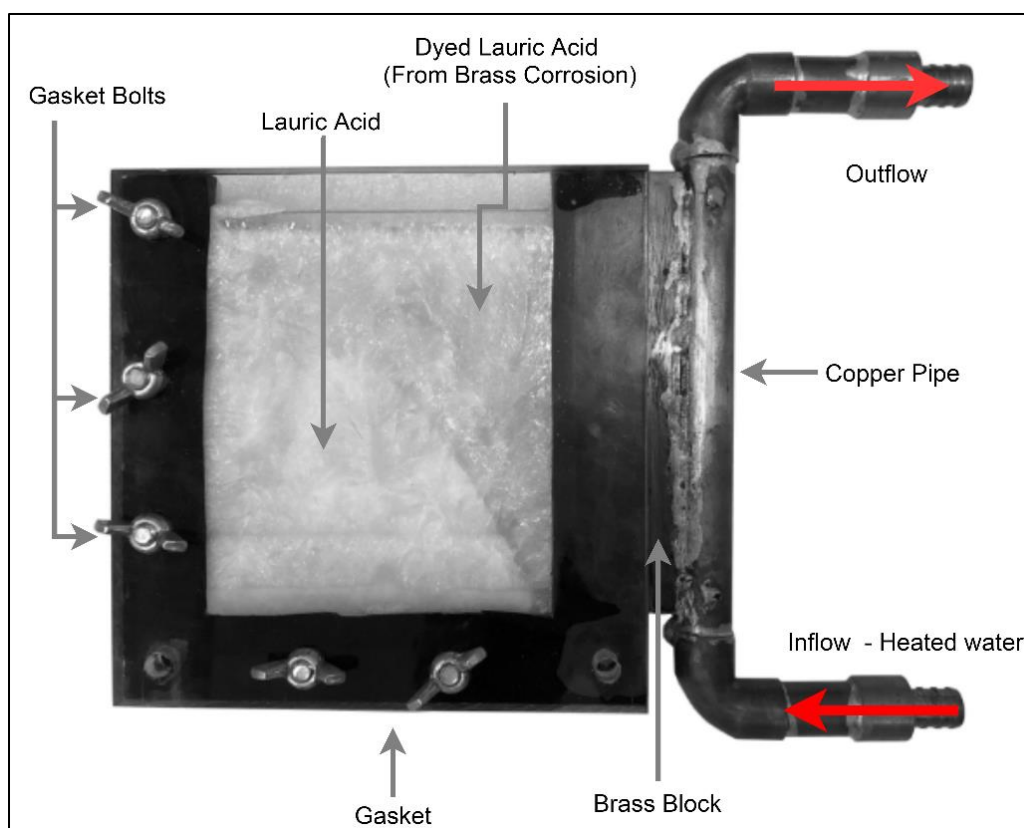
Figure 7: Schematic of third enclosure iteration

This trial proved successful in terms of data collection, allowing velocity data to be acquired during the lauric acid melting. Upon analysis of the data however, a major problem was discovered. It was found that the solubility of gases in the solid phase of lauric acid was significantly higher than in the liquid phase. As such, when the lauric acid was melted, dissolved gasses coming out of solution appeared in the liquid phase. These gases, appearing as bubbles in the camera images (highlighted in Figure 8), were similar in size to the tracer particles used in the PIV technique to show the fluid motion. Consequently, when processing the raw images, many of the bubbles would interfere with the analysis, generating false vectors as they rose to the top of the enclosure. Further post processing of the images to remove these false vectors was unsuccessful due to the large number of rising bubbles.

Bubbles from Dissolved Gasses
(Highlighted with red circles)

Figure 8: Highlighted bubbles from dissolved gasses during lauric acid melting

2.1.4   Fifth Iteration

Ultimately it was concluded that further analysis of the lauric acid would be unsuccessful and a fifth iteration was generated. This iteration utilized the same enclosure from the previous study, but replaced the lauric acid with the previous PCM, paraffin wax PCM. This design was the final iteration and was used for all analysis presented.

2.2   PCM Enclosure (Final Iteration)

A schematic of the final iteration of experimental enclosure, used in the study, is provided in Figure 9a. A thin, rectangular enclosure was constructed to contain the PCM and investigate its two-dimensional melting behavior. The internal dimensions of the chamber holding the PCM are 125mm tall (H), 75mm wide (W) and 12mm deep (D). The front, back, bottom and right walls were constructed from clear cast acrylic sheets (k ≈ 0.2 W/m.K). The thickness of the front and back panels was 6 mm while the bottom and right face were 25.4mm and 50.8mm, respectively. The top face of the chamber was left open to atmosphere, allowing for the expansion of liquid PCM during melting. The acrylic sheets were chosen for their low thermal conductivity, high resistance to heat degradation and zero impermeability to both solid and liquid PCM. Another important reason for choosing the clear cast acrylic was for its excellent optical properties, providing minimal distortion

of the captured camera images during both the PIV and temperature measurement. The left wall of the enclosure was constructed from a machined aluminum bar (k ≈ 205 W/m.K). This bar served as the heat source for the PCM. A square, 38mm section of the aluminum extended from the acrylic enclosure and within this region a hole was bored lengthwise to allow hot water to flow through the entire height of the bar, which served as the heat source.

The acrylic sheets were bonded together with an acrylic solvent glue, and the aluminum wall was epoxied directly to the acrylic sheets. This provided a leak proof design, which remained sealed when subjected to thermal expansion during heating.

The entire PCM enclosure, including aluminum heater, was further insulated with polystyrene boards (k ≈ 0.028 W/m.K), shown in Figure 9b. The polystyrene sheets were 25.4mm thick on each face. A section of the front and top faces was cut out of the insulation. This is highlighted as the semi-transparent cross hatched region in Figure 9b. This section was removed for short durations during imaging to provide optical access to the enclosed PCM (details will be provided later). Additionally, a 4mm thick sheet of fiberglass (k ≈ 0.038 W/m.K) was added to the sectioned cutout to reduce convective heat loss.
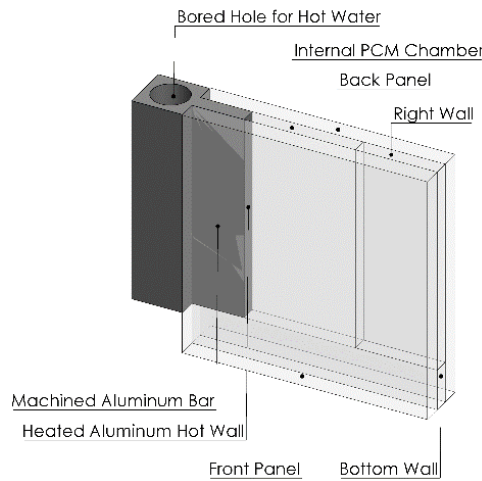
Figure 9a: PCM experimental enclosure (insulation removed)
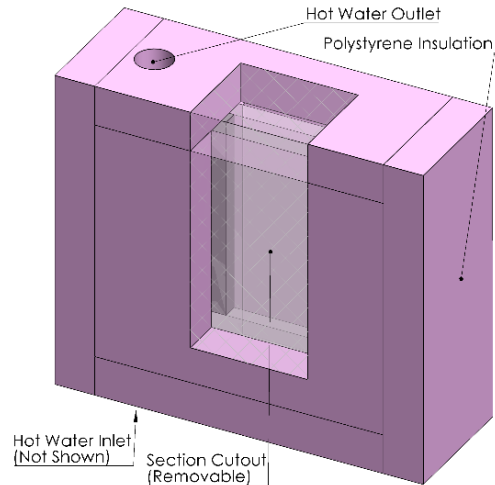
Figure 9b: PCM experimental enclosure with insulation shown

The PCM enclosure, camera, and PIV optics were mounted on a hinged steel frame, shown in Figure 10, Figure 11, and Figure 12. Figure 10 shows the full setup, including the heating circuit, steel frame, PCM enclosure and PIV laser light sheet. It is shown in the X-Y plane, providing a front view. Figure 11 displays the steel frame with optics, camera and PCM enclosure rotated at three angles. Figure 12 shows the same setup as the previous two figures, but in the Z-Y plane, highlighting the PIV optics and the camera supports. The hinged steel frame shown in both Figure 10, Figure 11 and Figure 12 allowed for the consistent alignment of all optics and camera positioning through adjustment of varying angles.

The frame is capable of pivoting between 0 degrees (horizontal) and 30 degrees (from the horizontal), counter-clock wise (CCW). To investigate the influence of the heat source inclination on the melting and associated heat transfer within the PCM domain, experiments were conducted at three different orientations of the PCM enclosure. These include, the heat source set at 0 degrees (vertical, no inclination), 8 degrees inclination and 18 degrees inclination. For an accurate comparison between each case, equal amounts of paraffin wax were required in the enclosure. An open top design limited the amount of PCM at increasing angles if overflow was to be prevented. Thus, the tilt angles 0, 8 and 18 degrees were selected to provide a discernable range of angles while still permitting a sufficient amount of PCM in the enclosure. The front view of the full frame supporting the PCM chamber, at all three tilt angles is shown in Figure 11. This frame facilitated an easy transition from 0 to 18 degrees without any need for realignments.

2.3 Thermal Energy Storage Medium

A commercially available mixture of paraffin wax and copolymer alloys in the form of white pellets, known as Polyfin, was utilized as the phase change material. The Polyfin, herein referred to as paraffin wax, was chosen as the PCM for its suitable visualization properties for PIV measurements. That is, in the solid state it has a white appearance and becomes transparent (optically accessible) in the liquid (molten) state. The average melting point of the paraffin wax is 55 Celsius. A summary of the Polyfin thermo-physical properties, as per published literature, is included in Table 1.

Table 1: Polyfin thermo-physical properties [55], [92]

Property	Value
Melting Temperature [°C]	55.0
Density $\left[\frac{kg}{m^3}\right]$	Solid: 934.5
	Liquid: 775.0
Specific Heat $[\frac{kJ}{kg \cdot K}]$	Solid: 2.78
	Liquid: 2.08
Thermal Conductivity $[\frac{W}{m \cdot K}]$	Solid: 0.24
	Liquid: 0.18
Kinematic Viscosity $[\frac{m^2}{s}]$	5.234×10^{-6}
Latent Heat of Fusion $[\frac{kJ}{kg}]$	180
Thermal Diffusivity $[\frac{m^2}{s}]$	8.4615×10^{-8}
Thermal Expansion $[\frac{1}{K}]$	0.778×10^{-3}

2.4 Heating Circuit

Shown in Figure 10 are the components for the heating circuit which was utilized to melt the PCM. A recirculating hot water bath was used to heat the aluminum block. Water was heated in an insulated glass tank with two submersed 1000W electric heaters (110V, 9A and 220V, 4.54A). The two heaters provided redundancy in the chance of one heater failure. The 110V heater (Model: C10 from Haake), contained a mixing impeller to provide an isothermal water bath. To maintain a constant water temperature, both heaters were controlled with a proportional–integral–derivative (PID) controller and feedback was supplied through a K-type thermocouple. The water bath was held at a temperature of 80 Celsius and it was observed that the water temperature remained within ± 1 Celsius of the set value during all experiments.

Water was pumped from the tank through a centrifugal pump, running at a constant flow rate of approximately 0.12 L/s. The water was carried through flexible, nylon braided hose, with an inner and outer diameter of ¼ and ½ inches, respectively. The hose was selected to withstand the high temperatures while minimizing heat loss. Water entered through the bored hole in the base of the aluminum block and exited through the top. For a given experimental run, the water was pumped from the tank into the heating circuit once the hot water tank reached a steady state temperature. Thermocouples were placed within the heating tank, and at the inlet and outlet of the aluminum block, to measure and monitor the temperature of the supplied water.
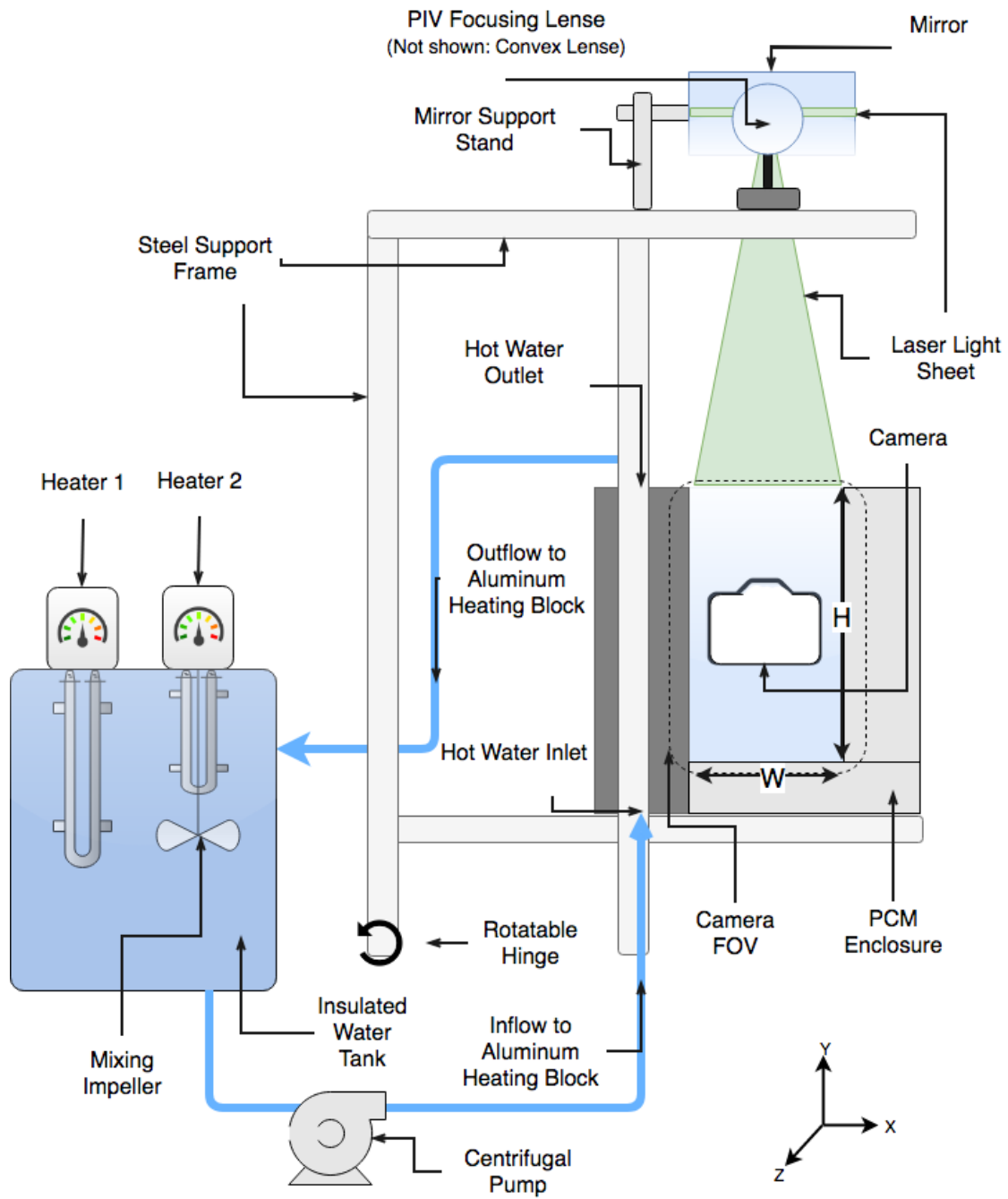
Figure 10: Complete experimental setup

0 Degree Tilt-Angle   8 Degree Tilt-Angle   18 Degree Tilt-Angle

Adjustable
Locking Hinge
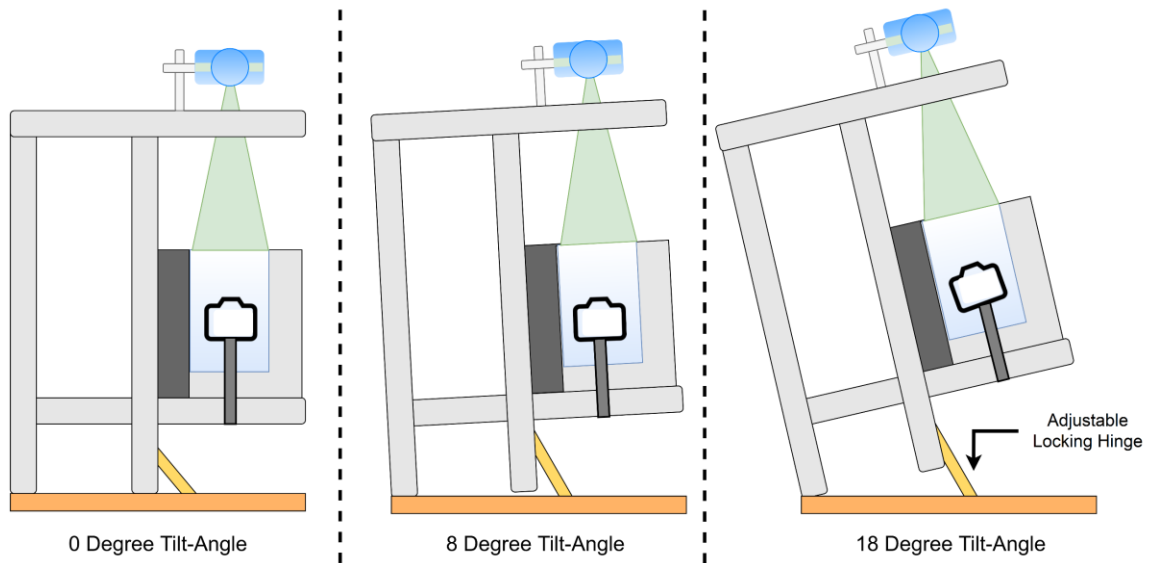
Figure 11: Schematic highlighting tilt angle of entire enclosure

2.5 Particle Image Velocimetry

Particle image velocimetry was utilized during the investigation of the transient flow behavior in the liquid domain of phase change material during solid-liquid phase change.

2.5.1 Working Principal of PIV Technique

Particle image velocimetry is a non-intrusive measurement technique, enabling the measurement and recording of instantaneous velocity fields in a cross-section of the flow with high spatial resolution. A typical PIV setup consists of a CCD camera, synchronizer, high power laser (light source), optics (to convert a laser beam into a light sheet), and tracer particles.

Small non-obstructive particles, referred to as seed or tracer particles, are introduced to the fluid medium where the flow velocity is under investigation. A laser light sheet is used to light a thin (~1-2mm) plane of measurement, illuminating the tracer particles and leaving the surrounding fluid and background dark. Due to their small size, the tracer particles are assumed to follow the fluid motion. A synchronizer connected to both a CCD camera and the laser, synchronizes both the camera frame recording and laser pulses. Hence, in a single exposure PIV recording technique, each camera image corresponds to a laser pulse. This

method essentially 'freezes' the particles in place, eliminating motion blur from fluid motion. Additionally, the frequency of the synchronizer controls the time delay between subsequent images and laser pulses. An instantaneous velocity field is then obtained by processing consecutive camera images (for example, image one and image two) and determining the particles displacement.

Analysis of PIV data involves search and interrogation windows. Image one is divided into regions called interrogation windows. Image two is divided into larger regions, generally twice the size of the interrogation window, called search windows. By cross-correlating between the interrogation region and search window in both images, a peak signal is produced, identifying the common particle displacement between images. Cross-correlation is computed for all interrogation and search windows to provide the displacement of particles in the full image. The velocity vector in each interrogation window can then be calculated since the time delay between images is known. Combining all velocity vectors from each interrogation window provides the overall instantaneous velocity field.

2.5.2   Implementation of PIV Technique

In the present study, silver-coated hollow glass spheres were used as the tracer particles. To prepare the PCM for velocity measurements, the paraffin wax was melted outside of the enclosure and silver-coated hollow glass spheres were introduced into the liquid phase. The glass spheres, with an average diameter of 13 µm, were fully mixed into solution in a separate container, providing an even dispersion throughout the PCM before being added to the enclosure. The silver coated spheres were used as tracer particles for the PIV measurements.

The PIV measurement system was comprised of a 120 mJ Nd:YAG laser (SoloPIV 120 XT) as the light source, a 12-Megapixel CCD camera (Flare, I O Industries) with a resolution of 4096 × 3072 pixels to capture images and a delay generator (Model 555 Pulse/Delay Generator) to control the timing of laser pulses. A horizontal stand, separate from the PCM enclosure, housed the laser and the delay generator. Figure 12 shows a side view of the steel frame with PIV components highlighted. The laser beam was directed at

the set of optical lenses affixed to the adjustable steel frame. The first optical lens (250 mm focal length, spherical lens, Thorlabs) reduced the diameter of the laser beam from 3-4mm to 2mm. The second lens (-12mm focal length, cylindrical lens, Thorlabs) split the beam into a horizontal light sheet. The light sheet (in the Z-direction), was directed towards a mirror, reflecting it vertically (Y-direction) towards the opening of the PCM enclosure. The light sheet spanned the entire mid-vertical plane of the enclosure.

The CCD camera was affixed on a rail, mounted to the steel frame (see Figure 12). The rail allowed the camera to traverse in the Z-direction, enabling the alignment of the camera field of view (see Figure 10 and Figure 12) to capture the entire PCM enclosure. Eight-bit images at a 12-Hz sampling rate were captured using an image acquisition system (DVR Express CORE, IO Industries) connected to a PC and controlled by an image acquisition software (CoreView, I O Industries). The raw images contained a colour channel, which was removed during export to greyscale images only.
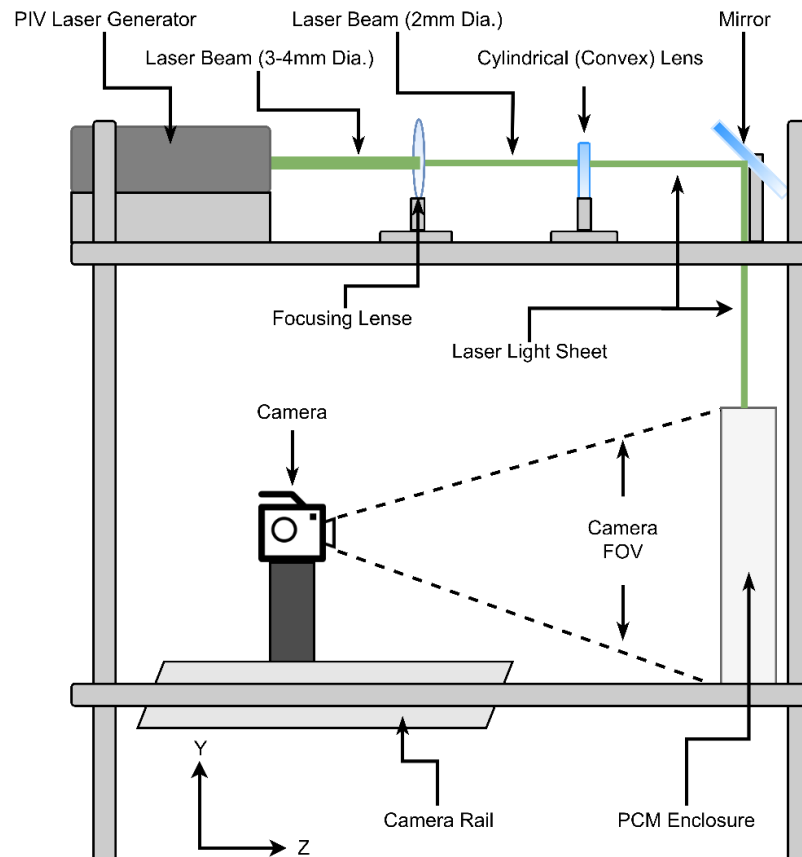
Figure 12: Experimental setup, highlighting PIV optics and camera mount

Due to the slow nature of the melting progression, its behavior and associated flow field were captured at discrete time intervals. The melting rate slowed over time, and the interval of image collection increased as the experiment progressed. From the beginning of the heating process to first 60 minutes, images were captured every 5 minutes, beginning at 15 minutes. This delay in initial imagining was due to the lack of melted PCM from 0 to 15 minutes. From 60-120 minutes, images were captured every 10 minutes. The remaining time intervals are as follows: 120, 140, 160, 180, 210, 240, 300, 420, 600 minutes. At each of these time steps, the top and front insulation cover was removed during imaging. The cover removal is necessary for the velocity measurements by allowing both the laser light sheet to enter the PCM chamber through the top of the enclosure and the camera to capture images of the PCM via the front wall. The images were acquired for 30 seconds and immediately after both insulation covers were reinstalled.

The periodic removal of the front and top insulation (even for the short duration) allowed heat to escape from the chamber. To investigate whether this heat loss influenced the overall melting behavior and the temperature field, a separate set of experiments were conducted where all insulation covers remained in place throughout the entire melting process. The time history of the temperature data at each thermocouple location was compared between the two cases, i.e. periodically removed and permanent insulation on the front and top cover. Figure 13 shows the time history of the temperature variation at three TC positions, along the mid-horizontal plane of the enclosure for the two cases. The results show that the trends of temperature variation with time are nearly identical, a strong indication that the melting behavior in both cases is similar. The comparison of the instantaneous temperature magnitudes between the two cases show slightly higher PCM temperature for the permanent insulation case, which is expected. However, the statistical analysis using the data from all thermocouples show that the average difference in the temperature magnitude is approximately 2.0% of the mean PCM temperature, which varied between 1.0% and 4.3%. These results confirmed that the periodic removal of the front cover (for short times) has minimal impact on the melting behavior inside the PCM enclosure.
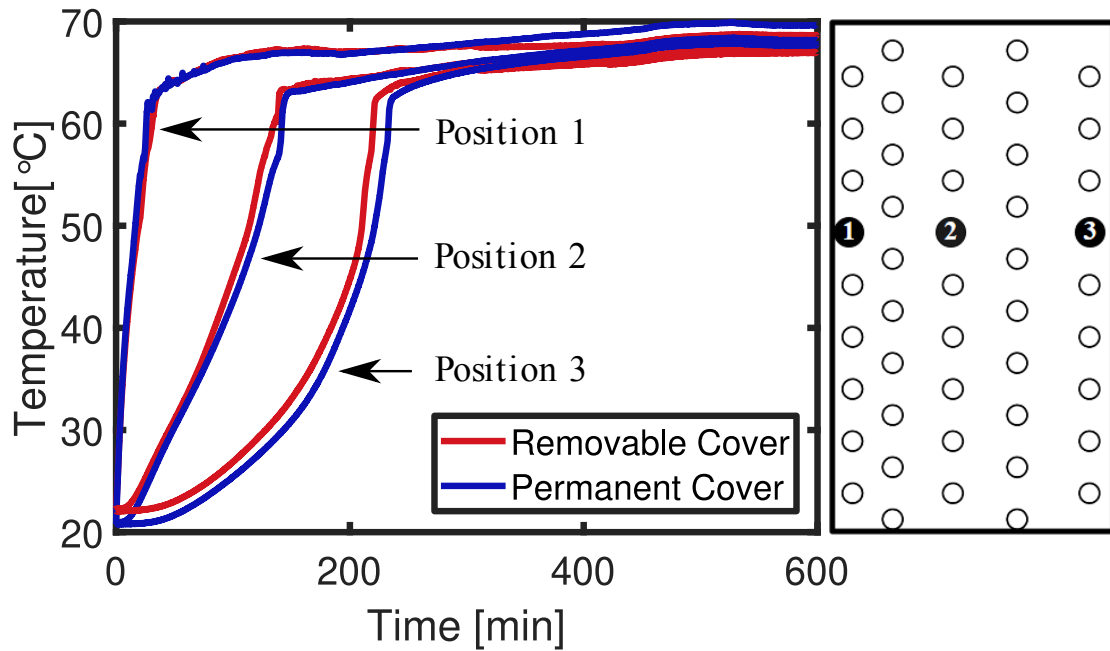
Figure 13: Temperature profiles at three TC positions along the mid-horizontal plane of the enclosure for periodically removed and permanent insulation cover. Right side of figure highlights the three TC positions within the enclosure.

2.6   Thermocouple Temperature Measurements

The second set of experiments were focused on quantifying the temperature field within the PCM domain, utilizing the enclosure, support frame and heating circuit from the velocity measurement study. Temperature measurements were conducted using 64 independent Neoflon-PFA insulated T-type thermocouples (Omega Engineering), referred herein as TC. A wire gauge of 36 AGW was selected to minimize interference between the TC probes and the liquid flow of PCM. Each TC was rated for special limits of error (SLE) which corresponds to a temperature accuracy of ±0.5 Celsius. The thermocouples were constructed separately from the PCM enclosure and were initially calibrated using an isothermal water bath from InnoCal (Model #14576-00). The bath was varied from 25 to 80 Celsius in 5-degree increments. All 64 thermocouples were placed within the hot water bath. At each 5-degree increment, temperature measurements from all TCs were simultaneously recorded and time averaged over 30 seconds. These 12 temperature increments were used to determine a calibration equation for each thermocouple. The

results show an almost linear trend for all calibration equations. However, it was later determined that the temperature reading from the InnoCal was biased, and as such provided temperature measurements significantly lower than that of the 64 TCs. The maximum standard deviation of the recorded TC temperatures was 0.35 Celsius; less than the manufacturer stated accuracy of ±0.5 Celsius. Therefore, the TC temperature readings were compared with the known PCM melting temperature to determine accuracy. Comparison between the recorded TC temperatures and the melt fraction from camera images was conducted, finding good agreement between both. As such, it was determined that the temperatures recorded by the TCs were accurate, with little bias, and therefore did not require a third-party calibration.

Within the PCM enclosure, 47 thermocouples were arranged in a staggered grid pattern using 5 columns alternating between 9 and 10 rows. The spacing and TC locations are highlighted in Figure 14. The thermocouples were inserted into the PCM domain through holes drilled in the acrylic at the back of the enclosure. They were placed at a depth of 3mm, corresponding to the midplane of the paraffin wax. The column grid spacing was varied depending on the distance from the hot wall. It was assumed that the largest temperature gradients would exist in the region closest to the hot wall. Therefore, TC spatial resolution increased with increasing proximity to the heat source. A column of 10 TCs, denoted by red markers in Figure 14, were placed directly to the hot wall and epoxied to the surface of the aluminum bar. OmegaBond 101 epoxy (Omega Engineering) was used to secure the TCs to the hot wall. These TCs were used to measure the surface temperature of the hot wall.

Four TCs were utilized to estimate the heat transfer from the PCM enclosure to the surroundings. Two TCs placed on the inside and two on the outside of the insulation measured the temperature gradient through the insulation during PCM melting. One TC measured the ambient air temperature, and two TCs placed within the hot water supply line were used to record the inlet and outlet temperature of the heated water pumped through the aluminum block Heat losses to the surroundings were calculated to be approximately 1.34 kJ for the 0-degree tilt angle case which experienced the longest melting. This is approximately 7.4% of the total heat absorbed by the paraffin wax during melting. Further

discussion of the total absorbed energy for each tilt angle is provided in Chapter 3, however the results show that heat losses to the surroundings was minimal and did not significantly influence the overall melting behaviour.
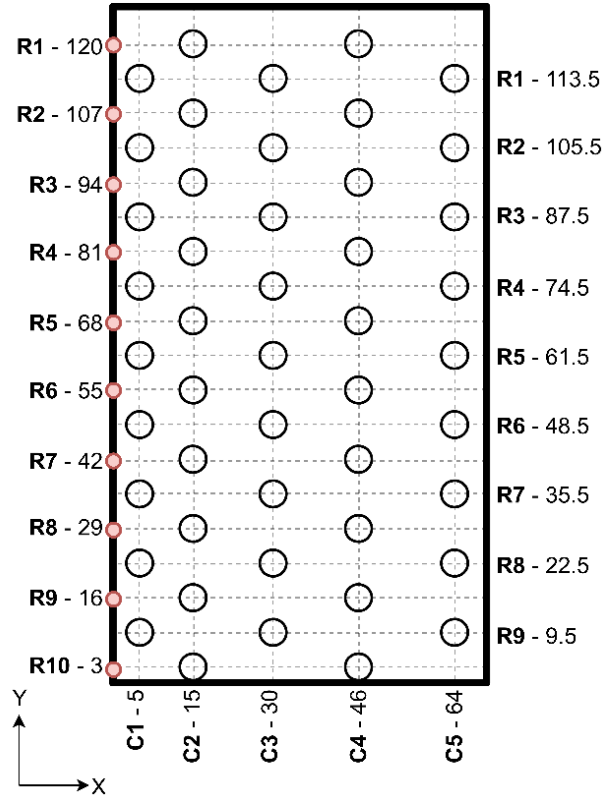
Figure 14: Thermocouple horizontal and vertical spacing within PCM enclosure. All values are in mm.

Data acquisition for all temperature measurements, including temperature measurements from the PIV study, were conducted using four separate, 4-Channel National Instruments NI9211 and three, 16-Channel National Instruments NI9214. The sampling rate for all modules was synchronized to record temperature measurements every 1 second for the full duration of the study via LabVIEW. Temperature measurement recording was conducted at three angles of hot wall inclination, 0 degrees, 8 degrees and 18 degrees, matching the angles from the PIV study.

2.7   Experimental Uncertainty

The uncertainty in the velocity values was calculated for all cases (0, 8 and 18 degrees). Using the results of Cowen and Monismith [93] and Prasad et al. [94], the uncertainty was estimated to be 0.31 pixels, corresponding to approximately 1.73% of the average mean resultant velocity presented. As the light sheet was passing through two different mediums, air and liquid PCM, with a moving air-PCM interface (free surface), there was potential for light sheet distortion in the liquid domain. It was observed that for all cases, despite the movement, the free surface remained flat (also confirmed from PIV images). Hence, the free surface did not cause any distortion of the laser light sheet inside the liquid PCM domain.

The uncertainty in the temperature values is from a combination of both the TC uncertainty, and the data acquisition hardware. As provided by National Instruments, the data acquisition uncertainty is typically ±0.35 Celsius and ±1.1 Celsius for the NI9214 [95] and NI9211 [96], respectively. This uncertainty, as stated by National Instruments, accounts for gain errors, offset errors, differential and integral nonlinearity, quantization errors, noise errors and isothermal errors [96]. Therefore, accounting for the uncertainty in the TC themselves, the total uncertainty is ±1.6 Celsius and ±0.85 Celsius for the NI9214 and NI9211, respectively.

2.8   Data Analysis

2.8.1   PIV Velocity Fields

Instantaneous velocity fields were computed by cross correlating two images of a given image pair using an in-house computer code operated in the digital image processing software, Heurisko (Aeon, Germany). An interrogation window of 32×32 pixels, a search window of 64×64 pixels and a grid space of 16 pixels (with 50% overlap) were used. This corresponds to a resolution of 0.73mm $\times$ 0.73mm of the velocity vectors field.

The velocity fields at each discrete time interval were obtained from 22 seconds of imagining at 12 Hz sampling rate, corresponding to 264 captured images. This produced 132 velocity fields, at each discrete time interval. The mean velocity field over a given time

interval was calculated by time averaging the velocity vectors at each grid point over 132 instantaneous velocity fields. As the time-scale of the melting process was very large (i.e. several hours), the velocity changes within the 22 seconds of data were found to be very small (almost negligible). The prime purpose of time-averaging over this short interval was to remove noise from the velocity field at a given discrete time. Hence, the mean velocity field is still a representative of the instantaneous velocity field at a given discrete measurement time.

A sample PIV image is shown in Figure 15(i). As figure shows, the regions of solid and liquid PCM are distinguishable due to the distinct gray values associated with each phase. An in-house image processing algorithm, developed in the MATLAB environment, facilitated the automatic detection of the solid-liquid interface by exploiting the distinct gray values of each phase. The solid-liquid interface detected by the algorithm is depicted in Figure 15(ii). A script was created to generate a binary image (Figure 15(iii)) through segmentation between the two phases of solid and liquid. The solid PCM was marked as the white region and the liquid PCM was marked as the dark region. These binary images were used as masks to exclude velocity vectors that were outside the liquid domain, since those were false vectors.
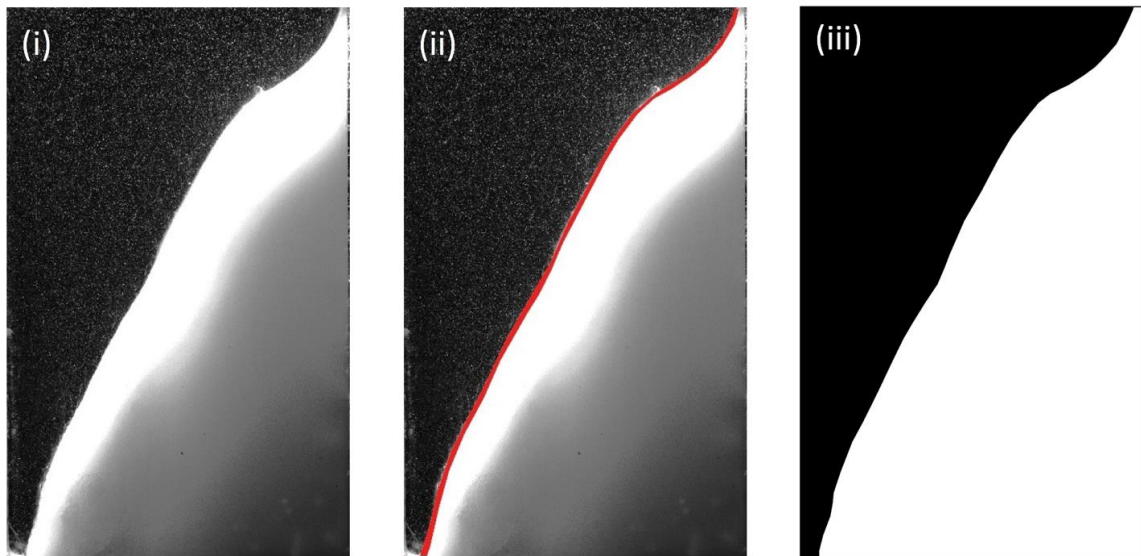
Figure 15: Original capture image (i), interface detected image through algorithm (ii) and generated binary image (iii)

2.8.2   Plotting of the Velocity Data

The plots of velocity vectors and contour plots of resultant velocity were generated from the mean velocity fields. In all plots, the light grey region denotes an area within the enclosure, but above the free surface of the liquid wax. To provide a proper comparison between all angles, the 0-degree cases were not fully filled to match the volume of the angled trials. Therefore, this grey region is visible in all cases. A black region corresponds to the solid, nonmelted wax and highlights the generated mask region where false vectors were removed. To improve the visual clarity by decreasing overlapping vectors, the resolution of the velocity vector plots was reduced by removing every other column and row of vectors.

2.8.3   Temperature Field Data

The temperature field at each angle and each discrete time was calculated through the recorded thermocouple data. As mentioned earlier in the experimental setup, 47 thermocouples were placed at discrete locations within the PCM domain. For a better perception of the temperature field, the temperature data was expanded to a grid of 635×350 via interpolation, covering the entire 127mm by 70mm enclosure domain. Each grid position corresponds to 0.2mm of the enclosure field. A natural neighbor scheme was utilized for the interpolation.

Unlike the velocity data, both solid and liquid regions were included in the temperature fields. The temperature data at locations above the liquid surface in the enclosure were excluded and the corresponding area were denoted by the same light grey as the velocity data.

2.9   Conclusions

Different experimental setups were constructed to measure and characterize the velocity field within the liquid PCM and the temperature field within the entire PCM (solid and liquid) domain. Construction of the enclosure progressed through five iterations before the final design was selected. It was found that specific attention regarding enclosure material and its resistance to corrosion should be considered when using PCMs which are acidic in nature. Additionally, the selection of the PCM in regards to PIV measurements is important to note, as not all PCMs are suitable for velocity measurements due to undesirable properties. This may include a low solubility of dissolved gasses which can cause the formation of air bubbles that interfere with the instantaneous velocity calculations.

The final design of the PCM enclosure utilized clear cast acrylic sheets for their resistance to corrosion and optical accessibility for PIV measurements. An aluminum bar was used as the heat source for its high thermal conductivity and corrosion resistance. A hot water bath with a PID controlled heater was implemented to provide a consistent heat source. The entire enclosure, including PIV optics and thermocouple measurement devices, was mounted on a hinged steel frame which could be rotated. This aided in the investigation of heat source orientation on the PCM melting process by allowing a consistent experimental setup through multiple tilt angles.

Velocity measurements were recorded through the PIV technique, utilizing a synchronized laser and camera to capture images of the liquid PCM domain. Both the velocity fields and resultant velocity plots were generated from the processed PIV data. Temperature data was recorded through thermocouples which were imbedded into the PCM domain. Interpolated temperature fields were generated from the recorded thermocouple measurements.

A full experimental uncertainty analysis was conducted for both the recorded velocity measurements and the recorded temperature measurements. Results show that the uncertainty was minimal and that the measured data was suitable for further analysis which is presented in Chapter 3.

Chapter 3

3 Results and Discussion

The high-resolution simultaneous imaging and temperature fields allowed for an in-depth qualitative and quantitative analysis of the transient melting process inside the PCM enclosure.

3.1 Spatial-Temporal Behavior of the Transient Melting Process

Heat was first transferred to the PCM via conduction, following the onset of heating from the hot aluminum wall. Figure 16 shows the temperature contours 5 minutes after the onset of heating, for all three tilt-angles of the enclosure. As expected, the plots show a strong temperature gradient in the horizontal direction due to the conduction heat transfer. Additionally, the results show that the temperature contours remained almost parallel to the hot wall, an indication of one-dimensional conduction. However, near the top of the PCM domain, adjacent to the PCM surface, the contours show a greater heat diffusion, visible in the deviation from a dominant horizontal temperature gradient. This increased heat diffusion is likely a consequence of heat transfer to the air which resided above the PCM in the enclosure (denoted by the grey region). It is probable that convection currents developed, enhancing the heat transfer from the top layer of the PCM and caused a higher heat diffusion.
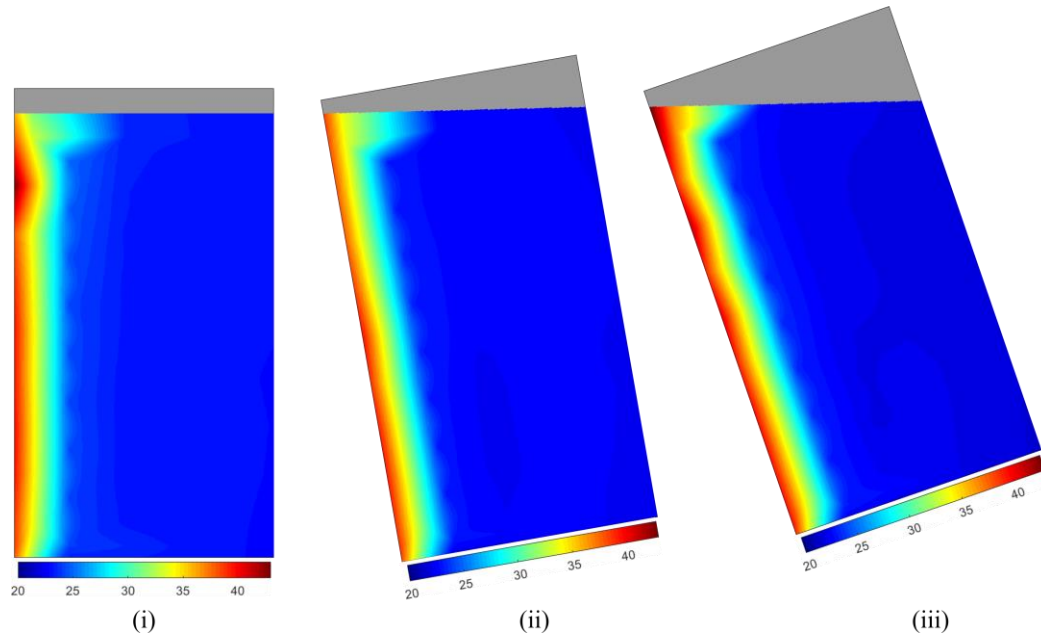
Figure 16: Temperature contours at 5 minutes of melting for tilt angles of (i) 0-degrees, (ii) 8-degrees and (iii) 18-degrees. Units in [°C].

As the heating continued, the temperature of the PCM rose with the spatial extension of the temperature gradients in the horizontal direction. Once the temperature of the PCM adjacent to the hot wall reached the melting temperature, the phase change started and a thin layer of liquid PCM formed next to the hot wall. Due to the small thickness of this layer, which was confined between two stationary boundaries, the viscous effects were dominant over the buoyancy force causing the liquid region to remain stationary. As a result, conduction was the primary mode of heat transfer to the PCM and the thin melted region remained parallel to the hot wall. This melted region was most prevalent at earlier times. As time progressed, the buoyancy effects increased in magnitude and became significant. Figure 17 shows the temperature contours 20 minutes from the onset of heating where the temperature of the PCM adjacent to the wall had surpassed the melting point, and a liquid region develops along the hot wall. The plots show that the temperature contours remain almost parallel to the hot wall over most of the height except near the top, where the heat diffusion region extended further. The expansion of this region is likely due to the combined effect of buoyancy-driven transport of heat to the top as well as the heat transfer due to the air at the top of the enclosure. However, at these early times of melting,

conduction remained the primary mode of heat transfer in the bulk of the domain. Note that the heat loss from the top to the confined air was considerable only in the very early stages of heating.
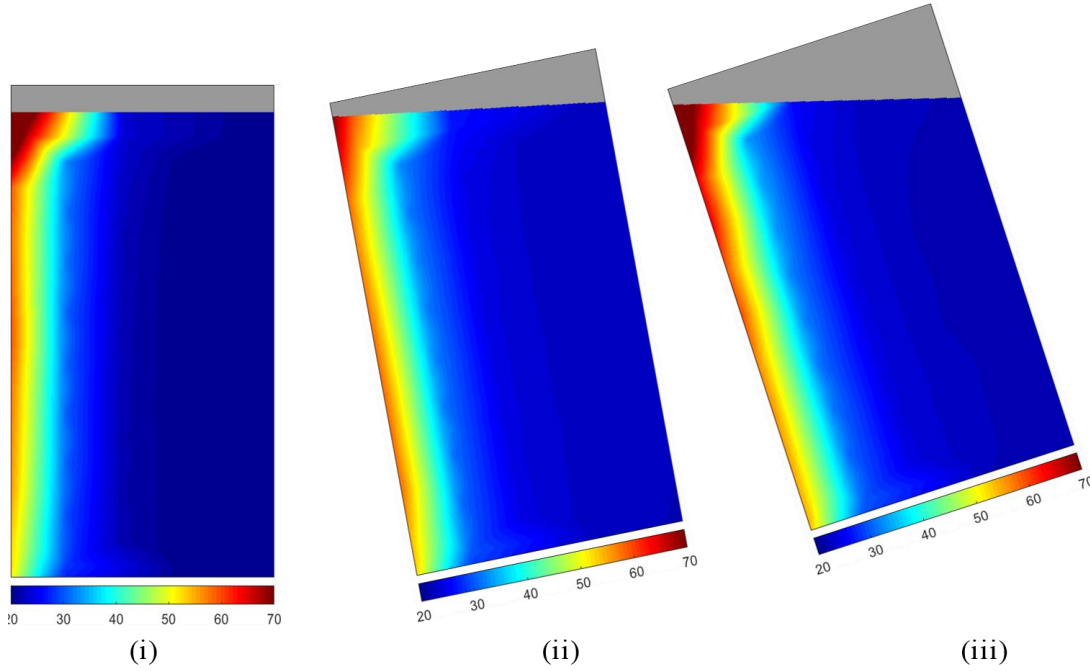
Figure 17: Temperature contours at 20 minutes of melting for tilt angles of (i) 0-degrees, (ii) 8-degrees and (iii) 18-degrees. Units in [°C].

Figure 18 to Figure 22 present the two-dimensional velocity field and contours of resultant velocity and temperature field at given instances of time during the melting process. At a given time, each row corresponds to a tilt angle of the PCM enclosure and the time instances presented range from 40 to 600 minutes. By 40 minutes (Figure 18), this vertically melted region, parallel to the hot wall, is only visible in the lower two-thirds of the chamber for all angles. The temperature gradients at this point of melting are still minimal in the vertical direction, and the primary temperature gradient exists only in the horizontal direction (see temperature contours in Figure 18). The initial conduction dominant heating is observed in all three enclosure angles and the orientation of the heat source for the 8 and 18-degree case do not appear to enhance this conductive melting.

As conduction heating progressed and the melted region grew, a growing amount of liquid PCM was propelled by the increasing buoyancy forces, which exceeded that of the viscous forces. This led to the induction of buoyancy-driven natural convection which is shown beginning within the top of the enclosure in Figure 17 and growing in magnitude in Figure 18.

As the buoyancy-driven vertical flow reached the upper surface of the liquid PCM, due to its impermeable nature, the flow was diverted in the horizontal direction towards the solid PCM, satisfying mass conservation. The temperature of the diverted flow decreased upon contacting the cooler, solid, upper boundary. This temperature decrease resulted in a density increase, and the descent of the heavier liquid created a recirculation zone within the top of the enclosure (see Figure 18).

The buoyancy-driven flow gained prominence with an increase in time. At 80 minutes (Figure 19), both the velocity vector and resultant velocity plots show a significant increase in the PCM velocity magnitude along the hot wall. This increased velocity translates to an increase of liquid PCM within the top of the enclosure causing the top recirculation region to grow. The temperature plots in Figure 18 and Figure 19 show an increasing region of hot PCM within the top of the enclosure. This recirculating region of PCM is responsible for the growing concave-shaped melt interface observed in Figure 19.

Figure 18: Velocity field, resultant velocity, and temperature field for (i) 0-degrees, (ii) 8-degrees and (iii) 18-degrees at time 40 minutes. Velocity plot units in [cm/s], temperature plot units in [°C].

As melting progressed, and the hot liquid contacted the cooler, solid PCM, further melting is induced. Heat is transferred from the warm liquid PCM causing it to cool and increase in density. This is visible in the temperature plots, which show a region immediately adjacent to the solid interface that contains cooler, liquid PCM. Figure 19 shows that there is an average temperature reduction of approximately 9 degrees Celsius between the center of the concave melt region, and the solid/liquid interface. The liquid parcels, now denser then the surrounding fluid, descend from the top of the enclosure. As they descend along the solid interface, additional heat is lost at the boundary, further increasing their density, and accelerating the flow. This is visible in the resultant velocity plots; the velocity of liquid PCM along the interface shows an increase as it descends from the top of the enclosure. Results in Figure 19 show that the velocity magnitude increased by approximately 300% as the PCM descends from the top to the mid height of the enclosure at all three enclosure angle configurations.

These descending PCM parcels, due to mass conservation, replace the rising plume of PCM adjacent to the hot wall. As the parcels descend they force the flow along the solid interface towards the hot wall where the cooler fluid parcels are reheated and begin to rise. This entire process creates a primary recirculation region along the boundaries of the enclosure and is responsible for the distinct melt patterns observed. The recirculating flow accelerates the transport of heat from the heat source towards the solid PCM, resulting in the enhancement of melting and heat transfer across the domain. As the time further progressed, the established recirculation region, driven by natural convection, grows further and becomes the primary heat transfer mode.
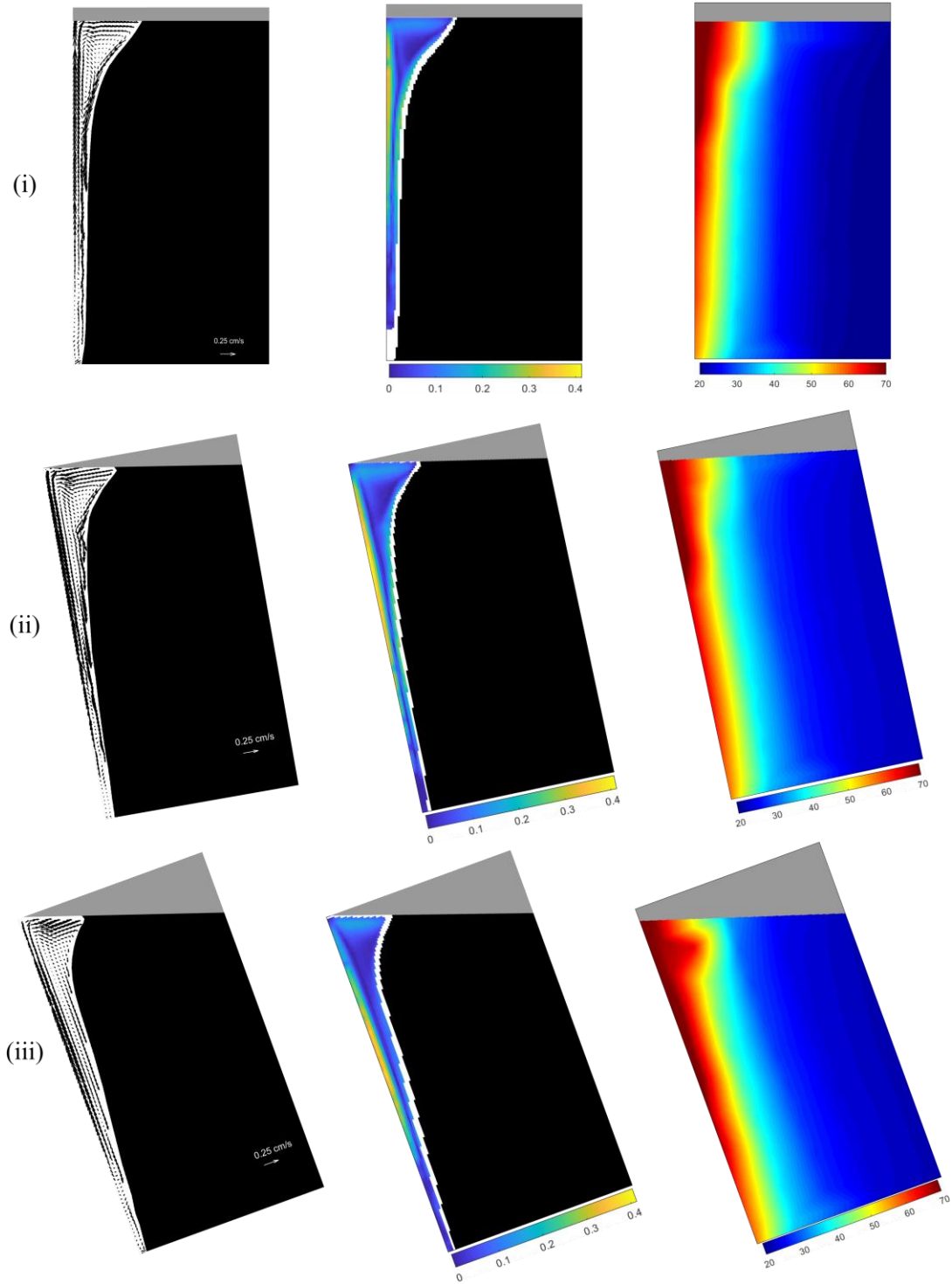
Figure 19: Velocity field, resultant velocity, and temperature field for (i) 0-degrees, (ii) 8-degrees and (iii) 18-degrees at time 80 minutes. Velocity plot units in [cm/s], temperature plot units in [°C].

With time increase, the melt front reaches the far wall of the enclosure, shown in Figure 21. Comparing the temperature fields between Figure 20 and Figure 21, there is a growing region of warm liquid which remains at the top of the enclosure. This growing region of warm PCM is consistent across all enclosure tilt angles. Heated PCM parcels are transported to the top of the enclosure where they remain above the cooler PCM. With the solid PCM no longer present in this region, there is no major heat sink, and the warmed PCM forms stratified liquid layers. However, with increasing enclosure tilt angle, these stratified layers of hot PCM become less prominent. This is likely a cause of the increased strength of recirculation and natural convection observed for the 8 and 18-degree cases and it is probable that this increased natural convection can be attributed to two primary factors:

First, with an angle above 0 degrees (vertical), the buoyancy driven PCM is accelerated vertically, therefore having velocity components both parallel and perpendicular to the hot wall. Thus, instead of moving parallel along the full length of the heater, as shown for the vertical wall, a fraction of the heated PCM separates from the hot wall, rising vertically under the influence of buoyancy. As a result, the high velocity fluid stream tends to become wider, losing its magnitude along the hot wall. In turn, more of the warm fluid parcels rise above the inclined heat source and penetrate into a larger body of the melted PCM above. This increased advection from the hot surface is visible in both the resultant velocity and temperature contour plots. With increasing tilt angle, a higher flow, distributed over a larger region, is observed in Figure 19 through Figure 22, for the 8 and 18-degree cases, when compared to 0-degrees. Furthermore, the temperature fields along the hot wall show that the heated PCM is distributed over a larger region.

Secondly, the enclosure recirculation is increased through the descending PCM along the solid-liquid interface. In the vertical orientation, the PCM is forced to follow the solid-liquid interface. However, with increased enclosure angles, a fraction of the cooler PCM can sink directly towards the hot wall, without following the full recirculating flow stream around the liquid domain.

Figure 20: Velocity field, resultant velocity, and temperature field for (i) 0-degrees, (ii) 8-degrees and (iii) 18-degrees at time 120 minutes. Velocity plot units in [cm/s], temperature plot units in [°C].
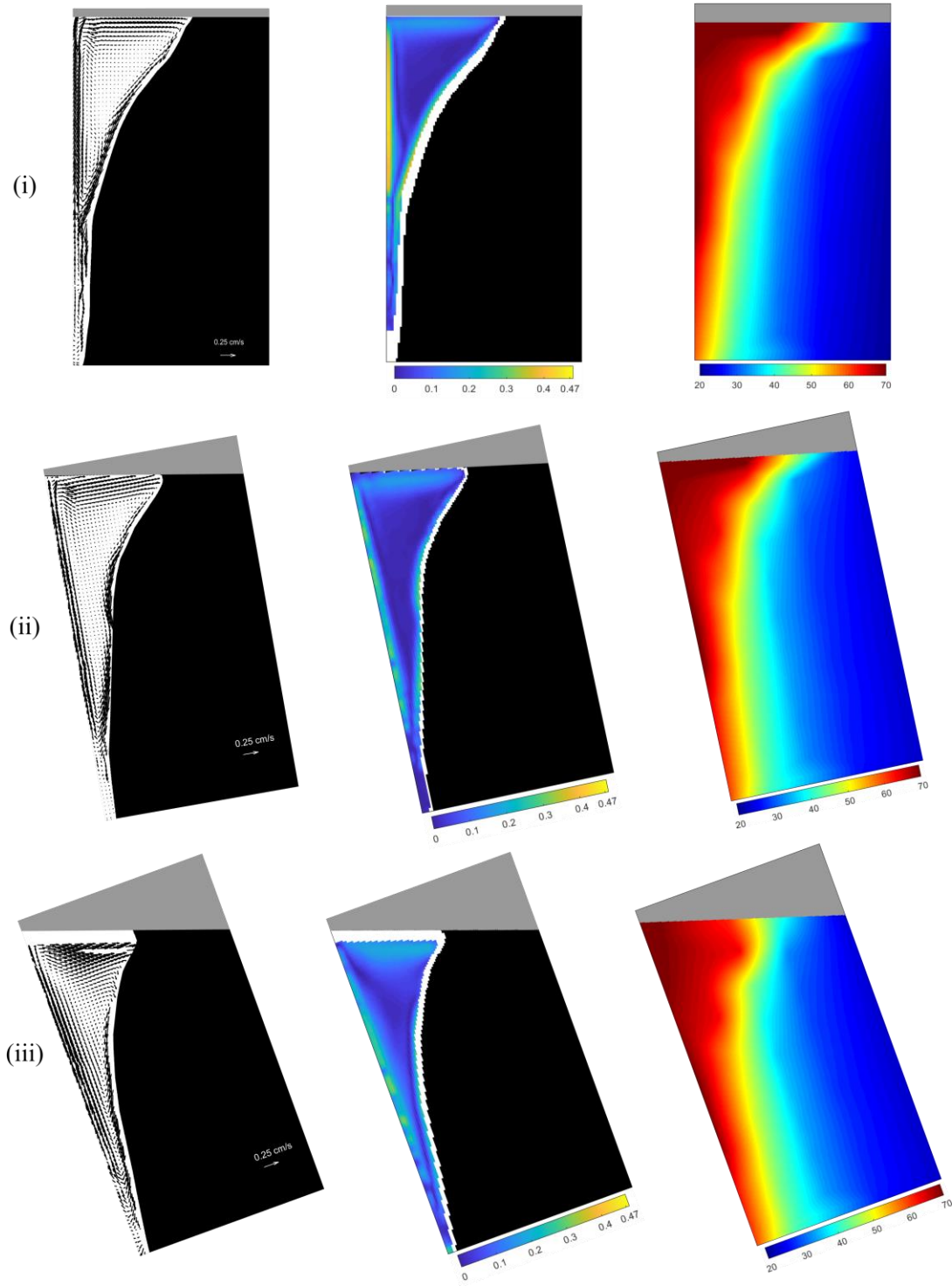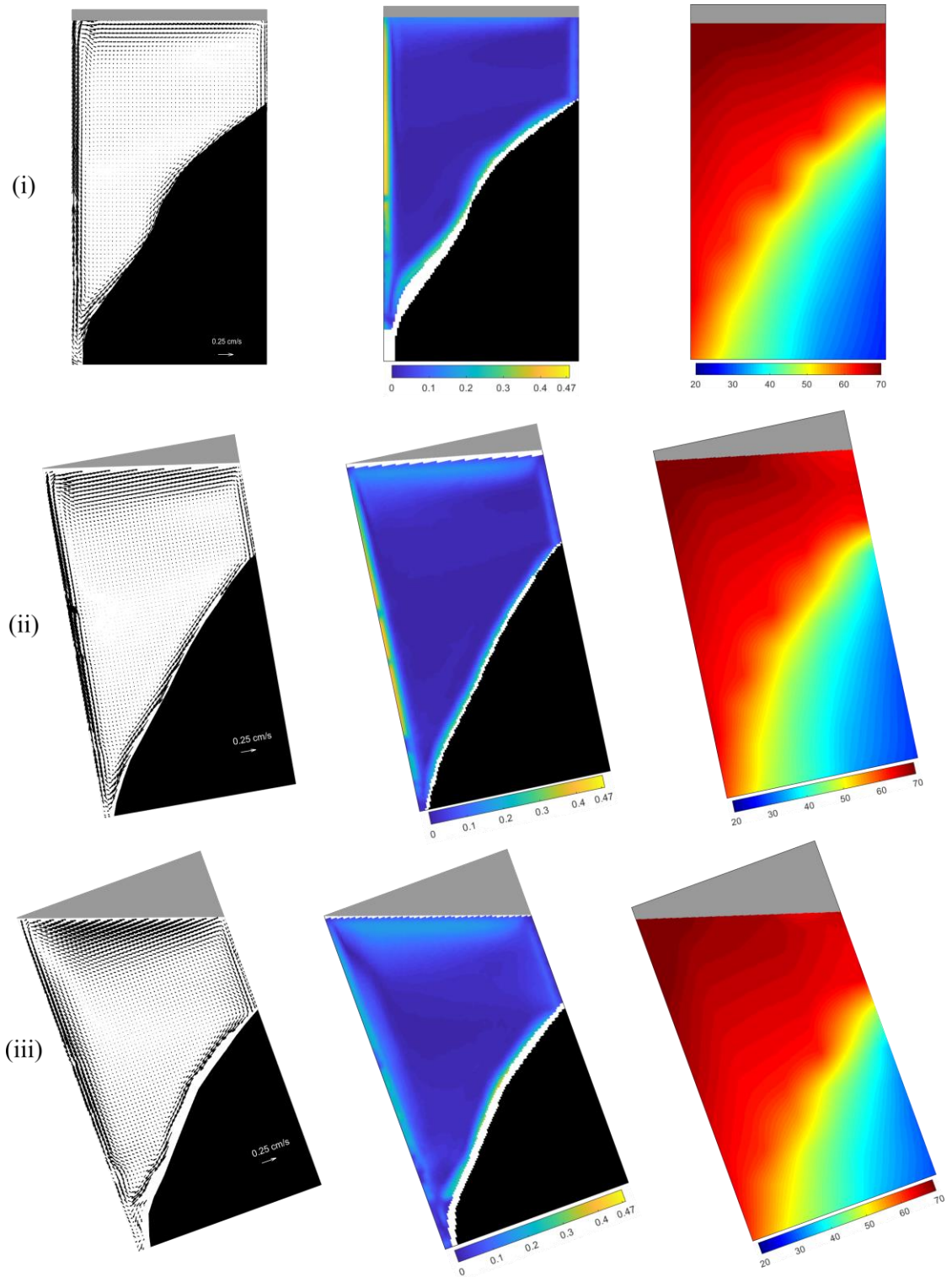
Figure 21: Velocity field, resultant velocity, and temperature field for (i) 0-degrees, (ii) 8-degrees and (iii) 18-degrees at time 240 minutes. Velocity plot units in [cm/s], temperature plot units in [°C].

Because of the boundary recirculation region, an angled solid-liquid interface is created in the top region of the enclosure. This feature of the interface was responsible for the formation of a distinct vortex between the angled interface and the hot wall. The sinking PCM parcels, below the concave melt region, are redirected towards the hot wall where they are reheated and begin to rise. This generates a prominent, clockwise vortex, which causes a flow diversion and prevents the majority of PCM from descending to the bottom of the enclosure. As a result, the convective motion in the lower section of the enclosure remains weak, restricting the expansion of the melting region. Hence, the melted region below the vortex in the lower section of the enclosure remains narrower compared to the recirculation zone created by the vortex.

The vortex-like behaviour, visible in the velocity fields, is most distinct for the 0-degree case. For the 8 and 18-degree inclination cases, the prominence of the vortex is reduced (see Figure 19 & Figure 20). As previously discussed, with increased tilt angle, the cooler parcels of PCM can descend over a wider region. This leads to the production of a weaker vortex with less concentrated flow directed towards the hot wall. Consequently, more of the PCM can descend into the lower region of the enclosure. This is likely responsible for the increase in the melting rate and larger transport of heat into the lower region of the PCM with an increase in the enclosure tilt angle as observed in Figure 18 through Figure 22.

As apparent in Figure 21 through Figure 22, at all enclosure tilt angles, there is a growing bulk region within the center of the enclosure which has negligible velocity. This is an indication that the heat from the hot wall is primarily transported through the liquid stream induced along the liquid domain boundary. The resultant velocity plots show that an increase in the tilt angle results in a wider region of the liquid stream along the liquid surface. This increased region of fluid flow reduces both the size of the stagnant liquid PCM region, and the overall area of hot stratified PCM liquid layers, thus contributing to the enhancement of the heat transport within the enclosure through the increase in natural convection.
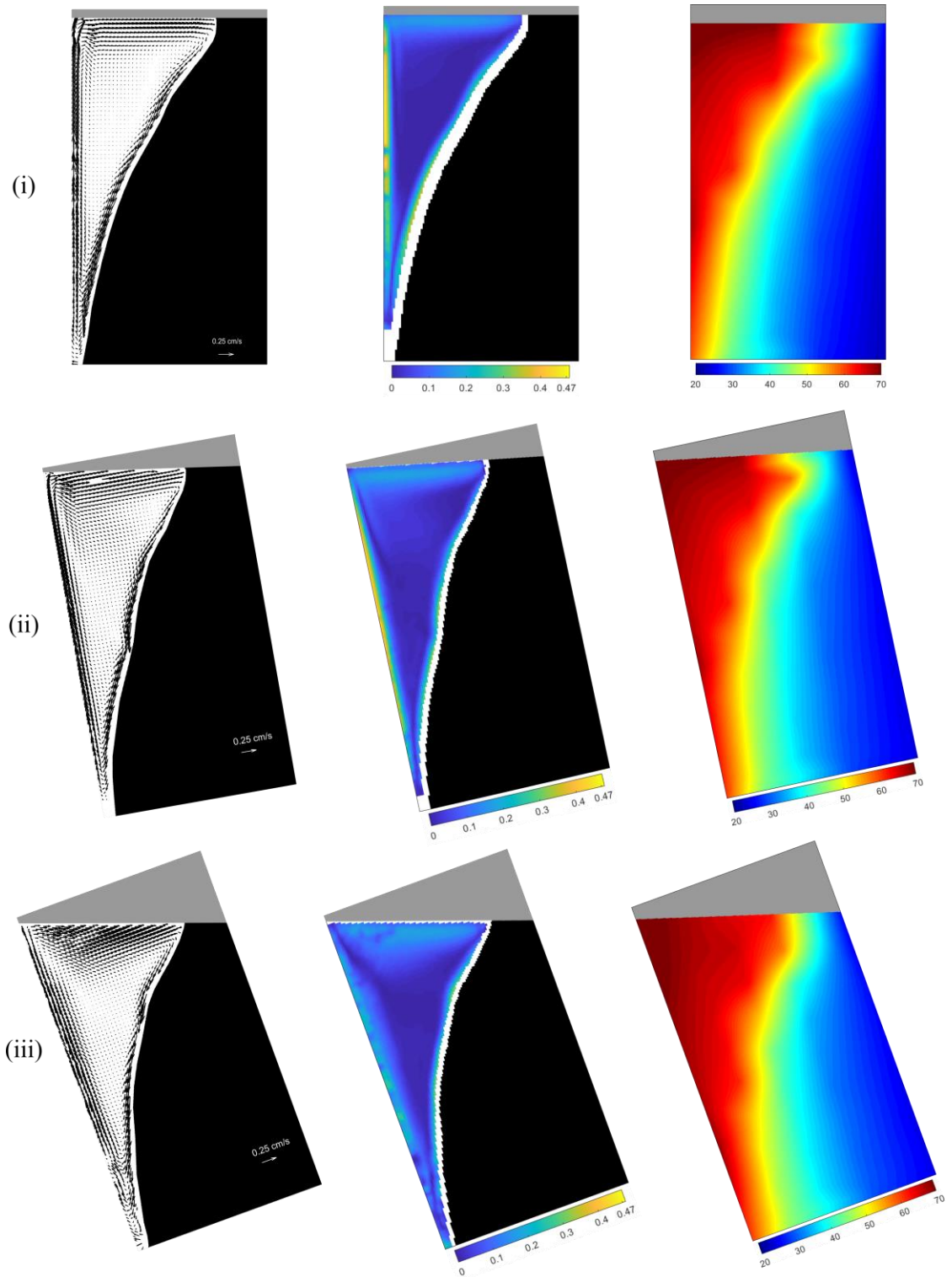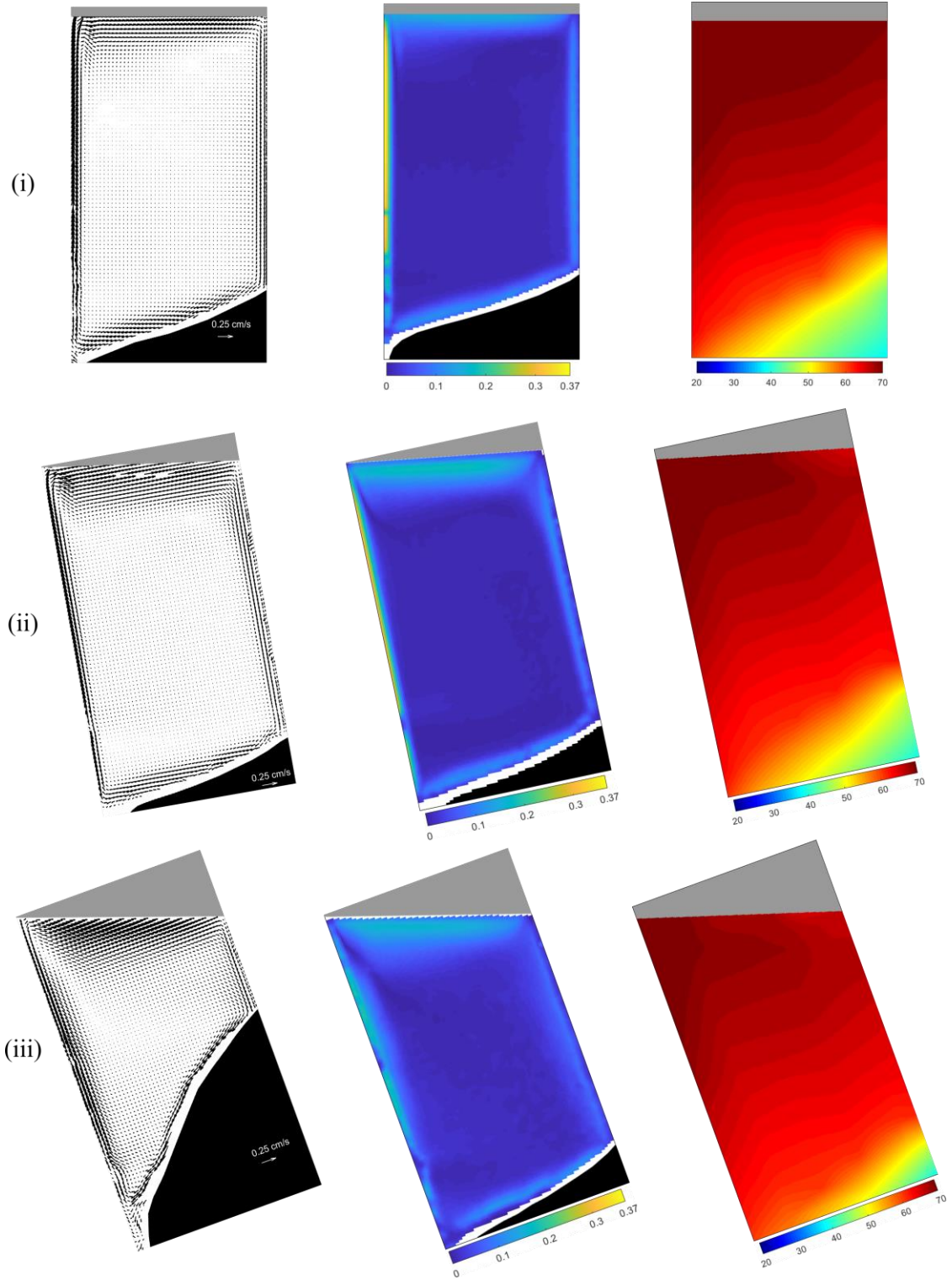
Figure 22: Velocity field, resultant velocity, and temperature field for (i) 0-degrees, (ii) 8-degrees and (iii) 18-degrees at time 600 minutes. Velocity plot units in [cm/s], temperature plot units in [°C].

As observed in the earlier figures, in all cases, the majority of the fluid flow occurs around the boundaries of the enclosure, which includes the heated wall, the liquid surface and the solid/liquid interface. Hence, it is important to investigate and quantify the velocities in these boundary regions for different enclosure tilt-angle cases and quantify the trends of the velocity magnitudes. Summarized in Table 2 are the average velocities in the boundary regions for each tilt angle, at 80, 240 and 600 minutes.

Table 2: Average velocity in boundary regions for all tilt angles, at 80, 240 and 600 minutes

Tilt Angle	Time [min]	Hot Wall Velocity (approx.) [mm/s]	Velocity Near Liquid Surface (approx.) [mm/s]	Velocity Along Solid/Liquid Interface (approx.) [mm/s]
0-Degrees	**80**	*4.6*	*1.6*	*2.5*
	240	*4.7*	*1.4*	*3.1*
	600	*3.8*	*1.1*	*1.2*
8-Degrees	**80**	*3.0*	*1.7*	*2.3*
	240	*3.8*	*1.5*	*2.7*
	600	*2.8*	*1.5*	*1.1*
18-Degrees	**80**	*2.6*	*1.9*	*2.1*
	240	*1.9*	*1.7*	*2.8*
	600	*1.8*	*1.6*	*1.0*

The results in Table 2 show that the velocity magnitudes for all tilt-angle cases, in general, are higher in the boundary region at the hot wall and lowest in the liquid surface region. The velocity magnitude in the solid-liquid interfacial region is between the two. This is

also qualitatively depicted in the previously discussed resultant velocity contour plots. The results show that in the regions of both the hot wall and the solid/liquid interface, fluid velocities for the 0-degree tilt angle have the largest magnitude at all times. This is a direct consequence of the alignment of both the buoyancy force and the orientation of the hot wall (vertical). Near the liquid surface however, the velocities are higher for the 8 and 18-degree tilt angle cases. It is likely that due to the impermeable liquid surface, buoyancy propelled fluid separating from the hot wall becomes concentrated in this region. Since the higher tilt angles experience greater fluid separation, more of this propelled fluid is concentrated along the surface than for the 0-degree tilt angle case.

It is also observed that the velocity along the solid/liquid interface increased from 80 to 240 minutes, and then significantly decreased from 240 to 600 minutes, likely a consequence of the increasing buoyancy force at earlier times, and the growing stagnant liquid region at later times. This is the primary region where heat transfer from the warmed liquid to the solid PCM occurs. With natural convection requiring both a heat source and heat sink, any reduction of velocity along the heat sink will reduce the overall heat transfer. As well, the velocities along all interfaces also decreased from 240 to 600 minutes for all tilt angles. Again, with fluid along these boundaries being the primary driver of heat transfer, any velocity reduction contributes to a reduction in natural convection within the enclosure.

While the 0-degree tilt angle experienced the highest velocities along the hot wall and solid/liquid interface, this accelerated fluid flow, referred to as a liquid stream, is restricted to a thin layer. For the 8 and 18-degree tilt angles, the accelerated velocity is distributed over a larger area, expanding the thickness of the liquid stream. Presented in Table 3 is the estimated thickness of the liquid stream at each of the three boundary locations.

Table 3: Estimated liquid stream thickness in boundary regions for all tilt angles, at 80, 240 and 600 minutes

Tilt Angle	Time [min]	Hot Wall Region Thickness (approx.) [mm]	Liquid Surface Region Thickness (approx.) [mm]	Solid/Liquid Interface Region Thickness (approx.) [mm]
0-Degrees	**80**	*5.2*	*7.9*	*4*
	240	*4*	*10.6*	*6.7*
	600	*5.1*	*13.3*	*6.9*
8-Degrees	**80**	*6.2*	*10.7*	*5.1*
	240	*6.7*	*11.2*	*5.3*
	600	*5.3*	*17.3*	*9.3*
18-Degrees	**80**	*9.3*	*15.9*	*5.3*
	240	*17.3*	*16.4*	*6.7*
	600	*12*	*19.9*	*10.6*

The thicknesses for all regions at 0-degree tilt angle are consistently less than the 8 and 18-degree tilt angles, as expected. Along the liquid surface and solid/liquid interface, the overall thickness of fluid flow increases with time for all cases. With the higher tilt angles, while the fluid velocity around the boundaries is lower, there is better distribution of the heated fluid, lessening the prominence of the stagnant liquid PCM region. It is interesting to note that for the hot wall region, the thickness for the 8 and 18-degree tilt angle cases experiences an increase from 80 to 240 minutes, and a decrease from 240 to 600 minutes. It is likely that with increasing time and the stratified liquid layers, there is a reduction in the temperature gradient potential that promotes flow to separate from the hot wall.

3.2   Solid-liquid Interface Tracking

The spatial and temporal movement of the solid-liquid interface is an indicator of the underlying physical processes that govern the transport of heat and hence the melting behaviour. Its detection is important for the characterization of the heat transfer during phase transition and is also an important validation parameter for numerical models. Conventionally, optical techniques are used to detect and track the solid-liquid interface [50], [55]. There are several issues and challenges with this approach however, as described below. Considering the necessary experiemenial setup, visual tracking of the PCM domain requires optical access which could be a challege or limitation in various setups. Additionally, the requirement of proper illumination tools and image capture and recording systems can be resource intense. In terms of material selection limitations, the PCM must have distinct color apprearences in the solid and liquid phases to allow the implementation of an image processing algorithm. As well, the imaging approach only allows interface detection adjacent to the transparent wall or in a near-2D configuration. Detecting the interface in a 3D domain is a practial limitation with the imaging approach. Hence, a more robust and easy to implement method would greatly help in the detection and characterization of the solid-liquid interface in a wide range of PCM domain configurations.

In the present study, a imaging PIV technique was used which facilitated the detection of the solid-liquid interface. In addition, high-resolution temperature measurements were also conducted for the characterization of the temperature field within the PCM domain. This provided an opportunity to investigate whether temperature data alone is sufficient enough to accurately detect the interface. For this purpose, the solid-liquid interface was detected and tracked in both space and time using the temperature data acquired during the phase change process for all three enclosure tilt angles.

The expected solid-liquid interface positions were tracked through the temperature field. While the true interface could be tracked through captured images, this was only possible at limited discrete times. The temperature data, on the other hand, was recorded at every second throughout the melting process and hence enables the tracking of the solid-liquid interface with higher temporal resolution for interface tracking. An in-house code in the

MATLAB environment was developed for this purpose. In each instantaneous temperature field, the MATLAB code located the grid points along the x-axis at which there was the smallest temperature difference between the actual PCM temperature and the melting temperature of 55 Celsius. These points were taken as the estimated location of the solid-liquid interface.

Figure 23 shows the interface that was detected from the temperature data, at different times and for all three tilt angles. For comparison, the corresponding interfaces detected from the PIV imaging data, are also plotted. The results show that overall, the solid-liquid interface, estimated from the high-resolution temperature data, agreed well both spatially and temporally with the interface positions obtained from the direct imaging. On average, the difference between the interface detected from the temperature field was within 15% of that obtained from the imaging data at all tilt angle cases. The results however also show some local disagreements between the detected interfaces, specifically near the top of the enclosure at higher tilt angles. This disagreement is likely due to the reason that with increased inclination, less temperature data was available within the top of the enclosure as fewer thermocouple resided within the PCM domain. Hence, the temperature data was slightly biased by the reduced resolution of the measured temperature (i.e. reduced thermocouple positions). However, as the interface started to shift both downwards and towards the adjacent wall, the number of recording thermocouples increased. This minimized any biasses from thermocouple positions in the temperaure field. The results in Figure 23 demonstrate that the temperature data could be used to accurately detect the solid-liquid interface both spatially and temporally. However, the accuracy of the detected interface is heavily dependent on the resolution of the actual measured temperature field. Hence, it is concluded that, with sufficiently high resolution of the measured temperature field, the solid-liquid interface can be accurately detected and tracked within the PCM domain.
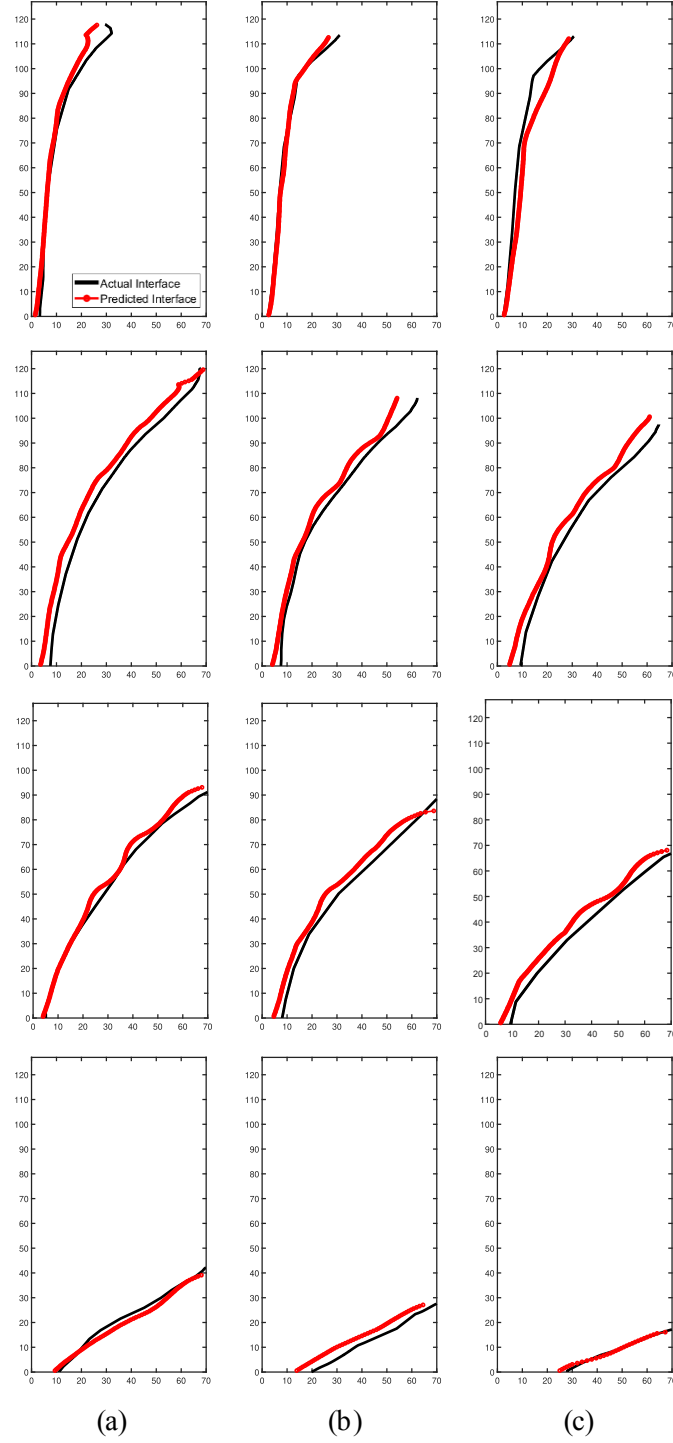
Figure 23: Predicted interface location for (a) 0-degrees, (b) 8-degrees, (c) 18-degrees at times 60, 160, 240 and 600 minutes in rows 1,2,3 and 4, respectively. All plots use the same legend shown in (a). The black line denotes the actual interface and the red line is the predicted interface

3.3   Time History of Melted Fraction

From the interface tracking, the solid and liquid fractions can be computed. As previously mentioned, the images of the melting progression were acquired at discrete times whereas the temperature data was acquired continuously throughout the melting process. Since results in the previous figure showed that the temperature data could accurately detect the solid-liquid interface, the interpolated temperature data was used to compute the instantaneous areas of solid and liquid regions within the PCM domain. Using a developed MATLAB script, the melted zone is identified as regions within the PCM domain that were above the PCM melting temperature of 55 Celsius. The melt fraction was then computed as the ratio between the area of the liquid region and the total PCM domain area, shown in equation (3.1):

$$\gamma_m = \frac{NT_l}{N_{total}} \tag{3.1}$$

Where γ_m is the melt fraction, NT_l is the number of interpolated grid coordinates above 55 Celsius, and N_{total} is the total number of grid points within the PCM domain. Although the melt fraction could also be determined through camera imaging, the temperature data allows for melt fractions to be updated as frequently as every 1 second.

Figure 24 shows the time history of melt fraction at each enclosure tilt angle. Both the melt fraction calculated from temperature data (solid lines) and raw camera imaging (dashed lines) is shown. There is good agreement between both methods. The discrepancy at later times is likely due to the discontinuous nature of the camera imagining, where there was a large amount of time between subsequent imagining. Analyzing the time history of melt fraction from the temperature data, the results show that initially the melting rate was linear at all tilt angles. This corresponds to the period where a shift from strong conduction to strong natural convection was present. As the time progressed, a reduction in the melting rate is observed at all tilt angles. It is likely that the heat from the hot wall was carried to the top of the chamber where it began to accumulate within the stagnant fluid region, and only a fraction of that heat was transported towards the solid PCM by the liquid stream flowing along the boundaries. As such, significant heat resided within the stagnant region

in the middle of the recirculation boundary. This stagnant region grew with time, and the amount of heat transfer from the liquid to solid PCM was reduced, thus slowing the melting rate.

Comparison between the three studied cases show that the melt rate increased with increasing enclosure tilt, supporting the idea that tilt angle has an influence on melt rate. The melting rates for the 0 and 8-degrees cases were relatively comparable in the early stages of melting. At later times however, the 8-degree tilt case began to melt at a higher linear rate than the 0-degree case. As the tilt angle was increased to 18 degrees, there was a further increase in melting rate. The increase occurred earlier on and remained almost constant during the duration of the melting process. On average, the melting rate for the 8 and 18-degree cases was 5.7% and 12.6% higher than that at the 0-degree case, respectively. It is also valuable to note that the results show the total melting time for 8 and 18-degree cases is 8.7% and 18.2% shorter, respectively, than that for the 0-degree case. The increase in the melting rate with an increase in the enclosure tilt angle supports the hypothesis mentioned earlier, that the increase in the inclination angle of the heat source cause the buoyancy driven flow parcels to advect upwards from the hot wall, enhancing mixing and hence increasing the melting rate.
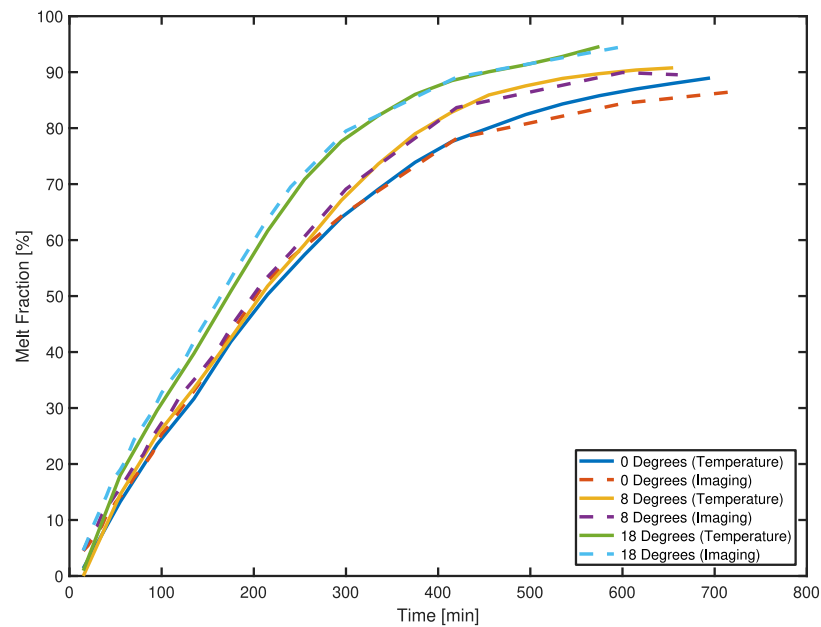
Figure 24: Time history of melted fraction

3.4   Temperature Contour Plots

Contour plots of the temperature data shown in Figure 25, highlight the growing, stratified region of warm PCM within the top of the enclosure. It should be noted that for 8 and 18-degrees, the plots are shown in the titled enclosure's frame of reference. The figure shows that at initial times, there was a sharp temperature gradient within the enclosure between the heated liquid PCM and the solid PCM. At this point, a significant portion of the solid PCM still remained near the initialized temperature of 20 Celsius. As melting progressed, and both the solid and liquid PCM warmed, the temperature gradient decreased, and an observed region of heated PCM began to expand, extending from the top left of the enclosure. Within this region, without the presence of a heat sink, the PCM temperature was nearly uniform. With time, this region expands from the hot wall towards the far, insulated wall. The minimal heat transfer from the insulated wall maintained the high and uniform temperature in the upper region, as well as, supported the stratified layers of heated liquid PCM. With time, the region of near-uniform temperature expanded downward. This in turn, contributed to the reduction of heat transfer from the hot wall to the solid PCM, slowing the melting rate. Additionally, in Figure 25, plots (b) and (c) show an inverse relationship between the enclosure tile angle and the area of hottest PCM. That is, at higher tilt angles, the region of the hot PCM is smaller. As mentioned earlier, this is likely due to the increase in flow circulation, and mixing, which increased the heat transfer from the top of the enclosure, towards the solid interface.
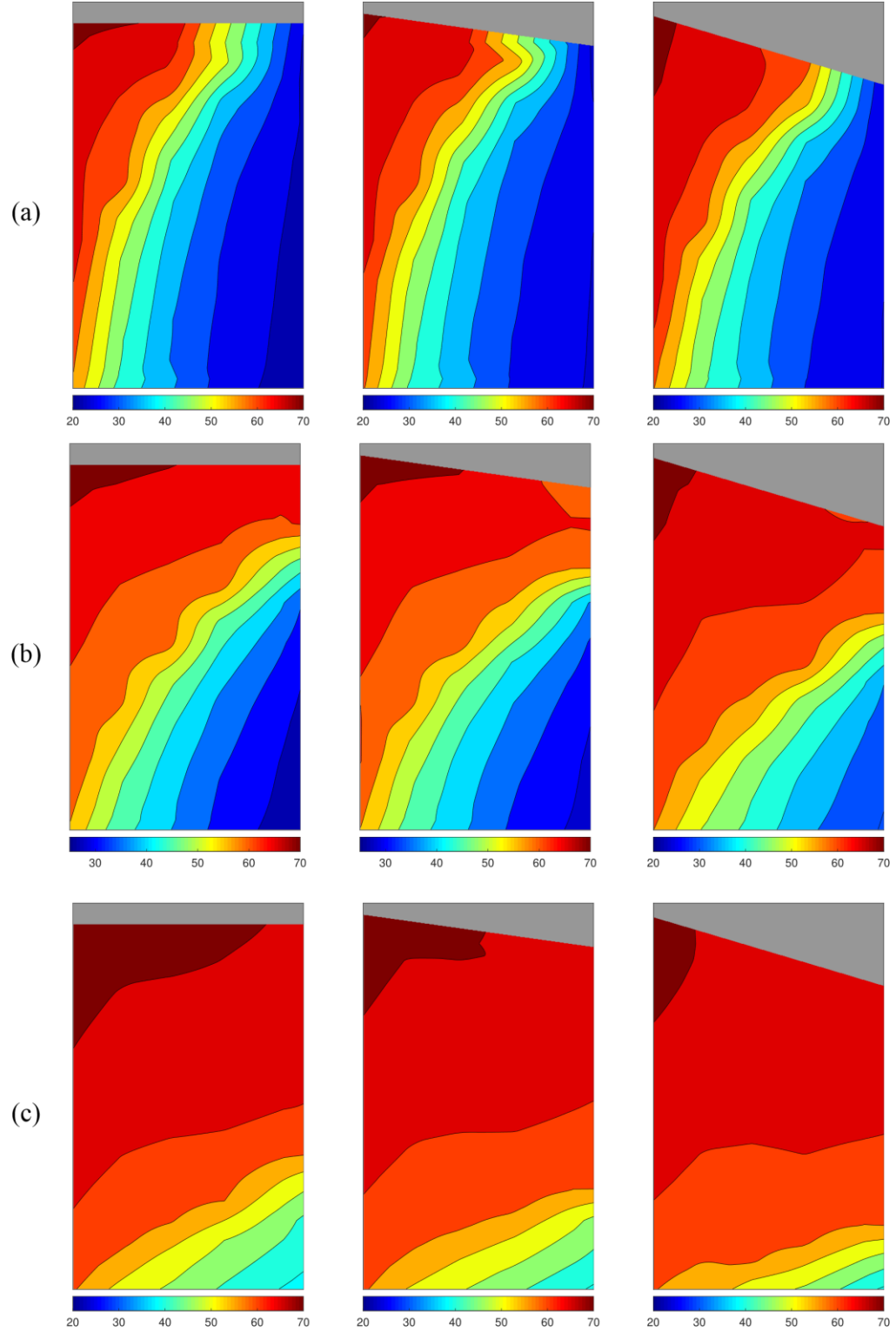
Figure 25: Contour temperature plots for (a) 120 minutes, (b) 240 minutes and (c) 600 minutes. The 0, 8 and 18-degree cases are shown in column 1, 2 and 3, respectively. Units in [°C].

3.5   Time History of Mean Temperature of Liquid PCM

The mean temperature of the liquid PCM ($T_{l_{mean}}$) at a given time, was calculated by averaging the temperature of the liquid region, defined as any temperature within the enclosure above the melting point of 55 Celsius. The time history of $T_{l_{mean}}$, calculated every 180 seconds, is plotted in Figure 26 for all three enclosure tilt angle cases. The results show that in all three cases, the liquid PCM experienced a sharp temperature rise at the very early stages of melting. At this point there exists only a very thin layer of liquid PCM, which formed directly adjacent to the hot wall when melting began. The heat transfer through this thin liquid layer was primarily due to conduction since the viscous effects were significantly stronger than buoyancy forces.

The sharp initial temperature increase occurs until a melt fraction of approximately 5%, for all tilt angle cases. Soon after, a reduction in the mean liquid temperature is observed, which coincided with the onset of natural convection. The buoyancy-driven convective currents enhanced the transportation of accumulated heat from the liquid region, thus lowering the mean liquid temperature. This reduction of the liquid PCM temperature occurred for a relatively short duration, from a melt fraction of approximately 5-10%.

As the recirculating liquid PCM stream became fully established (see, for example, the velocity fields in Figure 19 and Figure 20), it created an almost equilibrium between the heat transferred to the liquid stream from the hot wall and the heat transported by the stream to the solid region. This resulted in a nearly constant mean liquid temperature during the melt fraction interval of 10% to 30%.

After a 30% melt fraction, there is an observed increase in the mean liquid temperature that continued until the end of the melting process. The simultaneous analysis of the velocity and temperature data revealed that this temperature increase began when the solid-liquid interface reached the far insulated wall, denoted in Figure 26 by the vertical dashed line. Up until this point, the liquid stream was in full contact with the solid PCM region, continuously transferring heat along the full length of the enclosure (see Figure 20). However, once the interface reached the insulated side wall, minimal heat was transferred from the liquid stream to the insulated wall. As the interface further descended, the contact

area of solid PCM, and hence effective heat sink area, decreased, and the mean liquid PCM temperature rose. A rise in the liquid temperature reduced the temperature gradient between the liquid and the hot wall, resulting in the reduction of the overall heat transfer rate, slowing the melting process in the later stages as observed in Figure 24.
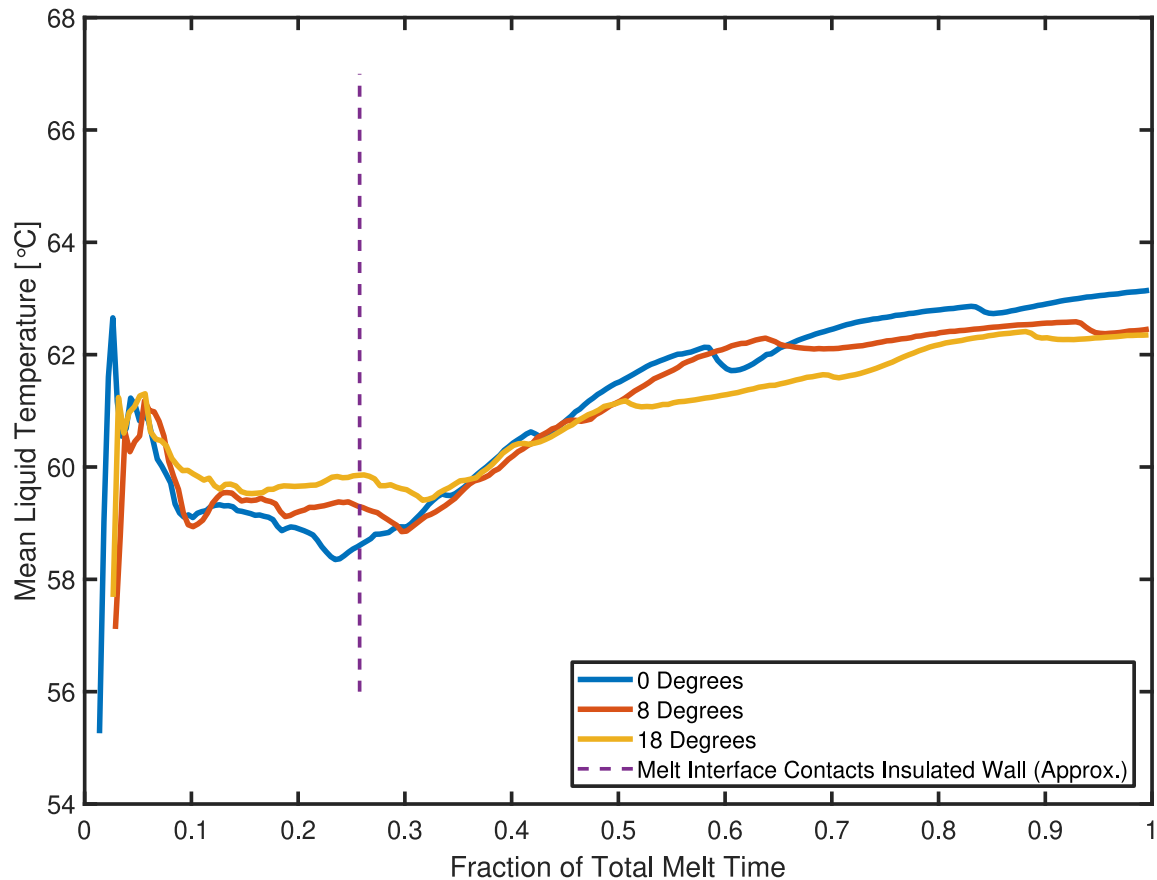
Figure 26: Time history of mean liquid temperature

3.6   Time History of Specific TC Temperature Readings

The time history of the PCM temperature obtained from thermocouples (TC) imbedded within the enclosure provides further understanding into the effects of enclosure inclination and the overall melting process. Figure 27 shows the temperature history for each angle, at four specific locations within the enclosure as highlighted in each plot. Each plot shows the recorded TC temperature every 100 seconds.

The time history of the temperatures at TC location R3-C2 show a sharp linear increase at initial times for all enclosure tilt angles. The TC in this location is at 14 mm away from the hot wall and 34 mm from the top of the enclosure. At this position, the temperature rose almost linearly and rapidly in the early stages of melting, which is likely due to the strong buoyancy-driven convective flow. As this location was in the top region where the hot PCM accumulated, the temperature marginally increased during the remaining melting process. The location R3-C2 also shows that the hot PCM accumulation in the top region close to the hot wall remains similar for all tilt angle cases.

The TC at location R4-C3 also shows the sharp temperature increase at initial times, for all enclosure angles. As this TC is further away from both the hot wall (29 mm) and the surface (52.5 mm), the temperature rise with time showed a quadratic trend rather than a linear trend, which was observed closer to the hot wall (see location R3-C2). Due to the distance of this location from the hot wall, the sharp temperature rise occurred over a longer period compared to the earlier location (105 minutes versus 75 minutes). As this region also became part of the warm stagnant liquid zone, the temperature rise became marginal during the rest of the melting process. Comparison among tilt angle cases show almost identical temperature values at 0 and 8-degree tilt angles and a relatively higher temperature at the 18-degree tilt case.

Investigating a location that is further away from the hot wall and the liquid surface (location R6-C4), both the rate of the initial temperature rise, and the maximum temperature was lower when compared to the locations closer to the hot wall and liquid surface. This slower temperature rise is associate with the gradual expansion of the liquid region. The lower maximum constant temperature in the latter part of the melting is due to its farther location from the top of the enclosure. Finally, at location R7-C5, the rate of temperature rise and the maximum temperature decreased further than previous locations; an expected consequence of the increased distance from both the hot wall and liquid surface (see location R7-C5).

Additionally, by the time that the boundary of the solid-liquid interface passes the TCs at R6-C4 and R7-C5, there has been prolonged sensible heating of the solid PCM. This results

in a smaller temperature gradient between phases and reduces the heat transfer within these locations. As well, at these times, the natural convection has begun to slow. Combined, the far distance to the hot wall, the reduced temperature gradient, and the diminished natural convection all contribute to the slower rate of temperature increase at these locations. The results in locations R6-C4 and R7-C5 also show that the influence of the enclosure tilt angle on the PCM temperature becomes more significant in the regions further away from the hot wall and liquid surface. It is observed that in those regions, the PCM temperature increases more rapidly and to a higher magnitude with an increase in the enclosure tilt angle.

The overall maximum temperature reached is directly proportional to the vertical height of the TC location. Due to the stratified layers within the liquid region, with the warmed liquid remaining at the top of the enclosure, the lower TCs record lower maximum temperatures. The TC at location R6-C4 reaches a maximum temperature of 65.8 Celsius, and the TC at location R7-C5 reaches a maximum temperature of 59.7, 62.2 and 63.7 Celsius for the 0, 8 and 18-degree cases, respectively.

Comparing between all four TC locations, as the distance from the hot wall and the liquid surface increased (i.e. moved further into the enclosure), there was an increasing variation in the rate of temperature gain between each tilt angle case. That is, with the higher tilt angle for the 8 and 18-degree cases, at lower TC positions, there was a greater initial temperature rise when compared to the 0-degree tilt angle. This is likely due to the following: 1) All three cases experience comparable conductive heating at initial times. If the initial rate of temperature increase is primarily due to conduction, then increasing the enclosure angle would have a minimal effect for TCs closest to the hot wall. 2) Since much of the heat transfer from the liquid to solid phase occurs at a thin layer immediately adjacent to the boundary interface, its position has a significant effect on the temperatures recorded by the TC's within close proximity. For the higher tilt angle cases, with the reduction in the vortex like behaviour, and increased melt fraction, the position of the interface remains consistency closer to the lower TC's. In turn, this contributes to both the earlier and higher rate of temperature increase that was observed for the higher tilt angle cases.
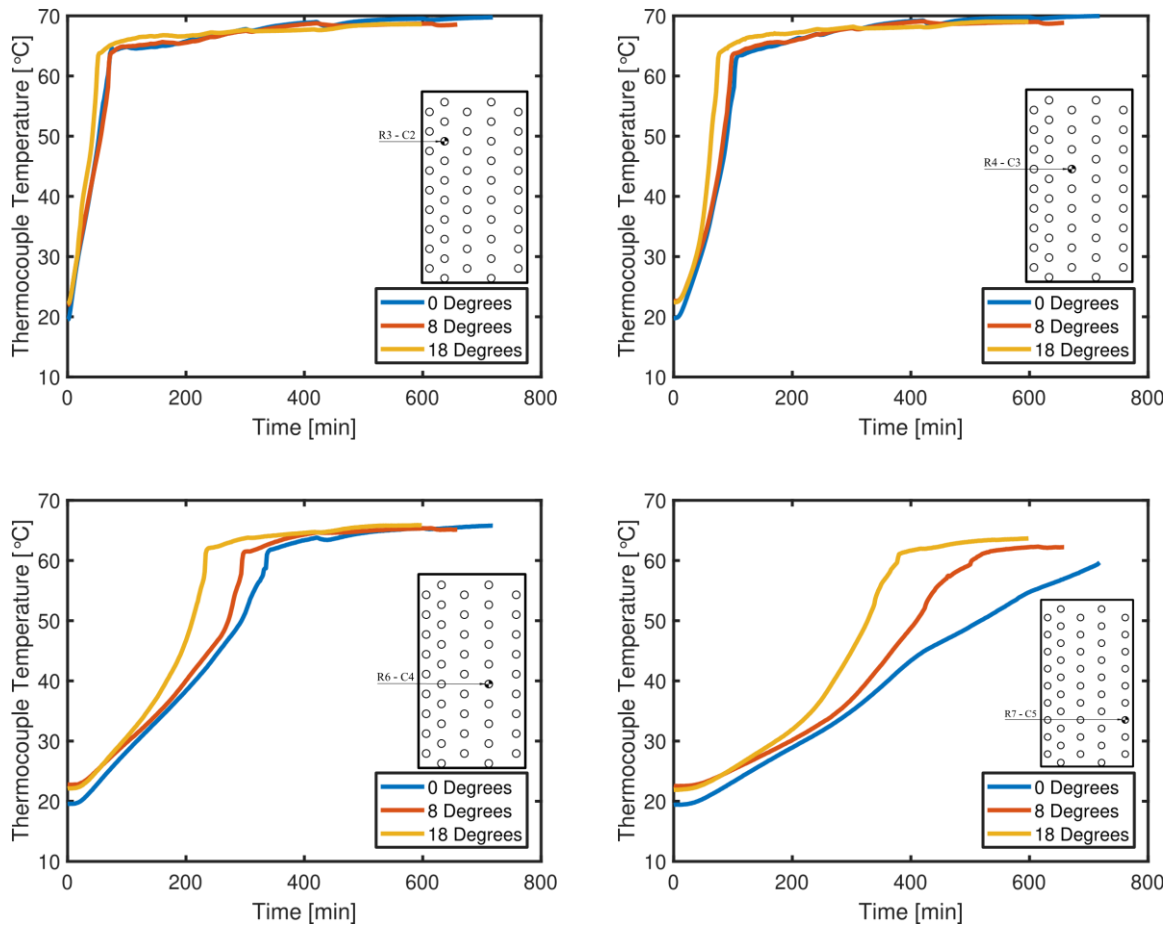
Figure 27: Temperature history at four indicated thermocouple locations

3.7   Cumulative Sensible and Latent Heat Absorbed Energy

The paraffin wax absorbed energy through both sensible and latent heating. There were two primary modes of sensible heating; sensible heat transfer to the solid PCM from initial temperature to the melting point and superheating of the liquid PCM (after melting). The absorbed latent heat can be estimated using the fraction of liquid PCM present. The instantaneous sensible heat transfer at a given time (t) was calculated by using equation (3.2) proposed by Shokouhmand and Kamkari [49]:

$$Q_{sensible} = \rho_s c_{p_s}(T_{m-s} - T_i)V_l(t) + \rho_l c_{p_l}\big(T_{m-liq}(t) - T_l\big)V_l(t) \qquad (3.2)$$
$$+ \rho_s c_{p_s}(T_{m-s}(t) - T_i)V_s(t)$$

Where the liquid, V_l and V_s are the volumes of liquid and solid fractions, respectively, at time, t. T_i represents the initial PCM temperature and T_l is the melting temperature of the PCM. T_{m-liq} and T_{m-s} represent the mean temperatures in the liquid and solid domains, respectively, at time, t. They were calculated by averaging the temperature field above and below the melting temperature, $T_{melting}$, of the PCM:

$$T_{m-liq}(t) = \frac{1}{NT_l} \sum_{k=1}^{N_{total}} T_k > T_{melting} \qquad (3.3)$$

and

$$T_{m-s}(t) = \frac{1}{NT_s} \sum_{k=1}^{N_{total}} T_k < T_{melting} \qquad (3.4)$$

Where, NT_l is the total number of data points above the melting temperature, NT_s is the total number of data points below the melting temperature, and N_{total} is the total number of temperature data point in the PCM domain.

In equation (3.2), the first term represents the sensible heating of the solid PCM to the start of melting. This term is necessary to account for the sensible heating that was required to reach the melting temperature for the fraction of solid PCM that melted. The second term

accounts for the superheating of the PCM past its melting point and the third term represents the sensible heating of the non-melted solid PCM from the initialized temperature to the onset of melting [49]. The instantaneous latent heat transfer at a given time (t) was calculated by using equation (3.5) :

$$Q_{latent} = \rho_l h_L V_l(t) \qquad (3.5)$$

The cumulative absorbed energy (addition of both sensible and latent heat totals, Q_{total}) in the PCM is plotted versus time in Figure 28. As expected, the cumulative energy increased with time. The results show a more rapid accumulation of energy during the first half of melting. It is found that approximately 85% of the total energy is absorbed in the first half time of the total melting process. Comparison of the results at different enclosure tilt angles show that total cumulative absorbed energy is the same for all cases, which is expected due to the energy conservation. The values varied by about 1%, which is due to the volume differences between the cases.
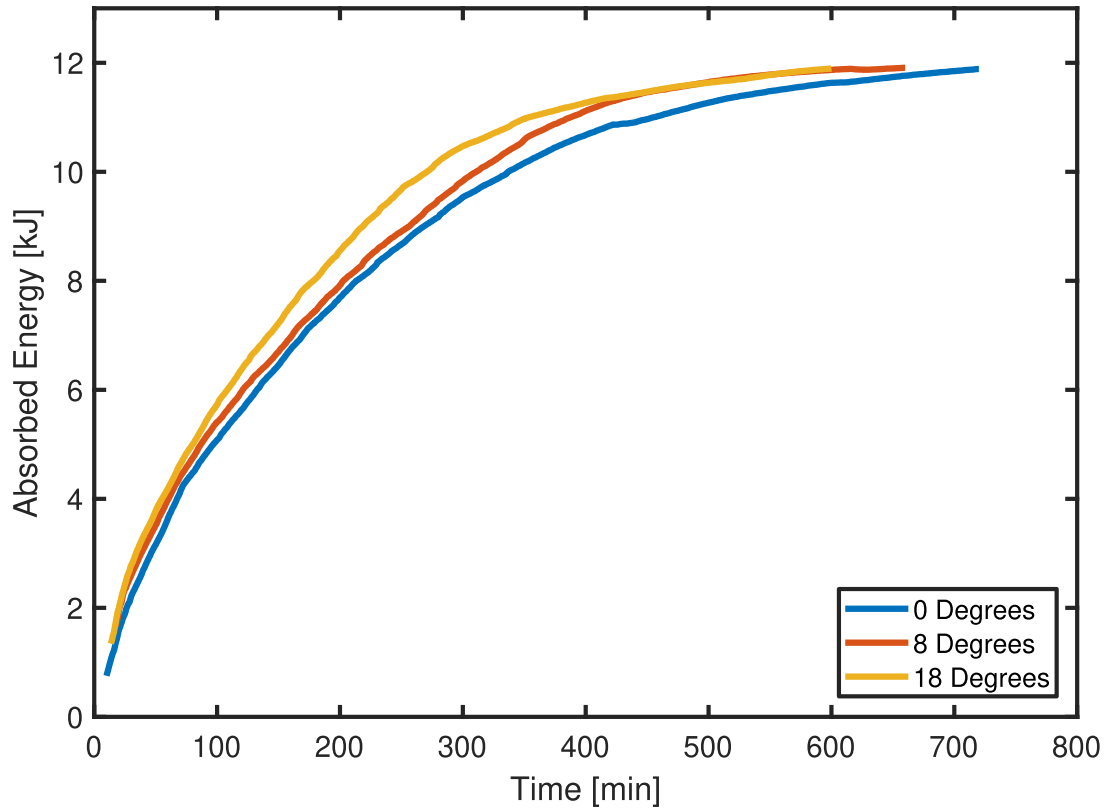
Figure 28: Total absorbed energy versus time

3.8   Transient Nusselt Number Analysis

The instantaneous surface-averaged Nusselt number was calculated for each enclosure tilt angle case, using the following equation:

$$\overline{Nu}(t) = \frac{\overline{h}(t)L}{k_l} \tag{3.6}$$

Where, L is the characteristic length used as the length of the hot wall, k_l is the thermal conductivity of the liquid PCM and $\overline{h}$ is the surface averaged heat transfer coefficient. The surface-average heat transfer coefficient is expressed as:

$$\overline{h}(t) = \frac{Q_{total}(t)}{A_w(T_s - T_{int})} \tag{3.7}$$

Where, A_w is the surface area of the hot wall, T_s is the average hot wall surface temperature and T_{int} is the average temperature of the solid-liquid interface. This temperature difference defines the temperature potential for the convective heat transfer. The average hot wall temperature was computed as the average temperature recorded by thermocouples attached directly to the aluminum surface. Note that once the interface reached the insulated wall on the other side of the enclosure, the T_{int} is computed as the weighted average of the insulated wall exposed to the liquid PCM and the remaining solid-liquid interface. The values are calculated over one-minute time intervals.

The transient Nusselt numbers for all enclosure tilt angle cases are presented in Figure 29. As the figure shows, the Nusselt number rapidly increased to peak values shortly after the beginning of the melting process, for all tilt angle cases. This maximum is likely due to the onset of the strong buoyancy-driven convective motion within the thin layer of melted PCM immediately adjacent to the wall, where a large temperature gradient existed between the hot wall and the cooler, solid PCM. The results show that this rapid increase in the Nusselt number is strongly dependent on the enclosure tilt angle, where increasing tilt angle results in greater Nusselt number rise. From this maximum, for all tilt angle cases, the Nusselt number then started to decrease relatively quickly. This is likely due to a combination of both the weakening temperature gradient and increased distance between

the hot wall and solid PCM. In all tilt-angle cases, this decrease in Nusselt number continues until a melt fraction of approximately 30%, where they reach a local minimum. From this local minimum, to a melt fraction of approximately 70%, the Nusselt number behavior is strongly influenced by the enclosure tilt angle. As observed, for the 0-degree tilt angle case, the Nusselt number shows a relatively linear decreasing trend. However, as the enclosure tilt angle increased to 8-degree, the Nusselt number remained almost constant and with the highest tilt angle at 18-degrees, a slight increase was observed. Thus, within this period, an increase in tilt angle corresponded to a greater average Nusselt number.

Further in the melting, as the time progressed, a decreasing trend of the Nusselt number is observed for all tilt angle cases. Comparison of Nusselt number for all cases show that overall, the Nusselt number increased monotonically with an increase in the enclosure tilt angle.

As observed from the velocity vector fields and resultant velocity plots, the higher inclination angles promoted an increase in the recirculation region around the perimeter of the enclosure, enhancing the natural convection which is directly related to the Nusselt number (see Table 2 & Table 3). Although the 0-degree tilt angle had greater velocity along the hot wall and solid/liquid interface in the liquid stream, the higher tilt angles had greater spatial extent of the liquid stream. This contributes to an increase in natural convection as the circulation of the warmed PCM is over a larger area. In turn, heat transfer away from the hot wall is greater, and the region of stagnant PCM is reduced. Additionally, the 8 and 18-degree tilt angle cases had faster velocity near the liquid surface, an important region for heat transfer. The heated liquid PCM along the hot wall is predominantly transferred to the solid PCM in the region along the liquid surface. By having a higher liquid velocity, distributed over a larger region (as seen in Table 2 & Table 3) more of the warmed fluid can be transported to the heat sink of solid PCM. For all cases, it is observed that the velocity along the solid/liquid interface decreases with time. The solid-liquid interface defines the boundary of the heat sink (i.e. the solid domain). A reduction in velocity along this interface results in a reduction in natural convection, causing the Nusselt number to decrease.
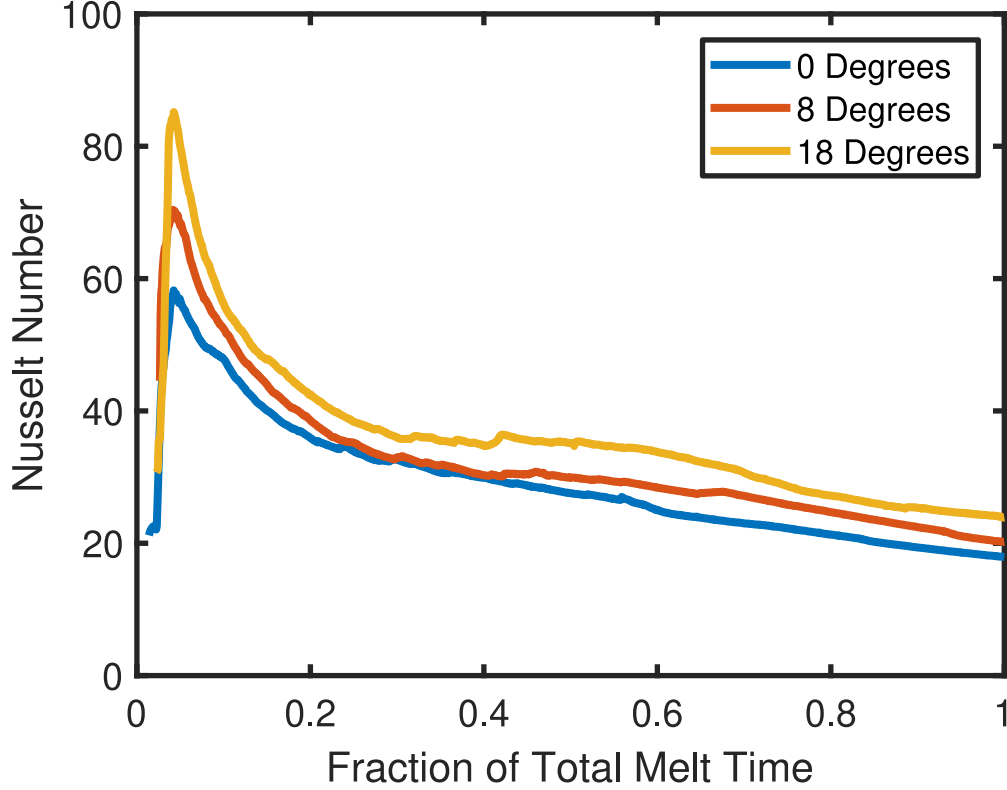
Figure 29: Nusselt number as a function of total melt time

3.9 Transient Rayleigh Number Analysis

The Rayleigh number (Ra) is a non-dimensional parameter that is used to characterize the contribution of buoyancy force relative to the viscous dissipative force in the fluid domain. The Rayleigh number is expressed as [50]:

$$Ra = \frac{g\beta(T_s - T_b)L^3}{\nu\alpha} \tag{3.8}$$

Where g is gravitational acceleration, β is the coefficient of thermal expansion of the fluid, T_s is the surface temperature, ν is the kinematic viscosity and α is the thermal diffusivity of the fluid. In the present case, T_s is computed as the mean surface temperature of the aluminum heater. The properties of the PCM due to temperature change are considered negligible within each respective solid and liquid phase, and as such remained constant through all calculations of the Rayleigh number. The variables T_b and L refer to the bulk temperature of the fluid (liquid PCM) and characteristic length, respectively. In the

classical cases of natural convection in a bounded single-phase fluid heated through a vertical wall, the length of the plate or the distance between the hot and cold walls of the enclosure is used as the characteristic length, and the temperature difference between the hot and cold walls is used as the driving temperature potential i.e., the cold wall temperature is used as T_b [97]. However, the present case involves natural convection heat transfer in an enclosure, which contains two simultaneous phases of solid and liquid material, where the extent of the liquid domain is continuously changing. Hence, the variables T_b and L may need to be defined differently. To investigate this issue, when calculating the Rayleigh number, the bulk liquid temperature was computed three different ways and the characteristic length was defined two different ways. The three different methods to define the bulk temperature are: 1) the melting temperature of the liquid PCM, T_l (a constant value of 55 Celsius), 2) the mean temperature of the liquid domain, T_{m-liq} (a time dependent value, calculated from Eq. (3.3), and 3) the mean temperature of the solid-liquid interface, T_{int} (a time dependent value, equivalent to T_{int} from Eq (3.7). The characteristic length was defined two ways, as 1) the distance between the hot wall and the horizontal mid-point of the solid/liquid interface, L_{int}, and 2) the distance between the hot wall and far insulated wall, L_{wall}, (a constant value of 70 mm). The transient Rayleigh number calculated using different variations of the bulk liquid temperature and characteristic length are presented in Figure 30. Figure 30 (i), (ii) and (iii) show the Rayleigh number calculated with L_{int} and T_l, T_m and T_{int}, respectively, while Figure 30 (iv), (v) and (vi) show the Rayleigh number calculated with L_{wall} and T_l, T_m and T_{int}, respectively. The results show large variations in each Rayleigh number calculation indicating that both the bulk liquid temperature and the characteristic length significantly influence the observed trends and magnitudes.

The effects of a variable characteristic length, L_{int} on the Rayleigh number variation is investigated first (see Figure 30 (i-iii)). The results show a similar trend for all variations of the Rayleigh number calculation. That is, both L_{int} and the Rayleigh number increase in a similar way. Since the Rayleigh number is proportional to the cube of the characteristic length, any increase in L_{int} would significantly contribute to an increase in Rayleigh number values. In the three cases using L_{int}, there exists an inflection point at approximately 50% of the total melting time. The Rayleigh number increased more rapidly

before this point and relatively slower after it. This point was found to be correspondent to a change in the melt rate as observed in Figure 24, i.e. before this point, the melting rate was the greatest and L_{int} increased most rapidly and in the second half of melting, when the melting rate decreased, the rate of increase of L_{int} also slowed down (see Figure 24). Comparison among different tilt angle cases show that before this inflection point, the Rayleigh number was relatively similar for all tilt angle cases implying that the tilt angle of the heat source has no influence on the Rayleigh number in the first half of melting. The influence of the tilt angle is evident after the inflection point where the results show a significant decrease in the magnitude and the rate of Rayleigh number with an increase in the tilt angle. This implies that in the latter half of melting, the Rayleigh number and hence the buoyancy effects decreased with an increase in the tilt angle of the heat source. The similar trends observed in all three plots (Figure 30(i-iii)) indicates that the trends are primarily influenced by the variation in L_{int}. That is, in the second half, the mid-half location of the interfaced moved slowest at the highest tilt angle.

While the trends in Figure 30(i-iii) are influenced by the characteristic length, the variations in the magnitude of Rayleigh number are due to the differences in the bulk temperature considered in these plots. The results show that on average, the Rayleigh number using T_l is approximately 50% and 26% larger than that using T_m and T_{int}, respectively. The reasons for these variations in Rayleigh number can be explained as follows: The bulk liquid temperature used in Figure 30(i) is the melting temperature, T_l, which is a constant. Hence, any increase in the Rayleigh number in Figure 30(i) attributed to the increase in the characteristic length. In Figure 30(ii), the bulk liquid temperature used is the mean liquid temperature, which varied throughout the melting process (see Figure 26). The temperature data of the hot wall surface temperature (not shown here) indicates that upon reaching steady state there were only minor fluctuations in the surface temperature. As well, the warm fluid immediately adjacent to the hot wall contributed to the overall liquid temperature, and therefore the mean temperature increased well past the melting temperature of the solid PCM. Hence, as the mean liquid temperature increased with time, the overall difference between the hot wall surface and the mean liquid temperature decreased, resulting in the lowest Rayleigh number magnitudes among the three cases. The interface temperature, which was considered in Figure 30(iii), was not influenced by the

heated fluid along the hot wall. As such, the overall magnitude of Rayleigh number was greater than in Figure 30(ii).
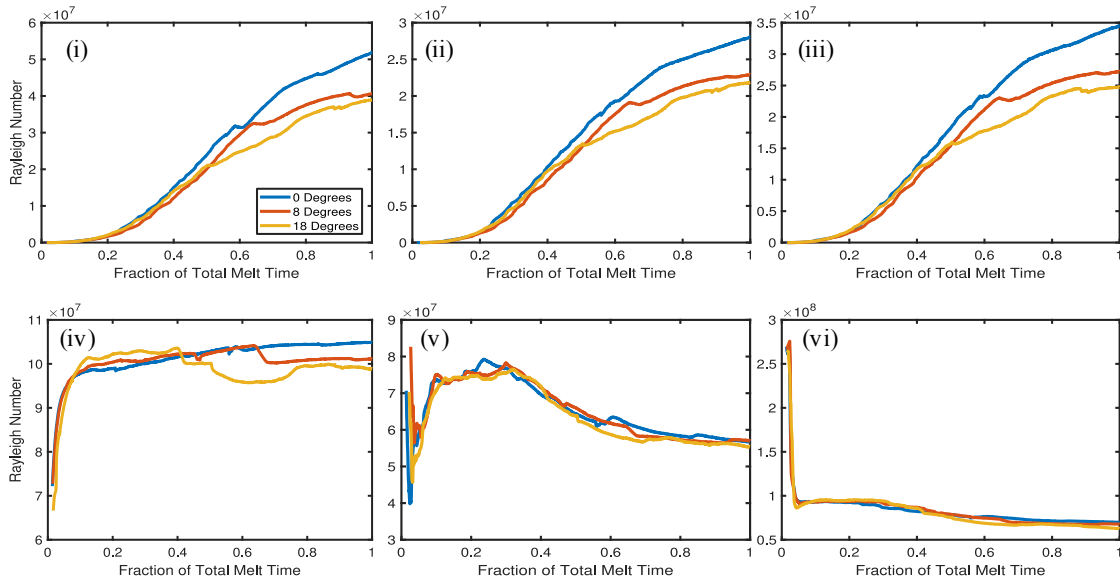
Figure 30: Rayleigh number plotted against fraction of total melt time with varying bulk temperature and characteristic length calculations. All y-axes refer to the Rayleigh number and each plot uses the legend in (i)

The plots in Figure 30(iv-vi) considered a constant characteristic length L_{wall}. In Figure 30(iv), all variables are constant except for the mean surface temperature of the heater. As mentioned earlier, there were fluctuations in the hot wall temperature. While these fluctuations were minor (less than $\pm$ 1 Celsius), they appear magnified when used to calculate the Rayleigh number. Since this method of calculation is dependent solely on the hot surface temperature, variations in that temperature are over represented and therefore improperly capture the heating trends present.

Figure 30(v) and Figure 30(vi) show the Rayleigh number calculated with a constant characteristic length, and varying bulk liquid temperatures with (v) using the mean liquid temperature and (vi) using the mean interface temperature. In both cases, the sharp temperature gradient driving natural convection contributes to the high Rayleigh number magnitudes initially observed. These Rayleigh number values drop rapidly to a local minimum as the recirculation region develops, lowering the overall liquid and interface

temperature. After the local minimum, the Rayleigh number increase slightly and then remains relatively constant. This is likely due to the constant mean liquid temperature, as previously shown in Figure 26. Finally, the Rayleigh number for both cases begins to decrease as the temperature difference between the heat source and sink decrease.

When comparing between all six cases, several conclusions can be reached. Case (i), (ii) and (iii) are beneficial when investigating the effect of cold interface position within an enclosure. However, it is likely that the interface position dominated, and limited the investigation of any temperature gradient effects. These three cases show that the Rayleigh number continuously increased which is not consistent with what was observed through the velocity plots. Case (iv) is highly dependent on the hot surface temperature and does not accurately consider all components contributing to the buoyancy driven flow. Case (v) and case (vi) are useful to study the effect of temperature gradients within an enclosure, while keeping the characteristic length constant. Examining the Rayleigh number, it appears case (v) and (vi) most accurately represent the underlying physical properties present, comparing well with the conduction dominant, convection dominant and weakening convection regions. Additionally, these cases have good agreement with the observed velocity data, as interface velocities are a good indication of buoyancy forces present. By utilizing the velocity data in parallel with the temperature data, better insight into the true underlying physical properties can be gained. As previously discussed, on average from 80 to 240 minutes (approximately 12% to 36% of total melt) the interface velocities for all cases increased. This agrees well with the observed Rayleigh number increase in Figure 30(v) and 11(vi) over a similar time range. Similarly, from melt fractions of 36 to 100%, the interface velocities for all tilt angles decreased, a trend also seen in the Rayleigh number over this time.

3.10   Conclusions

Through the generated velocity vector plots and temperature contour plots, it was shown that there are three primary heat transfer phases. The initial phase, where conduction was dominant, occurred when the melt front was near parallel to the hot wall. At this point, the temperature gradients existed primarily in the horizontal direction. The second phase is when natural convection began and created a distinct recirculation zone around the boundaries of the liquid region. Comparing between each tilt angle case, it was shown that with increasing tilt angle this recirculation region was enhanced. This was evident through the increased thickness of the liquid stream for the 8 and 18-degree tilt angles. The third phase occurred when the natural convection began to decrease due to a reduction in the magnitude of the liquid recirculation. This reduction was caused by growing area of stagnant PCM that remained within the top of the enclosure. Also observed through the velocity plots was a CCW flowing vortex that occurred in lower section of the recirculation zone, between the solid PCM and the adjacent hot wall. This vortex grew in size as the melt fraction increased and was responsible for an increase in the local melt rate. Additionally, it was observed that with increased tilt angle, the prominence of this vortex was reduced.

By tracking individual TC temperature readings and determining the regions above the melting temperature of the PCM, the mean liquid temperature could be calculated with time. Additionally, through a similar process, the solid-liquid interface could also be predicted with time by utilizing the TC readings. Strong agreement was shown between the temperature-based interface tracking and the raw camera images tracking, supporting the use of temperature measurements for robust interface tracking.

The Nusselt and Rayleigh numbers were also calculated. They further highlight the three primary heat transfer phases shown qualitatively in the PIV and temperature data. A significant relationship between enclosure tilt angle and Nusselt number was observed at initial melting times. The Rayleigh number was calculated through six methods to underline the effect of bulk temperature and characteristic length variation. All results in this chapter highlight the significance of flow and temperature characterization in the liquid PCM domain.

Chapter 4

4 Conclusions and Recommendations

4.1 General Conclusions

Thermal energy storage is an important component in the rapidly expanding fields of energy conservation and sustainability. The ability to store large quantities of thermal energy at relatively constant temperature is advantageous in many temperature sensitive applications. As well, TES is beneficial to provide consistency through the decoupling of energy supply and demand, critical for the widespread adoption of renewable energy resources such as solar and wind energy which are inherently inconsistent due to their reliance on uncontrollable environmental factors. Furthermore, latent heat TES is promising for the recovery and reuse of waste heat by enabling direct energy transfer from these heat sources and the wide availability of PCM melting temperatures. This energy conservation is especially important to conserve the finite supply of fossil fuels which continue to be major components in todays energy supply. However, due to the occurrence of phase change in a latent heat TES system, where the two phases simultaneously existing in an inherently inverse volumetric variation, the heat transfer processes are complex and transient in nature. As such, further investigation and research into the characterization of the thermo-fluid behavior can help to advance the technology, and overcome the weaknesses found in PCM-based thermal storage systems.

This research work is focused on the experimental investigation of the transient flow and transient thermal behavior of phase change material during solid-liquid phase change (melting). Two specific aspects of the current work are to investigate the influence of the flow behavior within liquid PCM on the melting and heat transfer processes, as well as, the impact of heat source orientation on the underlying melting and heat transfer processes. To date, a full investigation into the liquid flow behavior during PCM melting has not been unequivocally demonstrated in the scientific literature. Furthermore, to the authors' knowledge, an investigation utilizing the combination of both high-resolution velocity and temperature data has not been conducted. This combination was used to provide further

insight into the melting behaviour and trends that exist during PCM melting with varying heat source orientation.

To facilitate the research, an insulated rectangular enclosure was constructed, filled with paraffin wax (used as the PCM), and was isothermally heated along one vertical wall. The entire enclosure was rotated CCW through three varying angles, providing a heated wall at tilt angles of 0 degrees (vertical), 8 degrees and 18 degrees. PIV was utilized to measure two-dimensional velocity fields of the liquid domain along the mid-vertical plane inside the enclosure. Due to the transient nature of melting, with varying liquid and solid fractions, the PIV data was acquired at discrete times during the study, from fully solid to fully melted PCM.

In a separate study, utilizing the same experimental setup and conditions, 53 thermocouples were inserted through the back face of the enclosure and were aligned along the same mid-vertical plane used in the PIV measurements. The thermocouples simultaneously sampled the data from the onset of heating until the PCM had fully melted. The recorded thermocouple data was interpolated to provide temperature data spanning the entire domain of the PCM enclosure. The temperature data allowed heat transfer characteristics to be calculated, specifically the Rayleigh and Nusselt numbers. Furthermore, it was demonstrated that high resolution temperature data could successfully predict the melt interface, eliminating the need for optical access to determine solid/liquid interface positions.

The results show three primary heat transfer phases. In the initial phase, conduction was the dominant mode of heat transfer when the melt front was near parallel to the hot wall. At this point, temperature gradients existed primarily in the horizontal direction. The second phase occurred when natural convection began, with the results showing for all tilt angle cases, a distinct recirculation zone developing within the liquid region. As the temperature in the liquid domain increased, the buoyancy forces surpassed the viscous forces, initiating buoyancy driven flow. Comparison between the vertical (0-degrees tilt angle) and inclined (8, 18-degrees tilt angle) heat source cases, shows that the recirculation region around the boundaries of the liquid domain was enhanced with the increased tilt of

the heat source. That is, while the 0-degree tilt angle generally experienced higher velocities along the interfaces, the thickness of the liquid stream is greater at 8 and 18-degree tilt angles. As such, the prominence of a stagnant region of liquid PCM is lessened for the higher tilt angle cases. The third phase occurred when the natural convection began to decrease due to a reduction in the liquid recirculation, a consequence of a growing region of heated PCM which resided in the top of the enclosure. Both the stratified temperature layers and negligible flow velocities contributed to the overall decrease in the natural convection occurring within the liquid PCM domain, and in turn was a major factor in the decreased melt rate observed at later times of melting.

A dominant, CCW flowing vortex was observed in the lower section of the recirculation zone, between the solid PCM and the adjacent hot wall. With increasing melt fraction, this vortex grew in size and was responsible for a decrease in the melt fraction of PCM beneath it. Fluid descending along the solid/liquid interface in its vicinity was redirected into the rising plume adjacent to the hot wall, preventing the majority of the flow to descend the full height of the enclosure. With increased enclosure angle, the prominence of this vortex was reduced, and hence the effects of melt reduction were diminished

The calculated Nusselt and Rayleigh numbers further highlight the underlying physical behaviors that occurred during the melt. The Nusselt number emphasised the three primary heat transfer phases, qualitatively shown in the PIV and temperature field data. A strong dependence on enclosure tilt angle and Nusselt number increase in the first region was observed. The Rayleigh number was calculated by six different methods, underlining the effect of varying the bulk temperature and characteristic lengths on the overall magnitudes and trends on the Rayleigh number. For proper comparison between cases, it was determined that the characteristic length should remain constant, allowing temperature variations to be the primary influence on the overall Rayleigh number value to provide proper evaluation between tilt angle cases.

The results in this study highlight the significance of the flow and temperature characterization in the liquid PCM domain. It was found that the fluid velocity is critical for both the heat transport within the liquid domain and the overall melting rate and its

pattern. Consequently, because the fluid velocity behavior influences natural convection, which is the primary mode of heat transfer, understanding its behavior is crucial in the advancement of thermal energy storage system design.

4.2 Contributions

Until now, an investigation utilizing the combination of both high-resolution velocity and temperature data had not been conducted of melting PCM. As such, these results further extend the understanding of phase change and the associated heat transfer processes in the PCM. The significance of natural convection within the liquid PCM domain was evidentially demonstrated through the combination of both velocity and temperature measurements. Differences between increasing heat source tilt angle was shown to have a significant impact on the fluid velocity around the perimeter of the liquid domain, with increasing tilt angle showing enhanced natural convection through the increased spatial distribution of the liquid stream.

Additionally, comprehensive benchmark data for the improvement of numerical models simulating the solid-liquid phase change process has been provided. Simulations can now be validated through both temperature and velocity measurements which was not possible beforehand.

4.3 Future Recommendations

Although a detailed study of PCM phase change was conducted, there are several aspects that need to be considered for the advancement of the scientific knowledge related to the phase change and transient heat transfer in a thermal storage medium. Some recommendations for future studies are:

1) Expand Investigations to the Freezing Cycle

In real-world applications, latent heat TES systems operate in both melting and freezing cycles. The current study focused solely on the melting processes and associated heat transfer characteristics. Further investigation into the freezing cycle is a natural extension

of this work to encompass the entire process. Challenges surrounding the optical access for PIV during the solidification would need to be addressed.

2) Investigation into varied heat source temperature

The current investigation limited the heat source to a constant temperature. In practice, the applied heat source to the latent heat TES system would vary depending on external conditions. A detailed study into the effect of heat source temperature would further extend the knowledge of heat transfer characteristics and design optimization.

3) Expanded investigation from 2D to 3D behavior

The present study investigated phase transition in an enclosure that was constructed with a depth much less than the height and width to limit the 3D effects and provide an approximate 2D geometry. This constraint provided a simplified heat transfer process, beneficial for initial investigations. However, in practical applications, all TES systems are three-dimensional in nature, and as such, further investigation into extended, 3D enclosure systems would allow a better characterization of the phase change and heat transfer processes, which will facilitate the design optimization for real world applications.

4) Investigate different heat source geometries

As previously discussed, work has been conducted by various researchers to improve heat transfer with the extension of heat transfer surfaces, such as fins. However, some of these studies concluded that the additional extensions may impact the natural convection within the liquid phase. The current study looked solely at a simple configuration of the heat source i.e. a plane wall. Additional investigations into various heat source geometries, and their impact on the fluid flow, and hence natural convection, could provide further insight into improving latent heat storage system design.

References

[1]   L. B. Kong, T. Li, H. H. Hng, F. Boey, T. Zhang, and S. Li, "Waste Energy Harvesting: Mechanical and Thermal Energies," *Energy Technol.*, vol. 24, no. 1, pp. 1–2, 15, May 2014.

[2]   L. Pérez-Lombard, J. Ortiz, and C. Pout, "A review on buildings energy consumption information," *Energy Build.*, vol. 40, no. 3, pp. 394–398, Jan. 2008.

[3]   *World Energy Outlook 2017*. OECD, 2017.

[4]   U.S. Energy Information Administration, "International Energy Outlook 2016," 2016.

[5]   H. Kharas, "The Unprecedented Expansion of the Global Middle Class An Update," *Glob. Econ. Dev.*, pp. 1–29, 2017.

[6]   International Energy Agency, *CO2 Emissions from Fuel Combustion 2017*, vol. 1. 2017.

[7]   R. Lal, "Offsetting global CO2 emissions by restoration of degraded soils and intensification of world agriculture and forestry," *L. Degrad. Dev.*, vol. 14, no. 3, pp. 309–322, 2003.

[8]   D. R. Taub, B. Miller, and H. Allen, "Effects of elevated CO2 on the protein concentration of food crops: a meta-analysis," *Glob. Chang. Biol.*, vol. 14, no. 3, pp. 565–566, Nov. 2007.

[9]   S. Shafiee and E. Topal, "When will fossil fuel reserves be diminished?," *Energy Policy*, vol. 37, no. 1, pp. 181–189, 2009.

[10]   M. A. Bashar, "Experimental Investigation of the Melting Behavior and the Transient Heat Transfer in a Phase Change Material (PCM)," 2016.

[11]   D. Shively, J. Gardner, T. Haynes, and J. Ferguson, "Energy storage methods for renewable energy integration and grid support," in *2008 IEEE Energy 2030*

Conference, ENERGY 2008, 2008, pp. 1–6.

[12] National Energy Board of Canada, "Canada's Energy Future 2017: Energy Supply and Demand Projections to 2040," p. 8, 2017.

[13] J. Yagi and T. Akiyama, "Storage Of Thermal-Energy For Effective Use Of Waste Heat From Industries," *J. Mater. Process. Technol.*, vol. 48, no. 1–4, pp. 793–804, Jan. 1995.

[14] T. Hendricks and W. T. Choate, "Engineering Scoping Study of Thermoelectric Generator Systems for Industrial Waste Heat Recovery," *US Dep. Energy*, vol. 20, pp. 2, 14, 2006.

[15] H. Chen, T. N. Cong, W. Yang, C. Tan, Y. Li, and Y. Ding, "Progress in electrical energy storage system: A critical review," *Prog. Nat. Sci.*, vol. 19, no. 3, pp. 291–312, Mar. 2009.

[16] A. Sharma, V. V. Tyagi, C. R. Chen, and D. Buddhi, "Review on thermal energy storage with phase change materials and applications," *Renew. Sustain. Energy Rev.*, vol. 13, no. 2, pp. 318–345, Feb. 2009.

[17] B. Dunn, H. Kamath, and J. M. Tarascon, "Electrical energy storage for the grid: A battery of choices," *Science (80-.).*, vol. 334, no. 6058, pp. 928–935, Nov. 2011.

[18] B. E. Conway, "Transition from 'Supercapacitor' to 'Battery' Behavior in Electrochemical Energy Storage," *J. Electrochem. Soc.*, vol. 138, no. 6, pp. 1539–1547, 1991.

[19] S. M. Hasnain, "Review on sustainable thermal energy storage technologies, part I: Heat storage materials and techniques," *Energy Convers. Manag.*, vol. 39, no. 11, pp. 1127–1138, Aug. 1998.

[20] M. Haider and A. Werner, "An overview of state of the art and research in the fields of sensible, latent and thermo-chemical thermal energy storage," *Elektrotechnik und Informationstechnik*, vol. 130, no. 6, pp. 153–160, Sep. 2013.

[21] A. Abedin and M. Rosen, "A Critical Review of Thermochemical Energy Storage Systems.," *Open Renew. Energy J.*, vol. 4, pp. 42–46, 2011.

[22] B. Zalba, J. M. Marín, L. F. Cabeza, and H. Mehling, "Review on thermal energy storage with phase change: Materials, heat transfer analysis and applications," *Appl. Therm. Eng.*, vol. 23, no. 3, pp. 251–283, Feb. 2003.

[23] S. A. Mohamed *et al.*, "A review on current status and challenges of inorganic phase change materials for thermal energy storage systems," *Renew. Sustain. Energy Rev.*, vol. 70, pp. 1072–1089, 2016.

[24] H. Ibrahim, A. Ilinca, and J. Perron, "Energy storage systems-Characteristics and comparisons," *Renew. Sustain. Energy Rev.*, vol. 12, no. 5, pp. 1221–1250, Jun. 2008.

[25] H. Zhao, Q. Wu, S. Hu, H. Xu, and C. N. Rasmussen, "Review of energy storage system for wind power integration support," *Appl. Energy*, vol. 137, pp. 545–553, 2015.

[26] R. Madlener and Y. Sunak, "Impacts of urbanization on urban structures and energy demand: What can we learn for urban energy planning and urbanization management?," *Sustain. Cities Soc.*, vol. 1, no. 1, pp. 45–53, 2011.

[27] X. Wang, G. Gaustad, C. W. Babbitt, C. Bailey, M. J. Ganter, and B. J. Landi, "Economic and environmental characterization of an evolving Li-ion battery waste stream," *J. Environ. Manage.*, vol. 135, pp. 126–134, 2014.

[28] M. M. Farid, A. M. Khudhair, S. A. K. Razack, and S. Al-Hallaj, "A review on phase change energy storage: Materials and applications," *Energy Convers. Manag.*, vol. 45, no. 9–10, pp. 1597–1615, Jun. 2004.

[29] R. Baetens, B. P. Jelle, and A. Gustavsen, "Phase change materials for building applications: A state-of-the-art review," *Energy Build.*, vol. 42, no. 9, pp. 1361–1368, Sep. 2010.

[30] E. Oró, A. de Gracia, A. Castell, M. M. Farid, and L. F. Cabeza, "Review on phase change materials (PCMs) for cold thermal energy storage applications," *Appl. Energy*, vol. 99, pp. 513–533, Nov. 2012.

[31] A. M. Khudhair and M. M. Farid, "A review on energy conservation in building applications with thermal storage by latent heat using phase change materials," *Energy Convers. Manag.*, vol. 45, no. 2, pp. 263–275, 2004.

[32] S. D. Sharma and K. Sagara, "Latent Heat Storage Materials and Systems: A Review," *Int. J. Green Energy*, vol. 2, no. 1, pp. 1–56, 2005.

[33] J. Stefan, "Uber die Theorie der Eisbildung, insbesondere uber die Eisbildung im Polarmeere," *Ann. Phys.*, vol. 278, no. 2, pp. 269–286, 1891.

[34] C. Vuik, "Some historical notes on the Stefan problem.," 1984.

[35] E. Sparrow, R. R. Schmidt, and J. W. Ramsey, "Experiments on the Role of Natural Convection in the Melting of Solids," *J. Heat Transf. Asme*, vol. 100, no. 1, pp. 12–16, Feb. 2009.

[36] A. G. Bathelt, R. Viskanta, and W. Leidenfrost, "An experimental investigation of natural convection in the melted region around a heated horizontal cylinder," *J. Fluid Mech.*, vol. 90, no. 2, pp. 227–239, Jan. 1979.

[37] D. N. Nkwetta and F. Haghighat, "Thermal energy storage with phase change material - A state-of-the art review," *Sustain. Cities Soc.*, vol. 10, pp. 87–100, 2014.

[38] F. Agyenim, N. Hewitt, P. Eames, and M. Smyth, "A review of materials, heat transfer and phase change problem formulation for latent heat thermal energy storage systems (LHTESS)," *Renew. Sustain. Energy Rev.*, vol. 14, no. 2, pp. 615–628, Feb. 2010.

[39] B. Zivkovic and I. Fujii, "Analysis of isothermal phase change of phase change material within rectangular and cylindrical containers," *Sol. energy*, vol. 70, no. 1, pp. 51–61, Jan. 2001.

[40] Z. Zongqin and A. Bejan, "The problem of time-dependent natural convection melting with conduction in the solid," *Int. J. Heat Mass Transf.*, vol. 32, no. 12, pp. 2447–2457, 1989.

[41] C. J. Ho and C. H. Chu, "Numerical simulation of heat penetration through a vertical rectangular phase change material/air composite cell," *Int. J. Heat Mass Transf.*, vol. 39, no. 9, pp. 1785–1795, Jun. 1996.

[42] A. A. Ghoneim, "Comparison of theoretical models of phase-change and sensible heat storage for air and water-based solar heating systems," *Sol. Energy*, vol. 42, no. 3, pp. 209–220, 1989.

[43] J. Wang, Y. Ouyang, and G. Chen, "Experimental study on charging processes of a cylindrical heat storage employing multiple-phase-change materials," *Int. J. Energy Res.*, vol. 25, no. 5, pp. 439–447, Apr. 2001.

[44] T. Hirata and K. Nishida, "An analysis of heat transfer using equivalent thermal conductivity of liquid phase during melting inside an isothermally heated horizontal cylinder," *Int. J. Heat Mass Transf.*, vol. 32, no. 9, pp. 1663–1670, Sep. 1989.

[45] M. Esen, A. Durmuş, and A. Durmuş, "Geometric design of solar-aided latent heat store depending on various parameters and phase change materials," *Sol. Energy*, vol. 62, no. 1, pp. 19–28, Jan. 1998.

[46] F. L. Tan, S. F. Hosseinizadeh, J. M. Khodadadi, and L. Fan, "Experimental and computational study of constrained melting of phase change materials (PCM) inside a spherical capsule," *Int. J. Heat Mass Transf.*, vol. 52, no. 15–16, pp. 3464–3472, Jul. 2009.

[47] T. Saitoh and K. Hirose, "High-Performance Phase-Change Thermal Energy Storage Using Spherical Capsules," *Chem. Eng. Commun.*, vol. 41, no. 1–6, pp. 39–58, Apr. 1986.

[48] M. Okada, "Heat transfer during melting around vertical cylinder (1st report, analysis and experiments of the melting without subcooling)," *Bull. JSME*, vol. 28,

no. 243, pp. 2007–2013, 1985.

[49] H. Shokouhmand and B. Kamkari, "Experimental investigation on melting heat transfer characteristics of lauric acid in a rectangular thermal storage unit," *Exp. Therm. Fluid Sci.*, vol. 50, pp. 201–222, 2013.

[50] B. Kamkari, H. Shokouhmand, and F. Bruno, "Experimental investigation of the effect of inclination angle on convection-driven melting of phase change material in a rectangular enclosure," *Int. J. Heat Mass Transf.*, vol. 72, pp. 186–200, 2014.

[51] Y. Wang, A. Amiri, and K. Vafai, "An experimental investigation of the melting process in a rectangular enclosure," *Int. J. Heat Mass Transf.*, vol. 42, no. 19, pp. 3659–3672, 1999.

[52] D. Pal and Y. K. Joshi, "Melting in a side heated tall enclosure by a uniformly dissipating heat source," *Int. J. Heat Mass Transf.*, vol. 44, no. 2, pp. 375–387, 2001.

[53] C.-J. Ho and R. Viskanta, "Heat transfer during melting from an isothermal vertical wall," *J. Heat Transfer*, vol. 106, no. February 1984, pp. 12–19, Feb. 1984.

[54] C. Bénard, D. Gobin, and F. Martinez, "Melting in Rectangular Enclosures: Experiments and Numerical Simulations," *J. Heat Transfer*, vol. 107, no. 4, p. 794, 1985.

[55] M. Bashar and K. Siddiqui, "Investigation of heat transfer during melting of a PCM by a U-shaped heat source," *Int. J. Energy Res.*, vol. 41, no. 14, pp. 2091–2107, Nov. 2017.

[56] Z. Ling, J. Chen, T. Xu, X. Fang, X. Gao, and Z. Zhang, "Thermal conductivity of an organic phase change material/expanded graphite composite across the phase change temperature range and a novel thermal conductivity model," *Energy Convers. Manag.*, vol. 102, pp. 202–208, 2015.

[57] L. Fan and J. M. Khodadadi, "Thermal conductivity enhancement of phase change materials for thermal energy storage: A review," *Renew. Sustain. Energy Rev.*, vol.

15, no. 1, pp. 24–46, Jan. 2011.

[58]   A. Abhat, S. Aboul-Enein, and N. A. Malatidis, "Heat-of-Fusion Storage Systems for Solar Heating Applications," *Therm. Storage Sol. Energy*, pp. 157–171, 1981.

[59]   B. Kamkari and H. Shokouhmand, "Experimental investigation of phase change material melting in rectangular enclosures with horizontal partial fins," *Int. J. Heat Mass Transf.*, vol. 78, pp. 839–851, 2014.

[60]   N. Sharifi, T. L. Bergman, and A. Faghri, "Enhancement of PCM melting in enclosures with horizontally-finned internal surfaces," *Int. J. Heat Mass Transf.*, vol. 54, no. 19–20, pp. 4182–4192, Sep. 2011.

[61]   K. A. R. Ismail and F. A. M. Lino, "Fins and turbulence promoters for heat transfer enhancement in latent heat storage systems," *Exp. Therm. Fluid Sci.*, vol. 35, no. 6, pp. 1010–1018, Sep. 2011.

[62]   I. M. Bugaje, "Enhancing the thermal response of latent heat storage systems," *Int. J. Energy Res.*, vol. 21, no. 9, pp. 759–766, 1997.

[63]   J. C. Choi and S. D. Kim, "Heat transfer in a latent heat-storage system using MgCl2·6H2O at the melting point," *Energy*, vol. 20, no. 1, pp. 13–25, Jan. 1995.

[64]   S. Kalaiselvam, R. Parameshwaran, and S. Harikrishnan, "Analytical and experimental investigations of nanoparticles embedded phase change materials for cooling application in modern buildings," *Renew. Energy*, vol. 39, no. 1, pp. 375–387, Mar. 2012.

[65]   J. M. Khodadadi and S. F. Hosseinizadeh, "Nanoparticle-enhanced phase change materials (NEPCM) with great potential for improved thermal energy storage," *Int. Commun. Heat Mass Transf.*, vol. 34, no. 5, pp. 534–543, May 2007.

[66]   S. Motahar, A. A. Alemrajabi, and R. Khodabandeh, "Experimental investigation on heat transfer characteristics during melting of a phase change material with dispersed TiO2nanoparticles in a rectangular enclosure," *Int. J. Heat Mass Transf.*,

vol. 109, pp. 134–146, 2017.

[67] M. Bashar and K. Siddiqui, "Experimental investigation of transient melting and heat transfer behavior of nanoparticle-enriched PCM in a rectangular enclosure," *J. Energy Storage*, vol. 18, no. May, pp. 485–497, 2018.

[68] F. Frusteri, V. Leonardi, S. Vasta, and G. Restuccia, "Thermal conductivity measurement of a PCM based storage system containing carbon fibers," *Appl. Therm. Eng.*, vol. 25, no. 11–12, pp. 1623–1633, Aug. 2005.

[69] J. Wang, H. Xie, Z. Xin, Y. Li, and L. Chen, "Enhancing thermal conductivity of palmitic acid based phase change materials with carbon nanotubes as fillers," *Sol. Energy*, vol. 84, no. 2, pp. 339–344, Feb. 2010.

[70] Y. K. Oh and H. D. Yang, "Experimental and Numerical Study on the Melting Acceleration of Phase Change Material by Ultrasonic Vibrations," *Key Eng. Mater.*, vol. 324–325, pp. 1075–1078, Nov. 2006.

[71] I. Dincer and M. Rosen, *Thermal Energy Storage Systems and Applications*. 2011.

[72] H. Akeiber *et al.*, "A review on phase change material (PCM) for sustainable passive cooling in building envelopes," *Renewable and Sustainable Energy Reviews*, vol. 60. Pergamon, pp. 1470–1497, 01-Jul-2016.

[73] V. V. Tyagi and D. Buddhi, "PCM thermal storage in buildings: A state of art," *Renew. Sustain. Energy Rev.*, vol. 11, no. 6, pp. 1146–1166, Aug. 2007.

[74] H. H. Al-Kayiem and S. C. Lin, "Performance evaluation of a solar water heater integrated with a PCM nanocomposite TES at various inclinations," *Sol. Energy*, vol. 109, no. 1, pp. 82–92, Nov. 2014.

[75] N. Nallusamy, S. Sampath, and R. Velraj, "Experimental investigation on a combined sensible and latent heat storage system integrated with constant/varying (solar) heat sources," *Renew. Energy*, vol. 32, no. 7, pp. 1206–1227, Jun. 2007.

[76] D. Buddhi and L. K. K. Sahoo, "Solar cooker with latent heat storage: Design and experimental testing," *Energy Convers. Manag.*, vol. 38, no. 5, pp. 493–498, Mar. 1997.

[77] Y. Rabin, I. Bar-Niv, E. Korin, and B. Mikic, "Integrated solar collector storage system based on a salt-hydrate phase-change material," *Sol. Energy*, vol. 55, no. 6, pp. 435–444, Dec. 1995.

[78] C. Arkar and S. Medved, "Free cooling of a building using PCM heat storage integrated into the ventilation system," *Sol. Energy*, vol. 81, no. 9, pp. 1078–1087, Sep. 2007.

[79] S. Álvarez, L. F. Cabeza, A. Ruiz-Pardo, A. Castell, and J. A. Tenorio, "Building integration of PCM for natural cooling of buildings," *Appl. Energy*, vol. 109, pp. 514–522, Sep. 2013.

[80] E. M. Alawadhi and H. J. Alqallaf, "Building roof with conical holes containing PCM to reduce the cooling load: Numerical study," *Energy Convers. Manag.*, vol. 52, no. 8–9, pp. 2958–2964, Aug. 2011.

[81] F. Agyenim and N. Hewitt, "The development of a finned phase change material (PCM) storage system to take advantage of off-peak electricity tariff for improvement in cost of heat pump operation," *Energy Build.*, vol. 42, no. 9, pp. 1552–1560, Sep. 2010.

[82] Z. Ait Hammou, M. Lacroix, Z. A. Hammou, and M. Lacroix, "A new PCM storage system for managing simultaneously solar and electric energy," *Energy Build.*, vol. 38, no. 3, pp. 258–265, Mar. 2006.

[83] V. V. Tyagi, D. Buddhi, R. Kothari, and S. K. Tyagi, "Phase change material (PCM) based thermal management system for cool energy storage application in building: An experimental study," *Energy Build.*, vol. 51, pp. 248–254, Aug. 2012.

[84] M. Rajagopal and P. Natarajan, "Experimental Investigation on Phase Change Material Based Thermal Energy Storage System For Waste Heat Recovery From

I.C. Engine Exhaust," *Int. J. Appl. Eng. Res.*, vol. 10, no. 30, pp. 22909–22913, 2015.

[85] L. L. Vasiliev, V. S. Burak, A. G. Kulakov, D. A. Mishkinis, and P. V. Bohan, "Latent heat storage modules for preheating internal combustion engines: Application to a bus petrol engine," *Appl. Therm. Eng.*, vol. 20, no. 10, pp. 913–923, Jul. 2000.

[86] W. Sun, Z. Zhao, and Y. Wang, "Thermal analysis of a thermal energy storage unit to enhance a workshop heating system driven by industrial residual water," *Energies*, vol. 10, no. 2, 2017.

[87] R. E. Murray and D. Groulx, "Experimental study of the phase change and energy characteristics inside a cylindrical latent heat energy storage system: Part 1 consecutive charging and discharging," *Renew. Energy*, vol. 62, pp. 571–581, Feb. 2014.

[88] K. A. R. Ismail, C. L. F. Alves, and M. S. Modesto, "Numerical and experimental study on the solidification of PCM around a vertical axially finned isothermal cylinder," *Appl. Therm. Eng.*, vol. 21, no. 1, pp. 53–77, Jan. 2001.

[89] J. Bony and S. Citherlet, "Numerical model and experimental validation of heat storage with phase change materials," *Energy Build.*, vol. 39, no. 10, pp. 1065–1072, Oct. 2007.

[90] A. F. Regin, S. C. Solanki, and J. S. Saini, "Latent heat thermal energy storage using cylindrical capsule: Numerical and experimental investigations," *Renew. Energy*, vol. 31, no. 13, pp. 2025–2041, Oct. 2006.

[91] D. R. Lide, *CRC Handbook of Chemistry and Physics*, vol. 127, no. 12. 2005.

[92] S. Himran, R. Taraka, and A. Duma, "An Analysis on Thermal Energy Storage in Paraffin-Wax Using Tube Array on a Shell and Tube Heat Exchanger," vol. 9, no. 10, pp. 1781–1788, 2015.

[93]   E. A. Cowen, S. G. Monismith, E. A. Cowen, and S. G. Monismith, "A hybrid digital particle tracking velocimetry technique," *Exp. Fluids*, vol. 22, no. 3, pp. 199–211, Jan. 1997.

[94]   A. K. Prasad, R. J. Adrian, C. C. Landreth, and P. W. Offutt, "Effect of resolution on the speed and accuracy of particle image velocimetry interrogation," *Exp. Fluids*, vol. 13, no. 2–3, pp. 105–116, Jun. 1992.

[95]   National Instruments, "NI 9214 and TB-9214 Datasheet." p. 10, 2016.

[96]   National Instruments, "User Guide and Specifications: NI USB-9211/9211A," *System*. p. 16, 2008.

[97]   Y. A. Cengel and A. J. Ghajar, *Heat and Mass Transfer: Fundamentals and Applications*, 5th Editio. New York: McGraw-Hill Education, 2015.

Curriculum Vitae

Name:	Steven Jevnikar
Post-secondary Education and Degrees:	Bachelor of Engineering Science with Honors (BESc) Mechanical and Materials Engineering *2012-2016* The University of Western Ontario London, Ontario, Canada
	Master of Engineering Science Candidate (MESc) Mechanical and Materials Engineering *2016-2018* The University of Western Ontario London, Ontario, Canada
Honours and Awards:	The Western Scholarship of Excellence *(2012)* Dean's Honor List *(2012 – 2013)* Dean's Honor List *(2013 – 2014)* Dean's Honor List *(2014 – 2015)* Dean's Honor List *(2015 – 2016)* Ontario Graduate Scholarship *(2017-2018)*
Related Work Experience:	*2016-2018* – Teaching Assistant: Fluid Mechanics II Western University, London, ON, Canada
	2016-2018 – Teaching Assistant: Finite Element Methods in Mechanical Engineering Western University, London, ON, Canada
Conference Peer Reviewed Abstracts and Presentations	S. Jevnikar, K. Siddiqui, Investigation of The Flow Behavior In A PCM-Based Energy Storage Using Particle Image Velocimetry, Proceedings of 2017 Energy & Natural Resources Symposium, June 22-23, 2017, Windsor, Ontario, Canada
	S. Jevnikar, K. Siddiqui, The Influence of Heat Source Orientation on PCM Flow Behavior During Phase Transition, Proceedings of the 5th Joint US-European Fluids Engineering Summer Conference, July 15-20, 2018, Montreal, Quebec, Canada